Observational tests of new reflection models for AGN

Master's Thesis in Physics

Presented by
Julia Häfner
Erlangen, December 4, 2023

Astronomisches Institut, ECAP
Dr.-Karl-Remeis-Sternwarte Bamberg
Friedrich-Alexander-Universität Erlangen-Nürnberg

Supervisors: Dr. Thomas Dauser,
Prof. Dr. Jörn Wilms

Abstract

In this thesis, I tested different versions of the relativistic reflection model `RELXILLLP` (Dauser et al., 2013; García et al., 2014) on the XMM-Newton and NuSTAR datasets of the Seyfert-II AGN ESO 033-G002, the X-ray spectrum of which was found to be well described by a low height lamppost source (Walton et al., 2021). My main goal was, by testing the performance of the model when the luminosity of the primary X-ray source is taken into account, to validate the lamppost geometry on stricter conditions. The ionisation at the inner edge of the accretion disk is thereby calculated self-consistently. Previous model versions included the ionisation as a free parameter and neglected the primary luminosity. Furthermore, I tested the model assuming a thin-disk α-density gradient (Shakura & Sunyaev, 1973) and a radially constant density. I compared the results to previous versions which neglected the primary flux, assuming an α-disk density gradient and a constant density; the latter implementing either an empirical powerlaw ionisation gradient or a constant ionisation.

By applying the stricter lamppost model to the datasets analysed by Walton et al. (2021), I produced results which point to a geometry similar to the geometry implied by previous models, and could confirm the validity of the lamppost approach for ESO 033-G002. However, the stricter model tended to predict a higher ionisation for the inner disk radii, a lower source height, and a higher reflection fraction. I furthermore identified correlations between the free ionisation parameter and other parameters, which are prevented by calculating the ionisation self-consistently. By sampling the parameter space with an MCMC algorithm, I found an altogether different solution than by χ^2-minimization. Nevertheless, I could identify a degeneracy in the inclination parameter of the new model, which was caused by the variability of the self-consistent ionisation for different disk inclinations. I concluded that the stricter model, which takes the primary flux into account, is a valid and necessary rectification of `RELXILL` in the lamppost geometry and provides greater impact to reflection spectroscopy measurements of accreting objects.

Contents

1 Motivation

As of today, it is considered a fact that black holes (BHs) with masses $M_{\mathrm{BH}} > 10^6$ solar masses ($10^6\, M_\odot$) are located at the center of galaxies, also called *active galactic nuclei*. Their existence is, for example, revealed by the orbital motion of stars in galactic centers (Genzel et al., 2010). Usually, the black hole accretes matter from the surrounding galactic material due to its strong gravitational force, thereby forming an accretion disk. Due to the high temperature of this disk, its emission peaks in the UV regime. However, also hard X-rays are measured from galactic centers (Giacconi et al., 1962). A possible explanation for this could be the existence of a region of hot electron plasma, called the *corona*, in the vicinity of the black hole, in which the soft disk photons are Compton-upscattered into the X-ray regime. The X-ray emission, in turn, irradiates the accretion disk and is reprocessed ("reflected") by the disk material. This reflected component in the spectrum of active galactic nulei, which is intrinsic to accreting black holes, carries with it information about the black hole properties, and the geometry and chemical composition of the disk.

Measuring the properties of black holes inside galaxies is especially interesting in the context of galactic formation and evolution. There is a tight connection between the properties of supermassive black holes and their galactic hosts, which indicates a co-evolution between black holes and galaxies (e.g. Fiore et al., 2017). Understanding the evolution of supermassive black holes therefore offers a window into one of the largest time and spacial scale evolutions in our universe.

The mass of a supermassive black hole grows in two ways: via accretion of galactic material, or via merging with another black hole. This, however, occurs on time scales beyond the possibility of human observation. Instead, other measures for extracting information about the growth history of a black hole have to be found. One promising candidate is the black hole's angular momentum $\vec{J}$, also called *spin* when normalized by the black hole mass, which theoretically changes its orientation and magnitude due to processes increasing M_{BH}. Especially the iron-K emission line from the reflected spectrum of active galactic nuclei is, due to its high fluorencent yield and the high cosmic abundance of iron, the most important diagnostic tool for measuring angular momentum. Due to the rotation of the accretion disk and the gravitational potential of the black hole, the line profile is distorted by Doppler effects, gravitational redshift and lightbending. Especially the extended red wing of the line depends on the location of the inner edge of the accretion disk, from which the spin can be estimated. Problems arise when measuring the distribution of black hole spin. For example, a bias towards measuring high spin for any flux limited sample exists (Brenneman et al., 2011), which may be caused by low spin black holes being surrounded by truncated disks. In this case, the relativistic blurring of reflection features is weak, and the diagnostic potential decreases.

Theoretical techniques for modeling the spectra of accreting black holes have been under development for many years, from simple line models on top of a radiation continuum (Fabian et al., 1989; Laor, 1991) to intricate models of intrinsically connected reflection and relativistic blurring (Dauser et al., 2013; García et al., 2014). A promising approach is the so-called *lamppost geometry* (Matt et al., 1991), in which a point source corona on the rotation axis above the black hole irradiates the inner region of the accretion disk in X-rays. This geometry could be interpreted as the base of a jet of perpendicularly ejected material acting as a corona

Figure 1.1: Artist's conception of an accreting black hole with a lamppost corona above its spin axis, possibly being the base of a jet (credit: NASA/JPL-Caltech)

(Markoff et al., 2005), as illustrated in Figure 1.1. The fraction of reflection w. r. t. the primary coronal emission in the total spectrum can be directly estimated in the lamppost geometry. This quantity exhibits a radial maximum, which depends on the black hole spin, and can be used to rule out unphysical spin solutions. However, past lamppost models have ignored the flux of the primary continuum, which, together with the disk density, completely determines the ionisation of the disk's surface.

In this thesis, an improved version of the existing model `RELXILL` (Dauser et al., 2013; García et al., 2014) for relativistic reflection in the lamppost geometry, which takes the flux into account and self-consistently calculates the disk ionisation with it, will be tested. In order to introduce all necessary terms and equations, I will also cover the basics of general relativity, radiative transfer in matter, the physics, components and evolution of accreting supermassive black holes, and the history and tools of relativistic reflection modeling. If the tested model turns out to be successful, it will pose as another evidence for the validity of the lamppost geometry for suitable objects, and will help to refine spin measurements for the ongoing research on galactic evolution.

2 Basic general relativity

Today, it is considered a fact that space-time around a heavy body, like a neutron star or a black hole, is so heavily warped by their gravitation that even light is influenced by it. Photons in the vicinity of such a body will not follow straight paths defined by standard Euclidean geometry, but paths that appear bent from our point of view. In order to properly describe spectra coming from such a heavy body, it is necessary to understand the exact geometric rules the photons follow under the influence of extreme gravitational forces.

Before the theory of general relativity was founded, Newtons law of gravity was considered an exact solution describing the force which two spherical masses exert on each other. It relates the strength of the force to the masses M_1 and M_2, and the distance between those masses in the simple equation

$$F = \mathrm{G}\,\frac{M_1 M_2}{R^2}, \tag{2.0.1}$$

where the gravitational constant G has been measured as $\mathrm{G} = 6.6743 \times 10^{-11}\,\mathrm{m^3\,kg^{-1}\,s^{-2}}$ with very high precision (Workman et al., 2022). The validity of this law, however, turned out to be limited when, for example, an excess in the precession of the perihelion of the Mercury orbit around the sun was discovered in 1845 (Einstein, 1915b). From our perspective today, Newton's law of gravity is only a good approximation for static forces between bodies at rest. While publishing papers on the topic since 1907, Einstein achieved a breakthrough in theoretical astrophysics in 1915 by adapting the mathematical concept of fields, already being used in electrodynamics, to describe gravitational fields in the equations of the theory of general relativity (Einstein, 1915a).

A short introduction of the basic concepts leading up to the concept of black holes shall be given in this chapter, which largely follows the published lectures of van Holten (1997). In all equations, I assume $\mathrm{G} = \mathrm{c} = 1$ for simplicity.

2.1 Einstein's equations

The gravitational potential field is described by the four-dimensional metric tensor $g_{\mu\nu}$ which constitutes the space-time line element

$$ds^2 = g_{\mu\nu}(x)\mathrm{d}x^\mu \mathrm{d}x^\nu. \tag{2.1.1}$$

In the above expression, the Einstein sum convention was used, wherein one executes a full summation over each index which appears twice, one lower and one upper. The gravitational vector field is then calculated from the potential gradients, i.e. the difference in potential from one point in space-time to another, and describes the force exerted on a test particle inside the potential. The acceleration gained from this approach is independent of the mass of the particle. The Minkovski matrix $\eta_{\mu\nu} = \mathrm{diag}(-1, 1, 1, 1)$ is a special case of $g_{\mu\nu}$ when no gravitational potential is present. For this case, also called *flat spacetime*, the space-time element in the restframe of a test particle is given by

$$-\mathrm{d}s^2 = c^2 \mathrm{d}\tau^2, \tag{2.1.2}$$

where $\mathrm{d}\tau$ is interpreted to be the proper time interval measured by a clock in the particle's rest frame. Both quantities are invariant under all coordinate transforms.

Equation 2.1.2 is only valid for the theory of special relativity, developed by Einstein since the publishing of his paper in 1905 (Einstein, 1905), i.e. in the absence of a mass which alters the shape of space-time. Instead, the theory of general relativity accounts for gravitational potentials. Here, a distinct geometric interpretation can only be given for the so-called *connection*,

$$\Gamma^{\lambda}_{\mu\nu} = \frac{1}{2} g^{\lambda\chi}(\partial_\mu g_{\chi\nu} + \partial_\nu g_{\mu\chi} + \partial_\chi g_{\mu\nu}), \tag{2.1.3}$$

which defines geodesics in space-time, i.e. the shortest possible connection between two points, where the total proper time $\int \mathrm{d}\tau$ is at an extremum.

The *Riemann tensor* – a higher-dimensional generalization of Gaussian curvature – is a measure of the curvature of space-time in the theory of general relativity. When all its components vanish, space-time is flat. The curvature itself is a measure of the gravitational potential gradient. The famous Einstein equations

$$R_{\mu\nu} - \frac{1}{2} g_{\mu\nu} R_{\mu\nu} = -\frac{8\pi G}{c^4} T_{\mu\nu} \tag{2.1.4}$$

describe the curvature of space-time in a general form. Here, $\mathrm{R}_{\mu\nu}$ is the *Ricci-tensor*, a contraction of the Riemann-tensor, and $\mathrm{T}_{\mu\nu}$ is the *energy-momentum tensor* which describes the density and flux of energy, and the density and flux of momentum in space-time, similar to the stress tensor in Newtonian mechanics. The Einstein equations are a set of nonlinear partial differential equations of second order, and their solutions give the exact form of the gravitational potential for a specific energy-momentum distribution.

2.2 Schwarzschild Black Holes

From a theoretical perspective, black holes are solutions of Equation 2.1.4 which represent bodies whose fields are strong enough to even capture light permanently. They have a horizon, which acts as a point of no return for every infalling test particle, and a singularity, where the local space-time curvature becomes infinite. In general, black holes are defined by three parameters only: mass, electric charge and angular momentum.

In 1916, Karl Schwarzschild found a solution of Einstein's equations for a point mass in static, spherically symmetric space-time (Schwarzschild, 1916). When the coordinate radius r approaches infinity, space-time becomes asymptotically flat. This solution in asymptotic Minkowskian space, seen from an observer at spatial infinity, yields two singularities: one at $r = 0$, and one for $r = m/2$ at the horizon, where m denotes the mass of the heavy body. Moreover, it can be shown that the regime $(0,\, m/2)$ can be mapped isometrically to $(m/2,\, \infty)$; so the inside of the horizon is basically a double cover of the outside. With this, it becomes clear that a distant observer cannot see past the horizon, as he or she is disconnected from space-time at $r < m/2$. From the distant observer's point of view, an infalling particle would take an infinite Minkowski-time to reach the horizon. Approaching $r = m/2$, it would appear increasingly slow as well as more and more redshifted, since the light has to travel out of a deeper point of the potential well the closer the particle gets to the horizon. The latter effect is called *gravitational redshift*.

In order to examine the inside of the horizon, one needs to transform the coordinates to the restframe of the infalling particle, for example via Eddington-Finkelstein coordinates. The horizon is now located at $r^* = 2m$ or, what is known in SI units as the *Schwarzschild radius*,

$$r^* = \frac{2\mathrm{G}M}{c^2}, \tag{2.2.1}$$

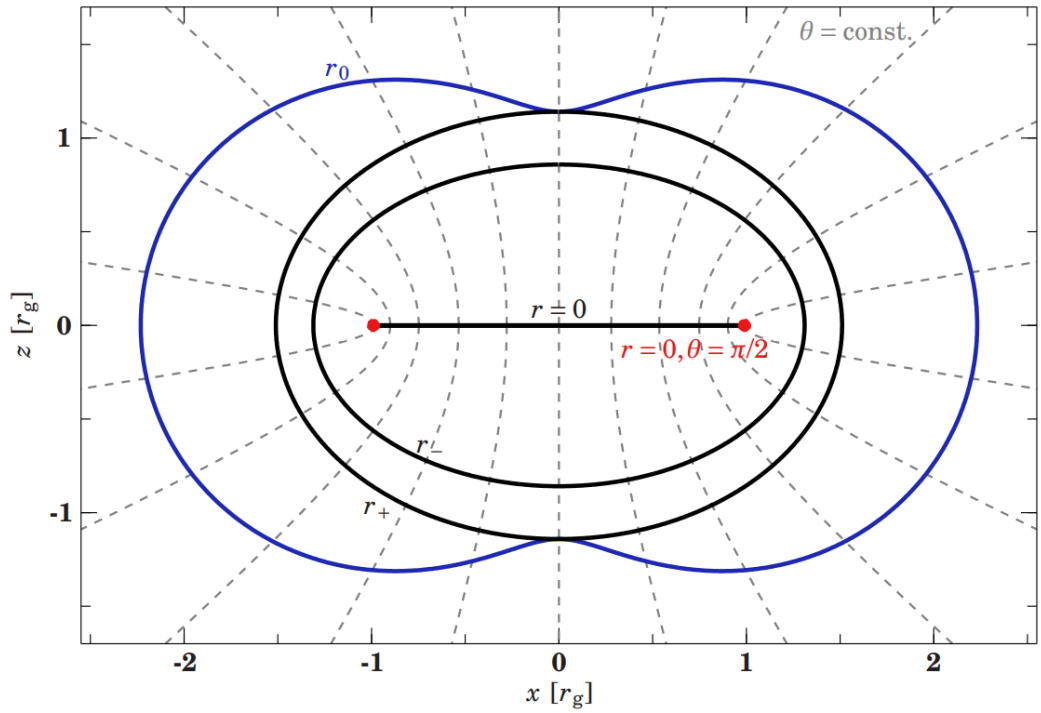

Figure 2.1: Y-plane cross section through a Kerr black hole. The surfaces illustrated are the ergosphere r_0, the two horizons $r_\pm$ and the ring singularity at $r = 0$. The dashed grey lines are the Boyer-Lindquist coordinate lines for a constant angle θ (taken from Dauser, 2010).

with the mass M relating to m like $m = GM$. More commonly used to describe size scales of black hole systems is the *gravitational radius* $r_\mathrm{g} = r^*/2$. Since the metric remains finite at this radius, it is no longer a singularity; the singularity described by the isotropic coordinates is merely a coordinate singularity. The singularity at $r = r^* = 0$, however, is coordinate-independent and therefore physical. Moreover, the roles of time coordinate and radial coordinate are interchanged for $r^* < 2m$, which shows intrinsically that all possible world lines for infalling particles end in the singularity, i.e. the radial infall cannot be reversed.

2.3 Kerr Black Holes

For this thesis, the additional consideration of rotation is important, since accreting astrophysical black holes take over the angular momentum of the accreted particles in order to ensure angular momentum conservation. Rotating black holes are described by the Kerr-metric, where the radial symmetry is broken in favour of an axial symmetry, the rate of rotation stays constant, and the exterior metric is time-independent. The choice of coordinates are Boyer-Lindquist coordinates (Boyer & Lindquist, 1967)

$$\begin{aligned} x &= \sqrt{r^2 + a^2}\,\sin\theta\,\cos\phi \\ y &= \sqrt{r^2 + a^2}\,\sin\theta\,\sin\phi \\ z &= r \cdot \cos\theta, \end{aligned} \tag{2.3.1}$$

an elliptical modification of Cartesian coordinates, where a is a constant which parameterizes the deviation of the line element from the form of the Schwarzschild metric, and θ and ϕ

are the spherical coordinate angles. The physical interpretation is that of the total angular momentum per unit mass $a = J/m$, also called *spin* of the black hole. The solution yields two horizons,

$$r^*_{\pm} = m \pm \sqrt{m^2 – a^2}. \tag{2.3.2}$$

When a approaches zero, the inner horizon r_- coincides with the singularity, and the outer horizon r_+ becomes the Schwarzschild radius; in other words, the Kerr solution becomes the Schwarzschild solution for non-rotating black holes. When the rotation becomes maximal ($a = m$), the two horizons blend together at $r^* = m$, which is half of the Schwarzschild radius for a non-rotating case. One could therefore say that a black hole becomes smaller the faster is rotates. Equation 2.3.2 also intrinsically poses limits for the unitless spin quantity $a^* = a/m$ in the form of the interval $-1 < a^* < +1$, where $a^* = -1$ represents maximal counter-rotation, and $a^* = +1$ maximal rotation. These limits arise because the horizon can maximally rotate at light speed. For simplicity, I will use the parameter a to refer to the unitless spin a^* for the rest of this thesis.

An analysis of the geodesic flow shows that there are no purely radial geodesics, i.e. any incoming test particle picks up rotation. In this context, the surface

$$r^*_0(\theta) = m + \sqrt{m^2 – a^2 \cos^2(\theta)} \tag{2.3.3}$$

defines a region inside which every particle has to co-rotate with the black hole because space-time itself is rotating. The regions between r_0 and r_+ is thus called the *ergosphere*. For $a > 0$ and $\theta = (0, \pi)$, the ergosphere cuts the outer horizon twice at the axis of rotation and billows out in a pumpkin-like shape for other values of theta.

Another coordinate transform into Kerr-Schild coordinates is necessary to inspect the nature of the Kerr-singularity. For $r^* = 0$ and $\theta = \pi/2$, it is mapped to the ring

$$x^2 + y^2 = a^2, \qquad z = 0. \tag{2.3.4}$$

It is therefore also called *ring singularity*. As a result of this peculiar shape, the geodesics crossing the horizon do not necessarily end up in the singularity, but can pass it by. The y-plane cross section of both horizons of a Kerr black hole in a Boyer-Lindquist coordinate system, as well as the ergosphere surface and the ring singularity are illustrated in Figure 2.1.

3 Radiative transfer

When a beam of X-rays hits a cluster of dust or gas in space, the photons interact with the material via scattering, absorption and re-emission. Since these energy and material dependent effects alter the shape of the incident spectrum in various ways, it is important to understand the processes down to the most basic atomic transitions. Only in this way, spectral modeling and therefore the inference of general astrophysical parameters can be successful. This chapter, unless specified otherwise, will largely follow the corresponding chapters in Netzer (2013).

In general, the local radiative flux per frequency in matter can be described by the specific intensity I_ν. The combined effect of absorption loss and scattering processes is expressed in the monochromatic absorption cross section κ_ν, and the locally emitted monochromatic flux is given by the the volume emission coefficient j_ν. All quantities are defined per unit time, volume and solid angle. Together, they give the equation of radiative transfer

$$\frac{dI_\nu}{ds} = -\kappa_\nu I_\nu + j_\nu, \tag{3.0.1}$$

which describes the change of radiative intensity per path length interval travelled inside the disk. It is given as the sum of the intensity loss due to absorption and scattering, and the intensity gain due to local (re-)emission. By defining the quantities of optical depth element $\tau_\nu = \kappa_\nu \mathrm{d}s$ and the source function $S_\nu = j_\nu/\kappa_\nu$, Equation 3.0.1 becomes

$$\frac{dI_\nu}{d\tau_\nu} = -I_\nu + S_\nu. \tag{3.0.2}$$

The solution to this equation is dependent on the geometry of the disk. For a perfect slab of thickness τ_ν, the solution perpendicular to the slab can be given as

$$I_\nu(\tau_\nu) = I_\nu(0)\,\mathrm{e}^{-\tau_\nu} + \int_0^{\tau_\nu} \mathrm{e}^{-(\tau_\nu - t)} S_\nu(t) dt. \tag{3.0.3}$$

For any other direction, I_ν will depend on the angle between the disk and the direction of propagation. The integral in Equation 3.0.3 is difficult to solve in most cases and requires numerical methods. Only in the case of a perfect slab and a source function that is independent of thickness, the integral can be solved analytically. For an opaque source in thermodynamic equilibrium, I_ν approaches the Planck function, which describes the spectrum of a blackbody for a certain frequency, dependent only on the temperature.

3.1 Compton Scattering

Generally, the scattering interaction between electrons and photons is described by *Compton scattering*. For slow or stationary electrons and light in the classical electromagnetic wave picture, the scattering is quasi-elastic, i.e. the energy and momentum of the incoming wave are conserved. The relationship between incoming (ν) and outgoing (ν') frequency is

$$\nu' = \frac{m_\mathrm{e} c^2 \nu}{m_\mathrm{e} c^2 + h\nu(1 - \cos\theta)}. \tag{3.1.1}$$

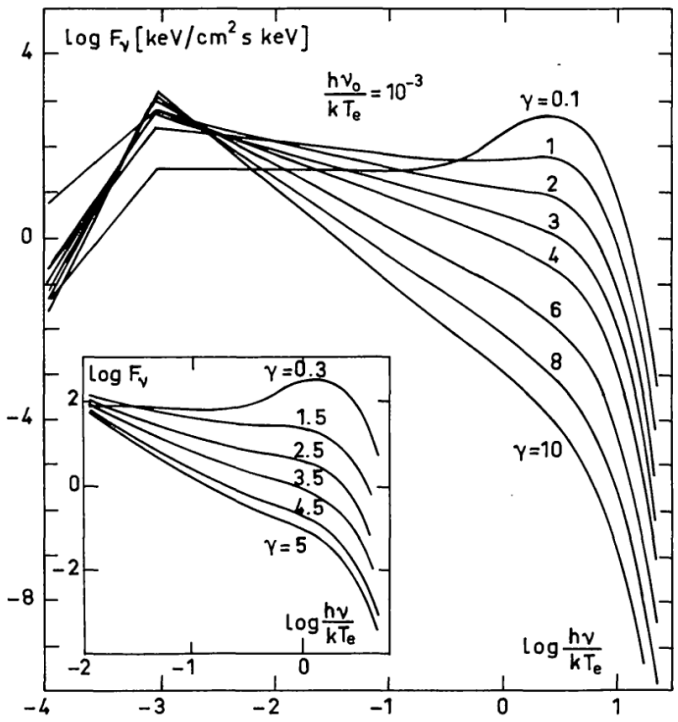

Figure 3.1: Comptonized spectra for different γ-parameters, where $\gamma \approx y^{-1}$ and y denotes the average energy gain via scattering. The Compton thick case is represented by $\gamma = 0.1$ ($y \approx 10$) and produces a "Wien peak". For higher γ values up to $\gamma = 10$ ($y \approx 0.1$), the spectrum approaches a powerlaw which cuts off at the characterisic electron temperature kT_e/h (taken from Sunyaev & Titarchuk, 1980).

This process is called *Thomson scattering*. Here, m_e denotes the electron rest mass and θ is the angle between the unit vectors of the incoming and outgoing directions of propagation. The differential Thomson cross section is given by

$$\frac{d\sigma}{d\Omega} = \frac{1}{2} r_e^2 \left(1 + \cos^2\theta\right). \tag{3.1.2}$$

For relativistic electron energies, the scattering becomes inelastic, and the symmetry in the scattering angle from Equation 3.1.2 is broken in favor of forward scattering. The corresponding quantum mechanical, relativistic *Klein-Nishina cross section* reduces to the Thomson cross section for photon energies that are negligible compared to the electron's rest energy. For even higher photon energy, the Klein-Nishina cross section decreases from it's initial value, i.e. a scattering becomes less probable. By evaluating the scattering in the electron's rest frame and transforming back to the lab system, the energy transfer turns out to be a factor of γ^2 larger than for non-relativistic electrons, making the scattering very efficient at high energies.

Let us now assume a Maxwell distributed ideal electron gas in thermodynamic equilibrium. Since photons are bosons, the incoming photons are Bose-Einstein distributed. At a certain electron temperature, the photons will gain energy from collisions with the electrons, in turn cooling them down. The fraction α of the electron energy kT_e transferred to the photon can be expressed as (Rybicki & Lightman, 2004)

$$\frac{\Delta E}{E} = -\frac{E}{m_e c^2} + \frac{\alpha k T_e}{m_e c^2} \tag{3.1.3}$$

in the electron's frame of rest. In thermal equilibrium, photons and electrons only interact through scattering, and Compton heating and cooling are in a balance. Therefore, the averaged net energy change is zero ($\langle \Delta E \rangle = 0$), and by calculating $\langle E \rangle$ and $\langle E^2 \rangle$ from the photon distribution, one can write

$$\langle \Delta E \rangle = 0 = \frac{\alpha k T_e}{m_e c^2} \langle E \rangle - \frac{1}{m_e c^2} \langle E^2 \rangle = (\alpha - 4) \frac{3(kT_e)^2}{m_e c^2} \tag{3.1.4}$$

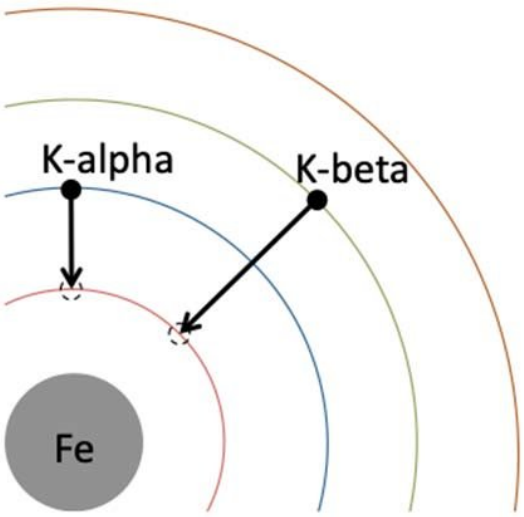

Figure 3.2: Atomic shell structure around the iron core. The K-, L-, M- and N-shell are depticted in red, blue, green and orange, respectively. The Kα and Kβ transitions are illustrated as black arrows (taken from Lapointe, 2020).

so that $\alpha = 4$ in this case. The Compton amplification factor can then be defined as

$$A := \frac{\Delta E}{E} = \frac{4kT_\mathrm{e} - E}{m_\mathrm{e}c^2}. \tag{3.1.5}$$

With photon energy $\mathrm{E} > 4\mathrm{kT_e}$, the photon loses energy (or is *down-scattered*) while for $\mathrm{E} < 4\mathrm{kT_e}$, it gains energy (or is *up-scattered*). The up-scattering of photons in a hot electron gas is also called *Comptonization*. The emerging Comptonized photon spectrum is a powerlaw with index

$$\Gamma = -\frac{3}{2} \pm \sqrt{\frac{9}{4} + \frac{4}{y}}. \tag{3.1.6}$$

Here, the minus sign applies to the case of $y \gg 1$ and the plus sign to the case of $y \ll 1$. For $y \sim 1$, called *unsaturated Comptionization*, the average is calculated. The so-called Compton-Y parameter is defined as

$$y = \max(\tau_\mathrm{e}, \tau_\mathrm{e}^2) \left[\frac{4kT_\mathrm{e}}{m_\mathrm{e}c^2}\right], \tag{3.1.7}$$

where the mean number of scatterings in a medium of optical depth τ_e is $\max(\tau_\mathrm{e}, \tau_\mathrm{e}^2)$, such that it grows quadratically for $\tau_\mathrm{e} > 1$ (optically thick case) and linearly for $\tau_\mathrm{e} < 1$ (optically thin case). An illustration of the different spectral regimes is shown in Figure 3.1. For $y < 1$, the spectrum equals a powerlaw spectrum with a certain high energy exponential cutoff reflecting the electron temperature. Most AGN sources exhibit $y \sim 1$, which corresponds to a powerlaw index of $\Gamma \sim 1.5$. For $y \gg 1$, the net photon energy equals the electron thermal energy and the Comptonization process is saturated. The corresponding spectrum exhibits a "Wien hump", which has never been observed in real sources.

3.2 Atomic transitions of iron

Emission lines in photon energy spectra from AGN correspond to the discrete energies of atomic shell transitions. The chemical element Fe, iron, is the end product of stellar nucleosynthesis, since the fusion from iron to cobalt no longer releases energy, but dissipates it. Because of this, iron is a highly abundant element in accretion disks. The iron emission lines are often the most prominent features in astrophysical X-ray spectra. Also, the energy range of 6–8 keV, in

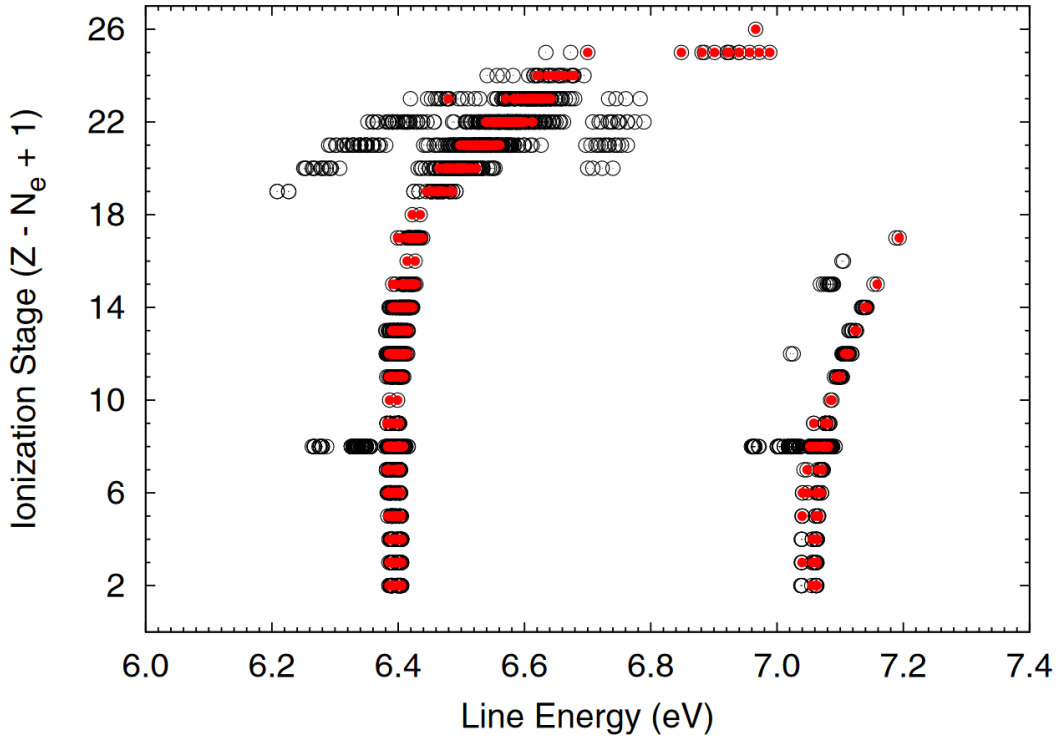

Figure 3.3: Line energies of iron for different ionisation stages from neutral to almost fully ionized. The two groupings of points correspond to the Kα transition (left) and the Kβ transition (right) (taken from García et al., 2013).

which most iron emission lines are found, is a relatively clean part in the spectrum where few other ions emit or absorb radiation, most detectors operate very efficiently in this range, and galactic absorption plays a negligible role. Iron emission features are therefore a useful subject for testing accreting black hole and accretion disk parameters.

In the simplified electron shell picture, The iron atom has 26 shells which are labeled, beginning from the innermost shell, as letter K, L, M, N, et cetera. These four innermost shells around the core are illustrated in Figure 3.2. If an X-ray photon now hits the iron atom and ionizes it, the resulting gap in the shell structure can be filled in two ways. In the *Auger process*, an electron from another shell drops to the empty position, and the released change in binding energy ionizes an outer shell electron. Since no photons are included in the end product, the Auger process produces no emission lines. Nevertheless, there is a certain probability proportional to Z^4 that a photon is emitted from the shell transition, where Z is the nuclear charge of the ion. From all transitions, the K-shell transitions possess the largest fluorescence yield, and are therefore most important for X-ray spectroscopic analysis. They are labeled as Kα, Kβ, Kγ et cetera, for electrons transitioning from the L-, M- and N-shell to the K-shell, respectively.

Depending on the ionisation stage, different line energies are observed. Figure 3.3 shows all radiative transitions of iron depending on the ionisation stage number $(Z - N_\mathrm{e} + 1)$ in the 6–10 keV range, where N_e is the number of electrons in the atom. They are included in the Database[1] used in the reflection model `XILLVER` (García et al., 2013), which needs to implement a large number of atomic transition in order to calculate an X-ray spectrum being reflected on an accretion disk. From bottom to top, the atom goes from a neutral state to a

[1] `https://heasarc.gsfc.nasa.gov/uadb`

fully ionized state. In total, there are 2735 lines which all correspond to K-shell transitions; the ones depicted are from the Kα complex on the left, and the Kβ complex on the right. The ionisation stages of iron are also denoted by roman numbers, from Fe II (once ionized) to Fe XXVI (one electron left). What is referred to as the "Kα-line" seen in many spectra is actually a conglomerate of many lines in the range of 6.39–6.43 keV. As the ionisation stage increases, the lines shift to higher energies and diverge. After Fe XVII, the M-shell is empty, therefore the Kβ line is only produced up to this stage. For almost fully ionized ions (Fe XXV and Fe XXVI), only a few lines around 6.9 keV remain.

The proper modeling of all relevant atomic transitions and possible emission lines helps to achieve more precise estimates of black hole and accretion disk parameters. The reflection model `XILLVER`, as well as the relativistic model `RELXILL` (Dauser et al., 2013; García et al., 2014) use the same atomic database for calculating emission lines by summing the local emission at different ionisation stages across the disk.

4 The physics of active galactic nuclei

Since Giacconi et al. (1962) launched a rocket carrying a Geiger counter into the atmosphere and subsequently detected a peak in the X-ray background near the galactic center, ongoing scientific research has brought much insight into the workings of the X-ray emitting parts of galactic centers. This knowledge, in turn, can be used to refine the theoretical modeling techniques that belong in the toolbox of every X-ray astronomer. With the theoretical background having been introduced in the previous chapter, I turn to black holes at the center of galaxies as physical objects. Hints of the existence of black holes in general were first found when Webster & Murdin (1972) measured the mass of the Cygnus X-1 binary system. Black holes as real objects are nowadays generally accepted, and many thousands of assumed black holes are known.

In general, most black holes can be classified as belonging to one of two categories. On the one hand, *galactic black holes* (GBHs) have a few to tens of solar masses and are created by supernova explosions of massive stars. Hence, they are located inside galaxies. Some GBHs, called *X-ray binaries*, accrete matter from a companion star with which they form a binary system. *Supermassive black holes* (SMBHs), on the other hand, have masses in the order of 10^6 to 10^9 solar masses ($M_\odot$). They are also called *Active Galactic Nuclei* (AGN) since they are located at the center of galaxies and form an accretion disk with the surrounding gas from their host galaxy. AGN may also exhibit jets of ejected material, which is accelerated to relativistic speeds by the strong magnetic fields of the system.

For accreting black holes, the unitless spin parameter a, which was introduced in the previous section, acquires a different limit. Because of the infall of particles with negative and positive angular momentum (w. r. t. the rotation of the black hole), a counteracting torque is created for a realistic accretion scenario, and theoretical calculations show that in this case, the spin can maximally reach a value of $a = 0.998$ (Thorne, 1974). For the rest of this thesis, all mentions of maximally spinning black holes will refer to this value. Since this thesis will focus on AGN as objects to be studied, the next sections will introduce the components and types of AGN and motivate the physics of accretion specifically for those objects. The derivations largely follow the corresponding chapters in Netzer (2013).

4.1 Accretion in AGN

During accretion, the gravitational potential energy of infalling particles from the surrounding galactic material is converted into heat and electromagnetic radiation. The efficiency by which this conversion happens for the infall of mass m from infinity to radius r is given by the factor

$$\eta = \frac{[E(\infty) - E(r)]}{mc^2} \tag{4.1.1}$$

which relates the change in potential energy to the rest mass of the particle. The particles which initially possess already a high angular momentum will form an accretion disk around the black hole in which they spiral inwards by losing angular momentum through viscosity mechanisms and magneto-rotation instabilities. Gas with a small initial angular momentum might be accreted spherically instead, though the easiest theoretical and therefore most widely

used approach is that of the geometrically thin, optically thick disk first described by Novikov & Thorne (1973) and modeled by Shakura & Sunyaev (1973, hereafter SS73). The accretion rate is then given by

$$\dot{M} = \frac{L}{\eta c^2}, \tag{4.1.2}$$

where L is the total source luminosity. A theoretical limit to the accretion rate is posed by the Eddington luminosity L_{edd}, which is defined as the luminosity where the outward force from radiation pressure equals the inward gravitational force, $f_{\mathrm{rad}} = f_{\mathrm{g}}$. Beyond this limit, the applicability of the typical accretion scenario breaks down.

4.1.1 Properties and spectra of thin disks

For a thin disk, the accretion rate and the mass and spin of the central black hole determine the disk geometry, gas temperature, luminosity and emitted spectrum. In general, luminosities of thin disks fall into the range $0.01 \leq L/L_{\mathrm{edd}} \leq 0.3$, though the corresponding limits are not well constrained. It is further assumed that the radial velocity is small in comparison to the angular velocity, $v_{\mathrm{r}}(r) \ll v_{\phi}(r)$, and that the angular velocity is well approximated by the Keplerian velocity, $v_{\phi}(r) \simeq v_{\mathrm{K}}(r)$. The gas therefore moves inward slowly while retaining its circular motion, and the angular velocity is transported outward. The viscous torque exerted on the differentially rotating ring dr, by which this mechanism is fueled, is explained by friction or viscosity coupling of the motion of a particle inside this ring to particles just inside and outside of it. As a result, the outer disk is thought to expand and disintegrate into clumps beyond a radius r_{out}.

Inside a minimal radius but still outside of the event horizon, particles have lost all of their angular momentum and fall radially inward. Therefore they no longer emit electromagnetic radiation. This regime is called the *plunging region*. The minimal radius for which circular motion is still possible, also known as the radius of marginal stability (r_{ms}) or the radius of the innermost stable circular orbit (r_{ISCO}), is a function of the spin of the black hole (Dauser et al., 2010):

$$\begin{aligned} r_{\mathrm{ISCO}}(a) &= M\left(3 + Z_2 - \mathrm{sgn}(a)\sqrt{(3-Z_1)(3+Z_1+2Z_2)}\right) \\ Z_1 &= 1 + (1-a^2)^{1/3}\left[(1+a)^{1/3} + (1-a)^{1/3}\right] \\ Z_2 &= \sqrt{3a^2 + Z_1^2} \end{aligned} \tag{4.1.3}$$

The faster the black hole rotates, the smaller r_{ISCO} becomes. For maximal rotation ($a = 0.998$), the ISCO is located around $r \sim 1.25\, r_{\mathrm{g}}$.

The local release of energy at radius r due to accretion is gained by adding the luminosity due to loss of gravitational energy and the luminosity due to work done by the viscous torque on the exterior disk, $L_{\mathrm{r}} = L_{\mathrm{G}} + L_{\mathrm{N}}$. The energy release per unit time at all radii can then be written as

$$\frac{dL_{\mathrm{r}}}{dr} = \frac{3\mathrm{G}M\dot{M}}{2r^2} f(r), \tag{4.1.4}$$

where $f(r) = 1 - (r_{\mathrm{in}}/r)^{\frac{1}{2}}$ is a factor emerging from the condition that directly at r_{in}, there is no torque exerted on the particles from the inside. Assuming dL_{r} is released over the unit area $2\pi r dr$, it follows that the emissivity per unit disk area is

$$D(r) = \frac{1}{4\pi r}\frac{dL_{\mathrm{r}}}{dr}. \tag{4.1.5}$$

If we further assume that the local emission is a perfect blackbody, $D(r) = \sigma T(r)^4$, the two expressions can be equated and the radial temperature profile follows

$$T(r) = \left(\frac{3GM\dot{M}}{8\sigma\pi r^3} f(r) \right)^{\frac{1}{4}}. \tag{4.1.6}$$

The maximal disk temperature for supermassive black holes is $\sim 10^5$ K. Most of the energy from the accretion disk is therefore emitted in the UV regime. In comparison, stellar size black holes have a maximal temperature of $\sim 10^7$ K and emit in x-ray energies. In conclusion, the larger the black hole mass, the cooler its accretion disk.

For deriving the total disk emitted spectrum, first the locally emitted monochromatic luminosity dL_ν has to be formulated. It follows

$$\mathrm{d}L_\nu = 2\pi r[\pi B_\nu(T)]\mathrm{d}r \tag{4.1.7}$$

with the Planck function

$$B_\nu = \frac{2h\nu^3}{c^2} \left[\exp\left(\frac{h\nu}{kT} \right) - 1 \right]^{-1}. \tag{4.1.8}$$

Now Equation 4.1.6 can be inserted into the previous expression, which is integrated from r_{in} to r_{out} and multiplied by a factor of 2 to account for both sides of the disk. The total monochromatic luminosity then is proportional to

$$L_\nu \propto \dot{M}^{2/3} M^{2/3} \nu^{1/3}. \tag{4.1.9}$$

The $\nu^{1/3}$ dependence, however, is only valid for a limited, intermediate energy regime because of the physical disk boundaries. The maximal temperature at the inner boundary corresponds to a certain frequency ν_{in}; beyond this frequency, the spectrum drops exponentially with a functional dependence on the maximal temperature. The outer disk boundary, corresponding to a minimal temperature and frequency ν_{out}, poses a spectral dependence of ν^2 below ν_{out} which resembles a blackbody. A plot of the total disk spectrum is shown in Figure 4.1.

The widely used thin disk model of SS73 allows for a system of equations which describe the matter dynamics, thermal equilibrium and radiative energy density in the disk. As a solution, the distributions of the surface density and temperature along the disk radius can be given as functions of accretion rate $\dot{M}$, black hole mass M and efficiency of momentum transfer α, where $\alpha \ll 1$ applies to wide regions of the disk. The disk's thickness can be defined by equating radiation pressure force and the normal component of the gravitational force for each radius. Subsequently, the disk is split into three density regions differing by the local speed of sound, dominating pressure source and main interaction between matter and radiation. For the first region in which radiation pressure and free electron scattering are dominant, the density follows

$$n = 3.4 \times 10^{17} \frac{r^{3/2}}{\alpha\, M\, \dot{M}^2\, (1 - r^{-1/2})^{-2}}. \tag{4.1.10}$$

Especially for a disk that is X-ray irradiated and highly ionized only in the innermost region, this model is well justified. In later chapters, it will be argued that such a geometry applies to the source that is analysed in this thesis.

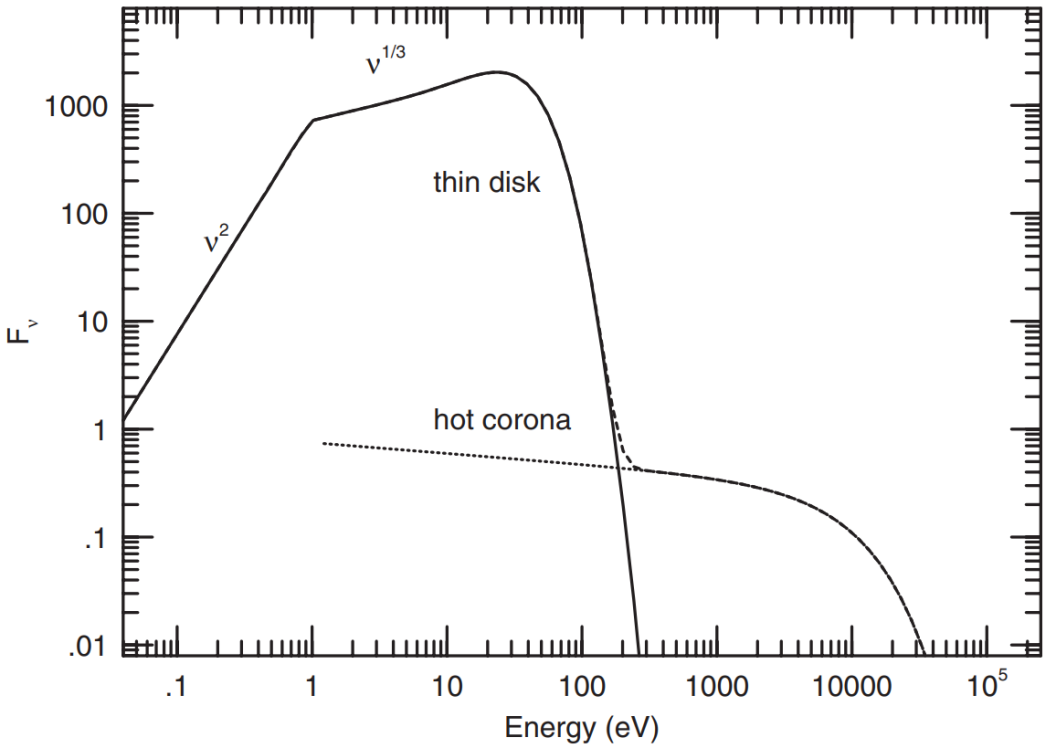

Figure 4.1: Theoretical spectral energy distribution of an active galactic nucleus. The solid line shows the UV disk spectrum ,which breaks around 1 eV, and cuts off exponentially around 12 eV. The dotted line illustrates the cutoff powerlaw spectrum of a possible hot corona above the disk, with its spectrum extending far into the X-ray regime. The dashed line traces the total spectral shape of both components (taken from Netzer, 2013, chapter 4)

4.1.2 Real AGN disks

It is important to remember at this point that the above disk geometry is merely a theoretical approximation. In reality, various physical mechanisms or additional components can alter the structure, chemistry and emission profile of the disk. For example, strong magnetic fields could drive massive winds from the disk, altering the physics and structure of the system altogether (Blandford & Payne, 1982). Another important factor, which will be further discussed in the following section, is the presence of a hot ($T \geq 10^7$K) electron plasma, called *corona*, somewhere in the proximity of the disk. The strong X-ray irradiation from the corona can change the local energy balance of the disk and therefore the emitted spectrum. The physical processes behind these phenomenons will be explained in detail in the following section.

The thin disk approximation itself might also not be applicable to real disks. Above a luminosity of $L/L_{edd} \approx 0.3$, which implies a high mass accretion rate according to Equation 4.1.2, the disk becomes puffed up as the radiation pressure increases, and the concept of a *thick disk* might be better suited to describe the accretion geometry. A thick disk on itself has been found to be thermally unstable (Pringle, 1976), but the scenario was reevaluated after the introduction of an *advection dominated accretion flow* (ADAF) which replaces the inner part of a truncated disk and stabilizes the system (Abramowicz et al., 1995). This inner flow of hot ions with a temperature of ~ 100 keV is often consulted for explaining the X–ray emission of hard state black hole binaries and low or medium luminosity AGN.

In X-ray binaries, at least two different accretion states can be identified: a low/hard state

with a low accretion rate and a mostly truncated disk where the coronal geometry is not quite clear, and a high/soft state with a high accretion rate where the inner edge of the disk extends down to the ISCO. The standard picture is that the inner edge moves closer to the black hole as the accretion rate increases. In some cases, the corona could serve as the base of a jet, which is commonly observed in hard and intermediate states (Markoff et al., 2005). However, the accretion in AGN is not so easily covered. Information about the state can be gained from the Eddington ratio $\varepsilon_{\mathrm{edd}} = L_{\mathrm{bol}}/L_{\mathrm{edd}}$ with the bolometric source luminosity L_{bol}, but $\varepsilon_{\mathrm{edd}}$ is difficult to obtain due to the large uncertainties in mass and distance measurements. Maccarone et al. (2003) suggest that radio-quiet AGN with an Eddington ratio of 5-10 % resemble high-state X-ray binaries in terms of spectrum, but note that more broad-band spectroscopy of this source type needs to be undertaken.

4.2 Components of AGN

In the material surrounding the central accreting black hole, multiple components can be identified. The **Broad Line Region** (BLR) is an arrangement of high density ($10^{10}\,\mathrm{cm}^{-3}$) clouds at a distance of around 0.1 - 1 pc from the black hole in the case of luminous AGN. Since their self-gravity dominates over radiation pressure at these distances, the system is bound. Typical Keplerian velocities in the BLR reach $\sim 3000\,\mathrm{km\,s}^{-1}$ which reflects in the emission line widths due to Doppler broadening, hence the name of the region. Further out, around 3 kpc away from the black hole, low density ($\sim 10^4 cm^{-3}$) clouds from the **Narrow Line Region** (NLR) with typical velocities of $\sim 300\mathrm{km\,s}^{-1}$. The gravitational potential in the NLR is controlled by the mass of the galaxy. Both BLR and NLR form a shape best approximated by a bicone whose velocity field contains both outflow and rotation components. Also relevant may be the **Highly Ionized Gas** (HIG) in the region between BLR and NLR with a very low density that results in high ionization levels. The HIG causes strong absorption and emission features in the X-ray part of the spectrum, and is also called *warm absorber* in X-ray spectroscopy. At radial distances of 0.1 to 10 pc, material containing dust and molecular gas with a density of 10^4 to $10^7\,\mathrm{cm}^{-3}$ form a donut shape called the **Dust Torus**. In some galaxies, this region obscures the emission from the innermost system and the BLR, hence only narrow lines from the NLR are visible in the spectrum. Directly surrounding the black hole is the central **Accretion Disk**; a high density structure that extends up to $1000\,\mathrm{r_g}$ outwards and is, as was argued above, often modelled as an infinitesimally thin, optically thick disk (SS73). The optical-UV continuum of AGN is dominated by the emission from this component. With the disk acting as a dynamo, strong magnetic fields can arise from it and accelerate a **Jet** of material to relativistic speeds along the axis of rotation.

All these components contribute to a complex spectrum of various continua, emission and absorption lines, and other spectral features. A simple illustration of the general AGN setup can be seen in Figure 4.2. This picture also illustrates the explanation of three different types of AGN - blazars, Seyfert I galaxies and Seyfert II galaxies - as the same object viewed from different angles. This is known as the *unified model of AGN*. It was first proposed by Antonucci & Miller (1985) and later developed further by Urry & Padovani (1995). When looking directly from above, the observer sees right into the emerging jet which makes the object appear a multitude brighter than regular galaxies, lending it the name *blazar* (blazing quasi stellar object). A minimally inclined AGN will reveal all of it's component's emission, hence the observer sees broad and narrow lines at the same time. This type of AGN is classified as a *Seyfert I galaxy*. When seen from an edge-on view, the dust torus absorbs the broad line emission from the BLR, leaving only narrow lines in the spectrum so that the AGN is classified as a *Seyfert II galaxy*.

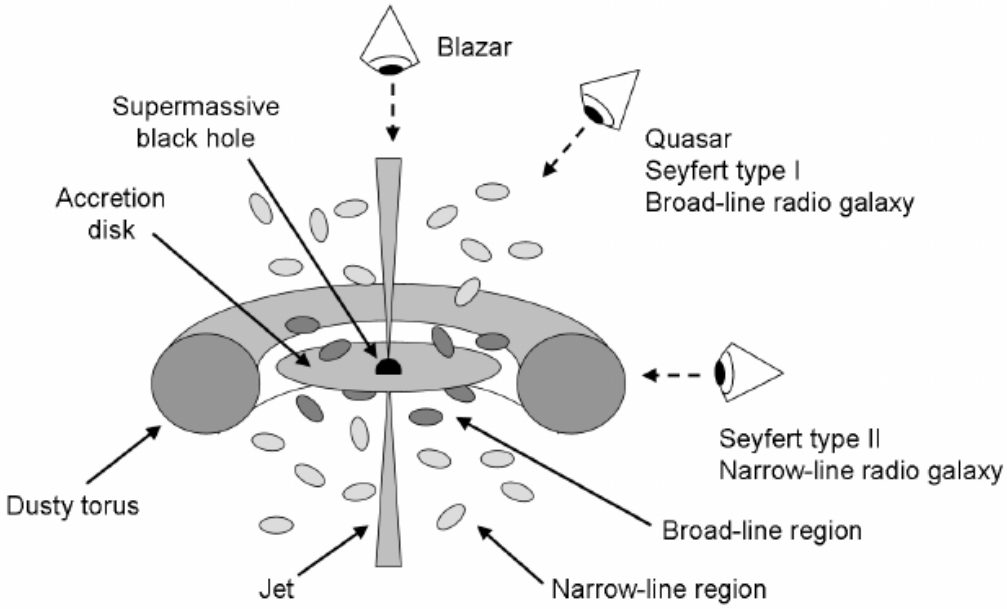

Figure 4.2: Components of an AGN and the types it can be classified as depending on the viewing angle (taken from Zackrisson, 2005).

4.2.1 Corona

In subsection 4.1.1, I argued that the emission of an ideal thin accretion disk around a typical AGN peaks in the UV part of the spectrum. However, many real observed sources exhibit considerable X-ray emission which cannot be explained by the standard disk alone: The Comptonization of soft photons in the disk's atmosphere, which possesses a smaller optical depth than the disk body and therefore a higher temperature and Compton depth, cannot exeed 100 eV for a black hole mass of $M_{BH} > 10^7 M_\odot$, thereby failing to account for the large fraction of energy from AGN that is emitted in the X-ray band of 0.2 to 100 keV. The ADAF scenario was already established as a possible solution to this problem, as well as the existence of a corona above or around the disk. The presence of large-amplitude, short-timescale variations in the spectra of many AGN and X-ray binaries (e.g. Mondal et al., 2023) point towards the fact that the physical object causing the X-ray emission might be considerably smaller than the disk.

In general terms, the corona is postulated as a hot, dilute electron gas in which the soft disk photons are Compton up-scattered and reflected back onto the disk. The Comptonized spectrum, as was derived in chapter 3, takes on the form of a cutoff powerlaw which extends far into the hard X-ray regime (see Figure 4.1). The cutoff energy is posed by the electron temperature, since this is the maximal amount of energy the disk photons can gain from Comptonization in the corona.

Thermodynamical considerations

Haardt & Maraschi (1991) for the first time derived a comprehensive model for two phases - one cool and optically thick, the other hot and tenuous - in thermal equilibrium. In their approach, the tenuous phase identified with the corona is approximated by a uniform plane-parallel slab, as is the cooler accretion disk. Furthermore, the two layers are coupled to each other:

the soft disk emission provides the input for Comptonization in the corona, and the hard Comptionized photons in turn heat up the disk. The system is described by two coupled equilibrium equations,

$$\begin{aligned} (1-f)\,P_{\mathrm{G}} + (1-a)\,L_{\mathrm{dC}} &= L_{\mathrm{s}} \\ f\,P_{\mathrm{G}} + L_{\mathrm{s}} &= A\,L_{\mathrm{s}}, \end{aligned} \tag{4.2.1}$$

for phase 1 and phase 2, respectively. The parameter f denotes the fraction of the gravitational power P_{G} which is dissipated in the corona, as opposed to the rest which is dissipated in the disk. The parameter a describes the fraction of the downward emitted part of the Comptonized luminosity L_{dC} that is not absorbed in the disk, but reflected off it. The third parameter, A, is the Compton amplification factor by which the corona multiplies the soft disk luminosity L_{s} (see Equation 3.1.5).

Limits to optical depth and temperature can be derived when taking pair production into account, which influences the compactness parameter l_{c}, defined as

$$l_{\mathrm{c}} = \frac{\sigma_{\mathrm{T}}}{m_{\mathrm{e}}\mathrm{c}^3}\frac{L}{R}, \tag{4.2.2}$$

where R denotes the radius of the hot phase, L the total emitted luminosity, and σ_{T} the Thompson cross section. The fraction of source specific parameters thereby represents the radiative compactness, i.e. the ratio of emitted luminosity and geometrical extent. With the assumption that no pair escape beside annihilation is allowed, the maximum temperature can be obtained by assuming the minimum optical depth, i.e. a pure pair plasma. For high values of l_{c} (10^2–10^4), the maximum temperature lies in the range of 70–250 keV. Even higher temperatures can be reached for a lower compactness. It is also interesting to note that l_{c} is generally higher for a spherical corona geometry than for a slab-like one, which means that a spherical corona's temperature should at most be below $\sim 250\,\mathrm{keV}$.

Haardt & Maraschi remark that the average spectral slope observed in Seyfert galaxies in the medium X-ray range require practically all power being dissipated within the hot phase. This requirement can be relaxed by introducing a covering factor for the corona, which can easily be provided by adding some of the absorbing components introduced in the beginning of this section to the model.

Geometry

The exact geometry of the corona is still a matter of active debate. In this thesis, the so-called *lamp-post geometry*, where the corona is approximated by a point source at some height h on the rotation axis above the disk, will be a major assumption for modelling X-ray reflection. Even though this assumption is still too simple for accurately describing real coronae, one advantage is that is enables the calculation of a consistent ionisation gradient across the disk. Another advantage of this geometry is the possibility of interpreting the corona as the base of a jet, which has been proven to be possible by Markoff et al. (2005, hereafter M05). A schematic illustration can be found in the top left panel of Figure 4.3.

In the paper of M05, the jet consists of a nozzle region with constant radius closest to the black hole and extends outwards further up, while the particles are being accelerated by the resulting pressure gradient. The hard X-rays emitted from the underside of the nozzle are a mix of Comptonized disk photons and synchrotron photons from higher up along the jet axis. While it has been proven by M05 that the jet model fits the data of galactic X-ray binaries GX 339-4 and Cygnus X-1 equally well as a Comptonized Corona model, the fraction of reflection from the disk has been found to be smaller for synchrotron-dominated X-rays (not

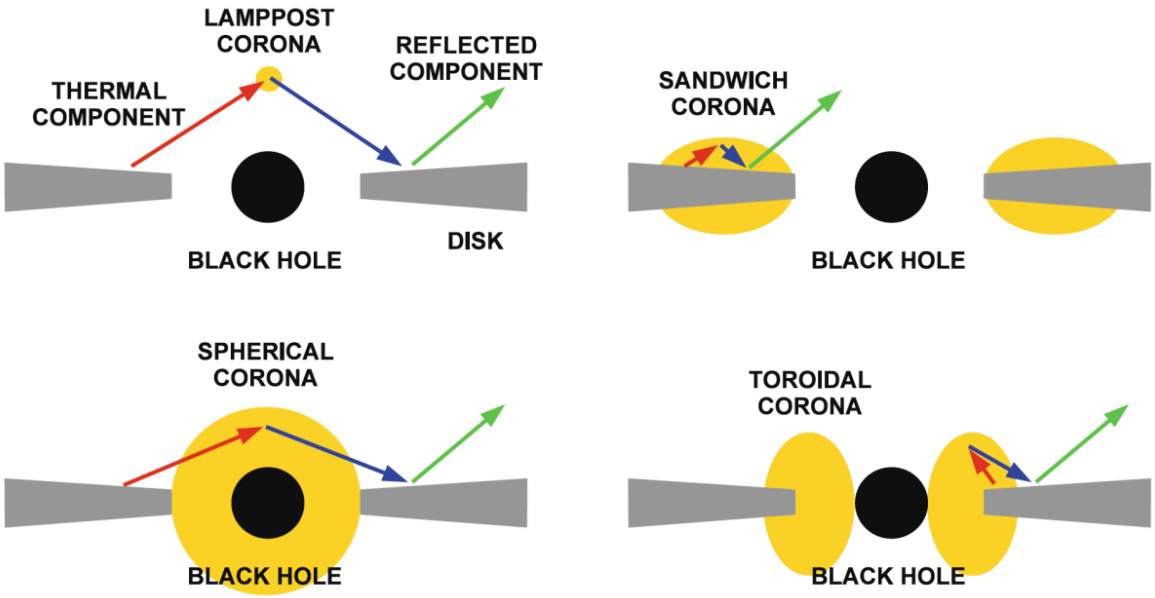

Figure 4.3: Possible coronal geometries. The thermal emission from the disk (red arrow) is Comptonized in the corona (yellow area), emitted again as hard X-ray emission (blue arrow) and finally reflected off the disk (green arrow) (taken from Bambi et al., 2021).

exceeding a few percent) in comparison to Compton dominated hard X-rays, which can reach reflection fractions of up to 20 %. Furthermore, a jet corona model generally implies hotter corona temperatures and steeper soft X-ray slopes due to the synchrotron emission. The universality of the correlation between radio and X-ray flux for accreting sources, regardless of mass, strongly indicates a fundamental underlying physical process for which a jet would be a convenient candidate. However, M05 note that the lack of knowledge regarding jet formation and acceleration makes it hard to formulate a realistic approach. An alternate version to the jet corona theory is the existence of an *aborted jet* above the black hole, which forms when the outflow velocity of the jet material is smaller than the required escape speed. With this, the jet base geometry in general might have gained still more relevance since it was proven that all types of AGN are capable of forming jets (Ghisellini et al., 2004).

Dovčiak & Done (2016) developed a method of estimating the size of a spherical lamppost corona, which was tested on a sample of Seyfert I galaxies, observed by the XMM-Newton satellite with a broad X-ray coverage, in the paper of Ursini et al. (2020) (U20 hereafter). The basic principle assumes that a radiatively compact corona (for which the ratio of luminosity to radius is large), must intercept a certain number of disk photons in order to explain the observed X-ray flux. This then poses a constraint on the solid angle that is subtended by the corona from the viewpoint of the disk. If only a fraction $(1 - \mathrm{e}^{-\tau})$ of the incoming seed photons get scattered in the X-ray band (where τ is the Thomson optical depth of the corona), the radius R_c can be estimated by the expression

$$\pi \left(\frac{R_\mathrm{c}}{R_\mathrm{g}} \right)^2 = \frac{f_\mathrm{X}}{f_\mathrm{BB}} \frac{g_\mathrm{L}}{1 - \mathrm{e}^{-\tau}} \tag{4.2.3}$$

Here, R_g denotes the gravitational radius, g_L is the gravitational energy shift between disk and corona, f_X is the x-ray flux and f_BB the seed photon flux from the disk's blackbody radiation. The equation assumes the conservation of the number of photons, i.e. neglects pair production

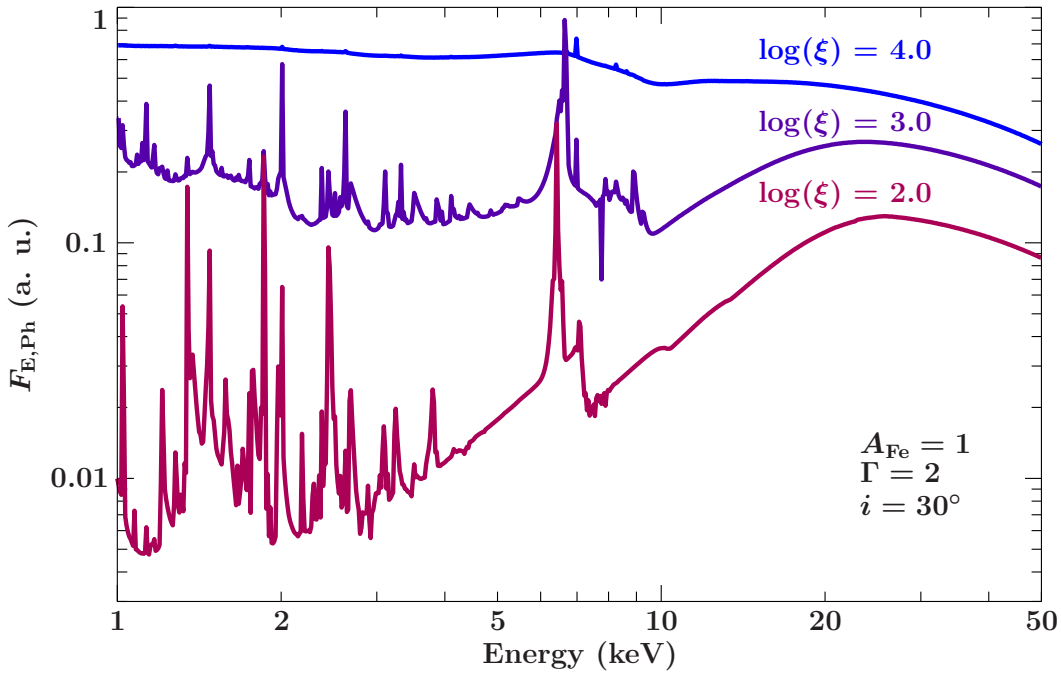

Figure 4.4: X-ray spectra for three different ionization parameter values, produced by the reflection code `XILLVER`. The curves from bottom to top represent a low, intermediate and high ionization regime of the disk. The specta are multiplied by a different constant each for better visibility.

and annihilation, which is reasonable to assume for low plasma temperatures ($T < 511\,\mathrm{keV}$). The coronal plasma temperature was fixed at 100 keV, and τ was inferred from the photon index (e.g. $\Gamma = 1.75$ corresponds to $\tau = 1.2$). U20 additionally account for a correction factor from the MONK code (Zhang et al., 2019) which properly treats the radiative transfer in Kerr space-time. As the ratio of X-ray flux to seed photon flux in Equation 4.2.3 increases, the radius of the corona also grows because it must intercept more photons. Assuming that the corona size should at least be smaller than the distance to the black hole, and the additional condition that the Eddington ratio $\varepsilon_{\mathrm{edd}} = L_{\mathrm{bol}}/L_{\mathrm{edd}}$, with the observed bolometric luminosity L_{bol} of the galaxy, should not exceed unity, U20 found that for a maximally spinning black hole with $r_{\mathrm{in}} = r_{\mathrm{ISCO}}$, the height of the corona can be as small as $2.5\,r_{\mathrm{g}}$, at least for sources with $\varepsilon_{\mathrm{edd}} \leq 0.1$.

Other corona models include the ADAF scenario, where the corona would constitute the hot accretion flow inside the inner disk edge, as illustrated in the bottom two panels in Figure 4.3 (e.g. Iwasawa et al., 2023), or the *sandwich geometry*, where the corona is interpreted as a layer of hot atmosphere covering the inner part of the disk from both sides, as illustrated in the top right panel in Figure 4.3 (e.g. Dobrotka et al., 2023). The corona might also not be in hydrostatic equilibrium, but outflowing. This implies that the geometry can evolve with time, as was observed in some sources (e.g. Wilkins & Gallo, 2015). Another possibility is the coexistence of more than one corona at the same time (e.g. Fürst et al., 2015).

4.2.2 Irradiated disk

The disk of an AGN is assumed to be approximately in a local thermal equilibrium so that its emission can be described as a sum of blackbodies. The corona, on the other hand, emits a powerlaw spectrum with an exponential high energy cutoff. These make up the thermal

and the Comptonized component, respectively. However, the reflected component, which is the coronal emission reprocessed by the disk, still looks different. Compton scattering within the disk changes the shape of the powerlaw, and absorption and re-emission by the disk material removes part of the flux or redistributes it into characteristic emission lines. Moreover, Doppler boosting from the rotation of the disk, gravitational redshift, light bending and photon capture in the vicinity of the black hole alter and blur the observed line profiles. The most notable features in the reflection spectrum are the zoo of fluorescent emission lines below 10 keV, the iron-K-line arount 7 - 10 keV, and the Compton hump at around 30 keV. The latter is formed due to a combination of low energy absorption and the down-scattering of photons with energies larger than $\sim 4\,kT_e$, as was derived in chapter 3.

The X-ray irradiation in such a scenario is strong enough to not only heat, but also ionize the surface material of the disk. From the irradiating X-ray flux F and the electron density of the disk n_e, the ionization parameter

$$\xi = \frac{4\pi F}{n_e} \tag{4.2.4}$$

is derived. With this, the disk ionisation state can roughly be classified into three regimes, as illustrated in Figure 4.4. For **low ionization** ($\log(\xi) < 2$), the main spectral signatures are fluorescence lines of relatively neutral species. In general, the intensity of a fluorescence line depends on a) the abundance of the element in the disk and on b) the fluorescence yield of of the atomic transition in question. The K-shells of the most abundant elements have a $\sim 1\,\%$ yield, while heavier elements have larger yields. For example, the iron K-shell has a fluorescence yield of $\sim 30\,\%$, hence the strongest lines are Fe I - XVII, all located around 6.4 keV. In the **intermediate ionization** regime ($\log(\xi) \sim 3$), only the heavy elements like Fe and Ni still have some electrons left. The prominent iron lines are Fe XXV and XXVI for H-like ions at 6.67 keV and 6.97 keV, respectively. In the **high ionization** regime ($\log(\xi) > 4$), no major features except for a weak iron absorption edge and Compton hump are visible, and the spectral shape approaches the original powerlaw, as the reflected spectrum is mostly a mirror image of the incident spectrum. The large deviation from the initial shape for a less ionized disk can be explained by the fact that many electrons are available for absorbing the flux, which is no longer possible for a highly ionized disk.

4.3 Evolution of AGN

The evolution of galaxies over times is closely connected to the mass growth of the SMBH $\dot{M}$ it hosts in its center. More specifically, M_{BH} is correlated with the mass of the galactic bulge, the stellar velocity dispersion and the total stellar mass of the galaxy. One can therefore speak of a co-evolution between SMBHs and galaxies. All large-scale cosmological simulations need to take black hole growth into account.

The growth rate by accretion is thereby determined by M_{BH} and the available mass supply from the surrounding galaxy. Previously, it was defined in Equation 4.1.2, where η denoted the efficiency with which gravitational potential energy is converted into electromagnetic radiation, defined in Equation 4.1.1. In the most simple case, one could postulate a linear growth

$$\dot{M} = \alpha_{BH} \tag{4.3.1}$$

with the constant α_{BH} being defined according to Equation 4.1.2. Reality, however, is likely more complex. Assuming accretion becomes more efficient with higher mass, a better approximation could be an exponential growth

$$\dot{M} = \beta M \tag{4.3.2}$$

with β denoting the inverse continuous growth time $t_{\rm cg}$, defined as

$$t_{\rm cg} = \frac{1}{\beta} = \frac{t_{\rm Edd}}{1-\eta}\frac{1}{L/L_{\rm Edd}}\ln\left(\frac{M_{\rm BH}}{M_{\rm seed}}\right). \tag{4.3.3}$$

The Eddington time $t_{\rm Edd} = M/\dot{M}_{\rm Edd}$ thereby denotes the typical time associated with the accretion process. $M_{\rm seed}$ denotes the black hole mass before the growing started. The typical growth time for mass growth via thin disk accretion is $\sim 4\times10^7$ yr for black holes accreting at the Eddington limit ($L/L_{\rm Edd} = 1$). However, a continuous growth may still be too simplistic. Depending on the distribution of matter in the innermost galactic region, several growth episodes may take place, where each is separated by long periods of quiescence. The episodes also may differ in η and $L_{\rm bol}$.

Furthermore, accretion is not the only possible way for a black hole to gain mass, and therefore for a galaxy to evolve in scale and shape. When another black hole, together with its host galaxy, is caught in the gravitational potential of the first, a merging event may occur. The growth via mergers is mainly responsible for galaxy growth and change in morphology, especially in cluster environments. The duration of such an event, from the first encounter to the final relaxed state, can take up 10–20 % of the age of the universe at the time of the merger. In the violent final stages, stellar orbits are disrupted, cold gas is compressed, and the galactic morphologies undergo large variations. The rate with which they occur also decreases with time, since the space between galaxies expands. Mergers are therefore more abundant at high redshifts ($z > 2$). In most cases, however, they are likely not important for the growth of a black hole, as the mass of the secondary black hole will only be a small addition to the main black hole. Mergers of equal mass are rare (Farah et al., 2023).

4.3.1 Black hole spin evolution

In the beginning of this thesis, I argued that due to angular momentum conservation, the growth of a black hole also results in a change of its spin parameter. Indeed, it has been proposed that, on the one hand, long periods of undisturbed prograde accretion lead to an efficient spin up, eventually resulting in a maximally spinning black hole (Bardeen, 1970). Chaotic accretion of matter with randomly oriented angular momentum, on the other hand, slows the spin towards $a \sim 0$ over a sufficiently long time (e.g. Dotti et al., 2013). SMBH-mergers can leave remnants which are either spun up or down, depending on the individual spin parameters during merging (e.g. Hofmann et al., 2016). It is therefore expected that different growth histories, either being accretion dominated, or containing accretion and merger events equally, leave a distinct imprint on the overall spin distribution of black holes in the universe.

Modeling the spin distribution of SMBHs is a difficult task. One of the current available models is *Horizon-AGN* (Dubois et al., 2014), a suite of cosmological, hydrodynamic simulations performed with the RAMSES code (Teyssier, 2002) for calculating spin evolution, starting with $a = 0$. However, the enormous size scales of accretion gas flows and feedback mechanisms, spanning hundreds of kpc, render the computation unfeasible with up-to-date numerical models and hardware. Instead, models use subgrid-prescriptions which rely on astrophysical scaling relations to predict large scale hydrodynamic effects from the physics at smaller scales. As the field of spin modeling in a full cosmological context is still in its infancy stage, results are likely to improve once better constraints for subgrid parameter tuning are found.

Beckmann et al. (2023), using a sample produced by Horizon-AGN, found that galaxies evolved in the absence of mergers host SMBHs with a preference for higher spin values than

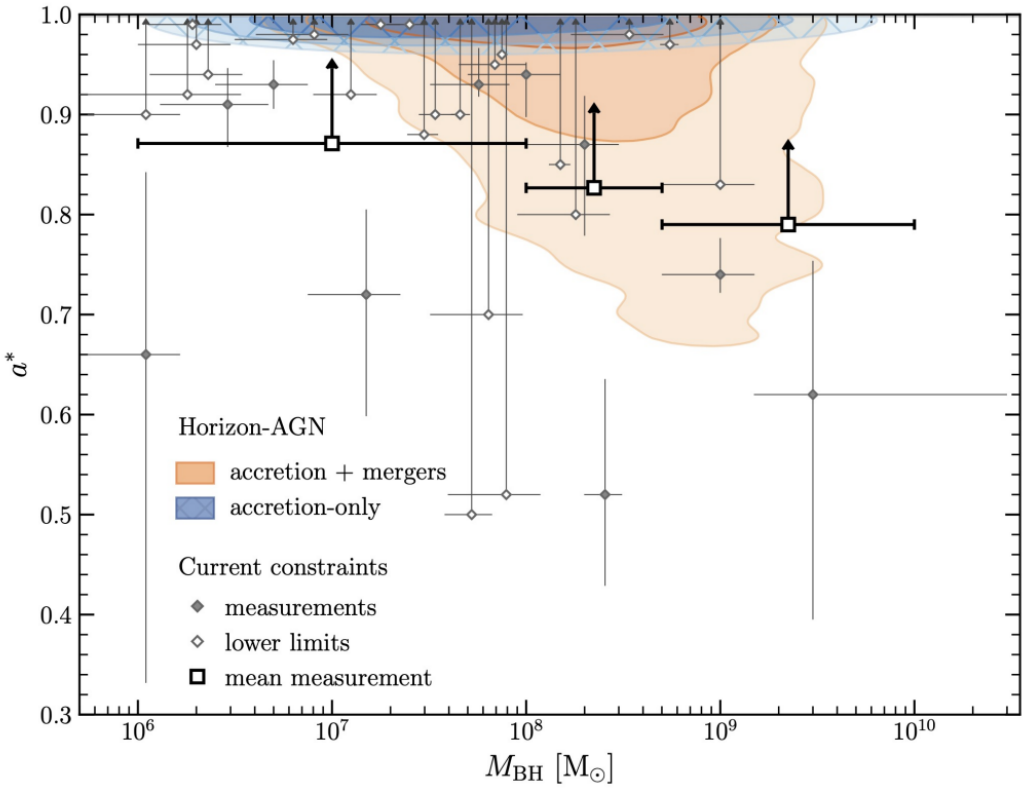

Figure 4.5: Spin-mass plane for SMBHs, comparing measurements and simulations. Current observational constraints are marked as open and filled grey diamonds. The confidence contours indicate the parameter space occupied by Horizon-AGN simulation samples for $M_{\rm BH} > 10^6\,M_\odot$. The orange contours represent accretion/merger driven sources, the blue contours represent accretion-only sources (taken from Piotrowska et al., 2023).

those with mergers in their growth histories with $>5\,\sigma$ significance. More specifically, they categorized their sample by the fraction of mass gained through merger events, $f_{\rm BH,merge}$, into accretion-only samples ($f_{\rm BH,merge} < 0.1$) and accretion/merger samples ($f_{\rm BH,merge} > 0.1$). The former category showed a narrow spin distribution peaking at the maximally allowed spin value. The latter distribution also slightly peaked at the maximum value, but almost approximated a flat uniform distribution.

4.3.2 The spin-mass plane

Relativistic reflection modeling, which will be introduced in detail in the next chapter, is a widely used tool for estimating the spin of an accreting black hole of any size. Measuring the mass of a SMBH, which ultimately determines the size scale of the AGN, is less straightforward. The most common method is reverberation mapping of broad emission lines (e.g. Peterson, 1993). Here, the mass is estimated from the proportionality

$$M_{\rm BH} \propto D_{\rm BLR}(\Delta V)^2, \tag{4.3.4}$$

in which ΔV is the line-of-sight velocity of gas from the BLR inferred from the emission line profiles, and $D_{\rm BLR}$ is the distance between the black hole and the BLR, inferred from time lag measurements of variations in the continuum and the line emission. Alternatively, the

mass can also be empirically inferred from the relation between black hole mass M_{BH} and stellar velocity dispersion σ_* in the galactic bulge of known samples (e.g. Saglia et al., 2016).

Using the same conditions for their Horizon-AGN samples as Beckmann et al. (2023) and categorizing them in the same way, but taking the mass into account, Piotrowska et al. (2023) found that accretion-only and accretion/merger populations differ the most for $M_{\mathrm{BH}} > 10^8\,M_\odot$. Figure 4.5 shows the spin-mass distribution of the simulated populations (contours) and the currently available measured sources (points with error bars). Indeed, from the means of the measurements, it seems like low mass SMBHs ($M_{\mathrm{BH}} = 10^6$–$10^7\,M_\odot$) show evidence for higher spins than the high mass candidates ($M_{\mathrm{BH}} > 10^8\,M_\odot$). However, only a small number of measured sources exist in this regime. For differentiating between growth histories of SMBHs, it is therefore necessary to better map out the spin-mass plane. Refining spin measurements by requiring more strict physical conditions for reflection models can help in this process.

5 Modeling relativistic reflection

The ultimate goal of X-ray spectroscopy is to estimate the parameters of an astrophysical object, since it is impossible to resolve it spatially. Therefore, astronomers need, at best, all-encompassing theoretical models of all involved processes which generate and alter the observed spectrum. Modeling the highly relativistic reflection of photons on an accretion disk in the vicinity of a heavy body specifically has proven to be useful for understanding accreting objects. These models, of course, should be as physically motivated as possible, since empirical modeling is only a substitute tool for when the real physical processes are not yet understood properly. The new model presented and tested in this thesis thereby is a more physical version of an already existing reflection model, which for the first time takes the measured luminosity of the corona into account and calculates the ionisation level of the disk with it.

In the following, the history and general methods of relativist reflection modeling shall be summarized briefly, following the paper of Bambi et al. (2021). Then, the model in question, followed by its rectified version, will be explained in more detail.

5.1 History

The Fe-Kα line is the most prominent line in astrophysical reflection spectra (see chapter 3). The first models therefore consisted of simply this line, which was broadened and skewed by relativistic effects, on top of a powerlaw continuum. Available line models at that time were `DISKLINE` for a non-spinning black hole (Fabian et al., 1989) and `LAOR` for a maximally spinning black hole (Laor, 1991). Later, also models for variable spin were developed: `KERRDISK` (Brenneman & Reynolds, 2006), `KYRLINE` (Dovčiak et al., 2004) and `RELLINE` (Dauser et al., 2010). However, since the softer emission lines, the Compton hump and other spectral features also need special modeling, only the inclusion of all relevant atomic transitions and radiative interaction processes allowed proper modeling of the whole reflection spectrum. The most advanced models up to date are `REFLIONX` (Ross & Fabian, 2005) and `XILLVER` (García & Kallman, 2010; García et al., 2011, 2013). The latter is considered the most accurate model available, since it incorporates an extended atomic database via the photoionization routines of the XSTAR code (Kallman & Bautista, 2001). As these models only give the directly emitted reflection spectra, they have to be convolved with relativistic blurring kernels in order to fit the observed spectra; examples are `KDBLUR(LAOR)` or `RELCONV(RELLINE)`. Most of these models assume that the photons are emitted under the same angle as the disk is viewed.

Compared to the previous practice of only fitting the broadened iron emission line, the full relativistic reflection models are a major improvement. In reality, however, the observer sees photons for emission angles other than the viewing angle due to the strong lightbending in the vicinity of the black hole, thereby seeing a superposition of multiple spectra from various angles. Also, the distribution of emission angles in the restframe of the disk impacts the spectral profile: for example, uncertainty in the angular distribution leads to uncertainties of up to 20% on the estimate of the position of the inner disk edge, and therefore on the spin measurement (Svoboda et al., 2009). Furthermore, simulations have shown that isotropic or other simple emission laws might differ significantly from the actual distribution. In

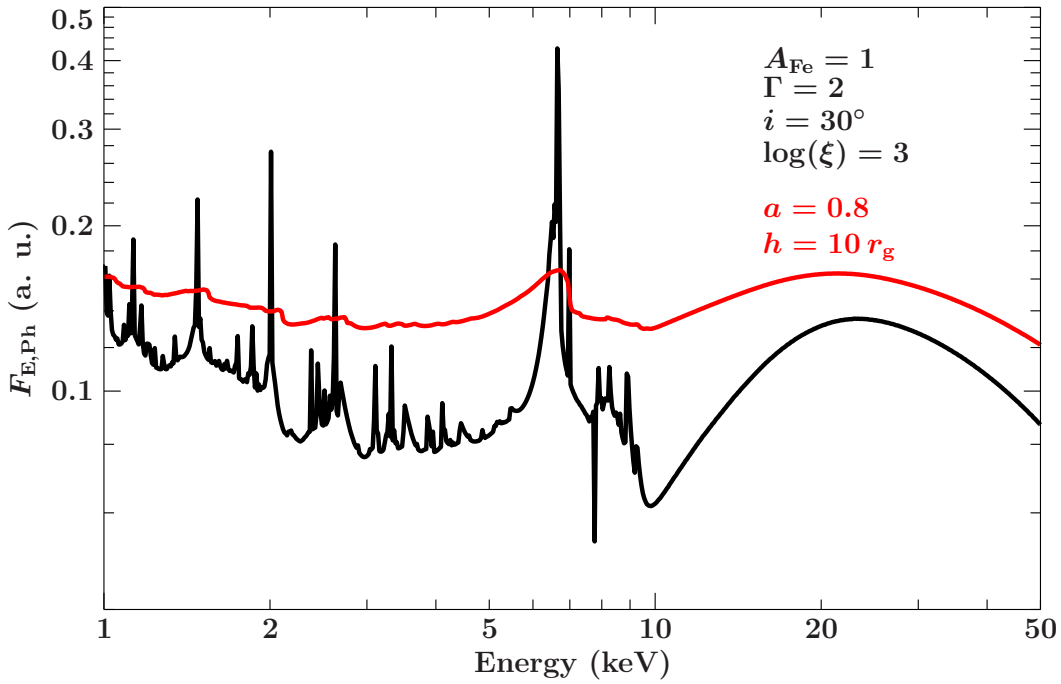

Figure 5.1: Disk reflection spectra with (red) and without (black) relativistic blurring in the lamppost geometry, produced by the reflection models `RELXILLLP` and `XILLVER`, respectively.

order to take the angular intricacies into account, the model `RELXILL` (Dauser et al., 2013) intrinsically combines the reflection spectrum of `XILLVER` and the relativistic blurring of `RELCONV`. Other models, which are specialized on some aspect of spectral modeling, are, for example, `KYN` (Dovčiak et al., 2004), `REFLKERR` (Niedźwiecki & Życki, 2008) and `RELTRANS` (Ingram et al., 2019), yet `RELXILL` is the most popular reflection model up to date. Both broken powerlaw irradiation and the lamppost geometry can be chosen for `RELXILL`, the latter being implemented in the model extension `RELXILLLP`. However, all previously mentioned models use a series of fundamental theoretical concepts to describe basic components of the AGN system.

5.2 Modeling methods

General parameters and properties of an accreting astrophysical object can only be inferred by correctly calculating the photon paths from the corona to the accretion disk, and subsequently the paths from the emission point on the disk to the detection point inside the observer's flat space. Since the space around the black hole is strongly influenced by general relativistic effects, calculations also have to take into account gravitational redshift, lightbending and other metric effects, which all influence the photon trajectories to some extent and produce broadened asymmetrical line profiles with a red wing that extends far into low energies. The more rapidly the black hole is spinning, and the closer the inner disk edge is located to the black hole according to Equation 4.1.3, the more emphasized the relativistic effects will be. From the shape of the distorted spectrum one can in turn estimate the system's parameters, like spin, inclination or ionization. Furthermore, the rotation of the disk will redshift the part of the photons which are emitted from the receding half of the disk, and blueshift the photons from the advancing half, creating a characteristic two-horned Doppler line profile. The shape

of the full X-ray spectrum with (red curve) and without (black curve) the relativistic blurring effects is illustrated in Figure 5.1 for a black hole spinning with $a = 0.8$, and a point source corona a height $h = 10\,r_\mathrm{g}$ along the spin axis. These theoretical spectra can, of course, only sufficiently describe real astrophysical objects when every part of the accreting system is modeled in great detail.

5.2.1 Reflection spectrum

For inferring the intensity I_e emitted in the rest frame of the disk from the flux F_o seen by the observer, the measured specific intensity I_o is integrated over the angular extent of the accretion disk image in the observer's sky:

$$\begin{aligned} F_\mathrm{o}(E_\mathrm{o}) &= \int I_\mathrm{o}(E_\mathrm{o}) d\Omega \\ &= \frac{1}{D^2} \int_{R_\mathrm{in}}^{R_\mathrm{out}} \int_0^1 \frac{\pi r_\mathrm{e} g^2}{\sqrt{g^*(1-g^*)}} f(g^*, r_\mathrm{e}, i)\, I_\mathrm{e}(E_\mathrm{e}, r_\mathrm{e}, \vartheta_\mathrm{e})\, dr_\mathrm{e} dg^* \end{aligned} \tag{5.2.1}$$

The right hand side can be calculated by integrating the emitted intensity per radius r_e and emission angle ϑ_e over the radial disk extent, and the *transfer function* f (Cunningham, 1975). The latter contains the Jacobian between the observer's Cartesian coordinates and the specific integration variables, and also depends on the viewing angle i, integrated over a modified redshift parameter

$$g^* = \frac{g - g_\mathrm{min}}{g_\mathrm{max} - g_\mathrm{min}} \tag{5.2.2}$$

as well. Here, g_min and g_max are the minimally and maximally possible redshifts, respectively. E_o and E_e are the photon energies as seen from the rest frame of the observer and the disk. In order to solve this equation, the transfer function is often calculated using ray-tracing techniques.

For calculating the reflection spectrum, the radiative transfer equation (describing the radiation field at every point in the disk), the level population of all relevant ions (which determines the ionization state of the disk) and the energy equation (which provides the local temperature) have to be known, additional to the disk density, which can be gained from e.g. magneto-hydrodynamic simulations. The resulting set of coupled equations is solved by applying iterative procedures and yields the full reprocessed reflection spectrum.

5.2.2 Corona

The normalization of the reflected spectrum is largely determined by the geometry of the X-ray source, which determines the illumination pattern. As the exact geometry has never been determined for any source, two different approaches for modeling the emissivity ε as a function of the disk radius are commonly applied. The first uses a broken powerlaw with $\varepsilon \propto r^{-q_\mathrm{in}}$ for the inner part $r < R_\mathrm{in}$ and $\varepsilon \propto r^{-q_\mathrm{out}}$ for the outer part $r > R_\mathrm{br}$ of the disk. Here, R_br is the characteristic break radius. Outer emissivity indices have been found to approach $q_\mathrm{out} = 3$, while the inner emissivity is very steep for many sources (e.g. Wilms et al., 2001), predicting $q_\mathrm{in} = 5 - 10$.

The second approach, which assumes a lamppost geometry with an isotropically emitting point source directly on the spin axis, intrinsically predicts steep inner emissivities due to the highly compact geometry, while simultaneously fulfilling the limit of $q = 3$ for larger radii. It was first discussed by Matt et al. (1991) as a part of Monte Carlo simulations for different corona and disk geometries. The broken powerlaw approach, as opposed to the lamppost approach, is purely phenomenological and requires no intrinsic assumption about

the corona geometry. It is therefore more broadly applicable, while the lamppost geometry is more physical, but requires strong assumptions about the accretion geometry. Furthermore, it allows for a physical interpretation and direct fitting of the fraction of reflected flux w. r. t. direct flux measured by the observer.

Is should be noted, however, that the point source lamppost is still a simplification of even the most compact coronae. In reality, the X-ray emitting source should have a radial extend, might be moving or accelerating when viewed as a jet, or might even exhibit non-isotropic emission from, e.g., a corona moving at relativist speed, or an elongated or patchy geometry.

5.2.3 Accretion disk

The standard way of describing the disk itself is by using the Novikov-Thorne model (Novikov & Thorne, 1973). Thereof, the three-phase density gradient model of Shakura & Sunyaev (1973) is derived, in which the vertical extend of the disk is negligible in comparison to the radial extent (thin disk approximation) and the gas retains a Keplerian motion. The physics of such a thin disk was covered in chapter 4. Furthermore, the deviations of space-time from the Kerr metric due to the presence of an accretion disk are very minor in most cases, and are therefore often neglected. In many models, the disk is assumed to have a constant vertical density and be cold (i.e. to not emit thermal radiation). Both assumptions can well be justified for very thin disks and high energy X-ray spectra, as well as for AGN where the low energy emission is absorbed by covering clouds and dust.

Most of these assumptions, of course, lose their applicability when the accreting system is in an altered state, i.e. when the disk is thick, maybe truncated, and where a significant amount of its emission could stem from the plunging region. More specifically, if the inner disk edge is wrongly assumed to extend down to the innermost stable orbit ($r_{\mathrm{in}} = r_{\mathrm{ISCO}}$), the spin is very likely overestimated. However, the systematic error on the spin parameter decreases as the actual spin increases, since this brings the inner edge closer to the black hole. Nevertheless, a thorough assessment of the accreting state of the object in question is necessary for making sure that the fit will yield significant results.

5.2.4 Second order effects

In the case of a truncated disk, photons from the bottom of the disk or photons which circle the black hole multiple times might traverse the plunging region and reach the observer, thereby creating higher order disk images (Zhou et al., 2020). This effect, however, is negligible for high accretion rates where $r_{\mathrm{in}} \approx r_{\mathrm{ISCO}}$.

A similar effect is the secondary spectrum of reflected radiation which is bent so strongly by the relativistic effects that it is reflected again on the disk. Naturally, this so-called *returning radiation* will mostly be relevant for rapidly spinning black holes, for which the lightbending is strong, and for highly focused irradiation. First conceived by Cunningham (1976), the process can be seen as a radial redistribution of the reflected spectrum. For a neutral disk, returning radiation mostly impacts the spectrum around 10 keV (Niedźwiecki et al., 2016). For ionized reflection (but neglecting effects of relativistic transfer of radiation), the spectrum which includes returning radiation resembles a standard reflection spectrum with higher ionization and significantly higher iron abundance (Ross et al., 2002). New research has shown that returning radiation has the strongest influence on the reflected flux in the case of a rapidly spinning black hole and a compact disk-corona geometry, making up 40 to 80 % of the total observed flux (Dauser et al., 2022). Mainly, returning radiation leads to a flattened emissivity profile and enhances the reflected flux, because it recovers part of the flux that is lost to

gravitational redshift. In any case, the effects of returning radiation are highly dependent on the other parameters of the system and should be studied for each object individually.

Lastly, some part of the reflection spectrum might be intercepted by the corona a second time and undergo Comptonization. When this reflection Comptonization is ignored, the fraction of reflection in the total spectrum might be significantly underestimated (Steiner et al., 2017). The line profiles can also be altered by this process, additionally to the relativistic broadening. But since the effectiveness of interception is largely dependent on the radial extend of the corona, reflection Comptonization likely plays no role in systems where the lamppost approximation is a good fit.

5.2.5 Galactic absorption

After the X-ray radiation is emitted by a certain physical process in the source, it encounters the cold intragalactic and interstallar medium (IGM, ISM), which results in partial absorption. The total photoionisation cross section σ_{ISM} of the ISM is composed of the cross sections for each relevant phase (gaseous, molecular and grain phase), following $\sigma_{\mathrm{ISM}} = \sigma_{\mathrm{gas}} + \sigma_{\mathrm{mol}} + \sigma_{\mathrm{grain}}$. In standard X-ray applications, this expression is often normalized to the total hydrogen number density N_{H}, so that the observed X-ray intensity can be written as (Wilms et al., 2000)

$$I_{\mathrm{obs}}(E) = \mathrm{e}^{-\sigma_{\mathrm{ISM}}(E) N_{\mathrm{H}}} \, I_{\mathrm{source}}(E). \tag{5.2.3}$$

Depending on the location and distance of the observed source w. r. t. the Earth, the exact magnitude of galactic absorption has to be taken into account when modeling a photon spectrum.

5.2.6 Open questions: soft excess and supersolar iron abundance

On top of the well known components, also unknown features may appear. The most prominent one in X-ray spectroscopy is the so-called *soft excess*, which is a surplus in flux below 2 keV that cannot sensibly be explained by the standard reflection models. The two main scenarios currently discussed are blurred ionized reflection (e.g. Xu et al., 2021), in which the emission line forest at low energies in neutral disk reflection spectra accounts for the soft excess, and Comptonization in an additional warm corona (e.g. the optically thin disk atmosphere), which is only thermally stable if Compton cooling dominates over bound-free emission, and which requires anomalous heating mechanisms to account for the necessary temperature (Kawanaka & Mineshige, 2023). The blurred reflection excess can be achieved by disk densities higher than the usually assumed $10^{15}\,\mathrm{cm}^{-3}$ in spectral models, since the major effect of higher densities on the spectrum is a significant increase in flux below 3 keV due to an increase in gas temperature (García et al., 2016).

Since the density also affects the spectral shape around the iron line region, the density parameter could be correlated with the iron abundance in some spectral models. This could be connected to the problem of an overall high iron abundance of a few solar abundances found in many sources (see García et al., 2018, for a review). The most extreme candidates, like the AGN 1H0707-495, reach abundances of $A_{\mathrm{Fe}} \sim 10$–20 solar abundances (Fabian et al., 2009). No physical mechanism for this extreme enrichment of iron has been identified yet, and it is generally accepted that this bias towards supersolar iron abundances is most likely unphysical. Moreover, spin estimates are driven by the shape of the iron-K emission line and absorption edge, and are directly influenced by the iron abundance parameter. Because of this, the reflection modeling process is currently reevaluated.

5.3 Modeling in the lamppost geometry

The model flavor `RELXILLLP` from the `RELXILL` model family (Dauser et al., 2013; García et al., 2014) is calculated in a lamppost geometry with the motivation of possibly interpreting the point-like corona as the base of a jet. The emissivity at a particular radius on the disk in this geometry is parametrized as

$$F(r, h) \propto r^{-\varepsilon(r)}. \tag{5.3.1}$$

The strong focusing on the inner disk parts produces a steeper emissivity (i.e. larger values of ε) for small radii, though it converges to its flat space value $\varepsilon = 3$ for larger radii (Dauser et al., 2013). The closer the source is located above the black hole, the faster the convergence. The steepening itself is almost independent of the source height, but strongly depends on the relativistic boosting and especially on the photon index of the primary continuum. The inner emissivity is indeed only steep ($\varepsilon > 8$) if the incident spectrum is very soft ($\Gamma > 2.5$), even for rapidly spinning black holes (Dauser et al., 2013). For a maximally spinning black hole and a hard spectrum with $\Gamma = 1.7$, the emissivity reaches at most $\varepsilon \sim 4$, not far from the flat space value.

The photon trajectories, which are defined by the emission angle δ from the point source, are ray-traced from their point of emission (h, δ) to their incident location $(r_\mathrm{i}, \delta_\mathrm{i})$ on the disk. They are influenced by various relativistic effects. The area contraction of a unit ring dr on the disk due to its relativistic rotation, as seen from the rest frame of the emitting source, leads to a decrease of the incident flux proportional to the disk's angular four-velocity v^ϕ; likewise, a decrease in flux is attributed to the extension of the proper area near the black hole as an effect of the Kerr metric. A geometric focusing of the photons towards the black hole leads to an increase in flux for small radii. Additionally, the photons are gravitationally blueshifted by falling into the black hole's potential well. The largest enhancement of flux, however, is controlled by the photon index of the incident spectrum, as was already the case for the emissivity: for a maximally spinning black hole, a soft spectrum can enhance the flux at the inner edge by a factor of up to 100. While a low source height also increases the irradiation of the inner disk part, it mostly influences the outer regions, where the disk receives almost no flux for very low sources ($\mathrm{h} < 2\,\mathrm{r_g}$). A very large source height ($h \sim 100\,r_\mathrm{g}$) produces a flux which is constant for large parts of the disk and only falls and rises lightly at the outer and inner edges, respectively. By accounting for these effects, the incident flux can be calculated for every radius.

5.3.1 Resolving the emission angle

According to García et al. (2014), it is apparent that the reflection spectrum is strongly influenced by the angle under which the observer views the disk. For larger inclinations, a distant observer will see more photons which took part in a higher number of scatterings, and therefore more high energy photons, which mostly contribute to the Compton hump. This region is therefore affected most by the viewing angle. However, since different line features are produced at different depths in the disk, these are also affected by the effective optical depth, which is the actual optical depth projected along the line of sight. More specifically, heavy elements like Fe or Ni sink deeper into the disk so that their emission lines will appear weaker for grazing angles than those of light surface elements like C, N or O. Additionally, the angular effects for the line features are stronger for neutral disks, since the opacity for photoelectric scattering is larger in this case.

The emission angle of the reflected photons is only identical to the viewing angle for a non-relativistic system. With the effect of lightbending, the observer catches photons that were emitted under various angles, therefore actually seeing a superposition of spectra with

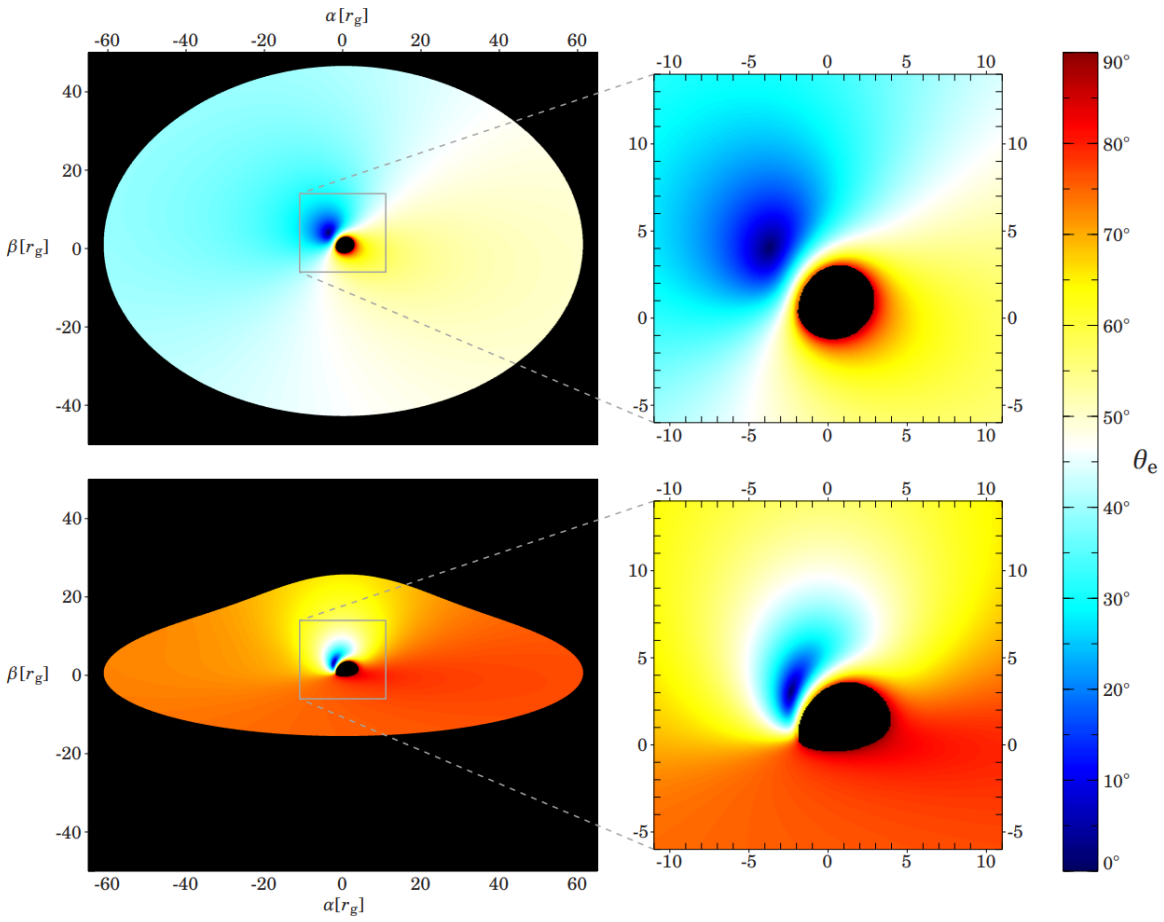

Figure 5.2: The angular distribution in an accretion disk around a black hole indicated by a color gradient. The disk is shown for inclination i = 45° (upper panels) and for inclination i = 75° (lower panels). The plots on the right show the zoomed-in innermost regions of the disk (taken from García et al., 2014).

different inclinations. In Figure 5.2, the change of emission angle over the extent of the disk is visualised in a color-coded plot. For large radii, the emission angle tends to align with the viewing angle; in the region close to the black hole though, all possible emission angles reach the observer due to the strong lightbending. This is especially important for a low lamppost geometry, since the flux is greatly focused onto this inner region. As a result, the distribution of emission angles increasingly peaks around the viewing angle for low inclination; for larger inclinations, it approaches a uniform distribution.

In the past, the reflection spectrum of `XILLVER` was convolved with the relativistic blurring kernel `RELCONV`. The improvement of `RELXILL` consisted of implementing a proper angular treatment: it takes the reflection spectrum for each point on the disk into account and convolves it according to its position on the disk, weighted by the irradiation of the chosen profile (García et al., 2014). Previously, a *limb* parameter had to be artificially added to the model in order to accomodate for the observed increase in brightness for high inclination angles in some sources; relxill now intrinsically predicts a significant limb-brightening for mildly ionized disks ($\log \xi \sim 2$), and an almost isotropic emissivity, e.g. no limb effects, for high ionization ($\log \xi > 3$). Physically, this is explained by the fact that for high ionization, electron scattering is the dominating interaction process in the disk. This produces no emission

lines and is therefore independent of the viewing angle, or, in other words, produces isotropic emission. Therefore, the previous convolutional approach had the same effect as simply averaging over all emission angles.

The deviations between the simple convolutional model and `RELIXLL` will at most be 30 % for a large source height. For a source close to the black hole, however, the difference will be below 10 %, as the strong focusing in this case mostly illuminates the inner disk part where the photons are emitted under all possible angles; the angle-averaged approach is therefore mimicked best by a low source height. In an analysis by García et al. (2014), it was nonetheless shown that in a standard system with low source height ($h = 3\,r_\mathrm{g}$, $\Gamma = 2$, $A_\mathrm{Fe} = 1$), the iron abundance might be overestimated by a factor of more than 2 for low inclinations, high spin and a neutral disk. Furthermore, the spin might be underestimated by up to 20 % for low inclinations and a highly ionized disk; a non-spinning black hole might even be found to be maximally spinning when inclination and ionization are high.

The improvement of `RELXILL` also poses a direct constraint on the so-called *reflection fraction*, R, which in the lamppost geometry has a physical interpretation. It is defined as the ratio between the part of the flux that actually hits the accretion disk, and the part that escapes into infinity:

$$R := \frac{f_\mathrm{AD}}{f_\mathrm{INF}} = \frac{\cos\,\delta_\mathrm{in} - \cos\,\delta_\mathrm{out}}{1 + \cos\,\delta_\mathrm{out}} \tag{5.3.2}$$

Here, δ_in and δ_out denote the incident angle at the inner and outer edge, respectively. Some part of the flux also might disappear inside the black hole, described by $f_\mathrm{BH} \propto 1 - \cos\,\delta_\mathrm{in}$. For a disk in flat space, exactly half of the coronal flux would be reflected. The reflection fraction therefore converges to 1 for large radii in a relativistic system. Closer to the black hole, the relativistic beaming reduces the escaping flux and enhances the reflected component. At the innermost radii, photon trapping by the black hole reduces the reflected flux again. It follows that R exhibits a radial maximum R_max which is dependent on the black hole spin. The broadening of the spectral features is therefore dominated by the emission from the region around this maximum. For a low source height and high spin, R_max can reach values of up to 20; for lower spins and larger inner edge radii, the maximal R is considerably smaller. Additionally, R_max can be used to exclude unphysical spin parameters, i.e. constrain the parameter space, and subsequently reduce the uncertainties on the spin estimate.

5.4 Introducing self-consistently calculated ionization

Following Equation 4.2.4, the radial change in flux, which is known from the assumed lamppost profile, and the density gradient introduced in the previous chapter imply a radial ionization gradient. The radial gradient is not the only ionization effect though. The angle under which the irradiating photons are intercepted by the disk also influences the reflection spectrum and with it the vertical ionization structure of the disk. Due to the change in effective optical depth, the intensity of incident radiation can be written as a function of the incident angle δ_i (García & Kallman, 2010):

$$I_\mathrm{inc} = \frac{2n_\mathrm{e}}{4\pi}\frac{\xi}{\cos\,\delta_\mathrm{i}} \tag{5.4.1}$$

For a perpendicular incidence ($\delta_\mathrm{i} \sim 90°$), the intensity is minimal but deeper layers of the disk can be reached by the ionizing radiation, whereas maximal heating of the surface but lower temperatures in deeper regions are achieved by grazing incident angles ($\delta_\mathrm{i} \sim 0°$). Aside from the viewing angle, these effects naturally affect the emission line features according to the depth at which they are produced in the disk. Moreover, the incidence angle's radial distribution shows a minimum which becomes narrower and is shifted towards smaller radii as

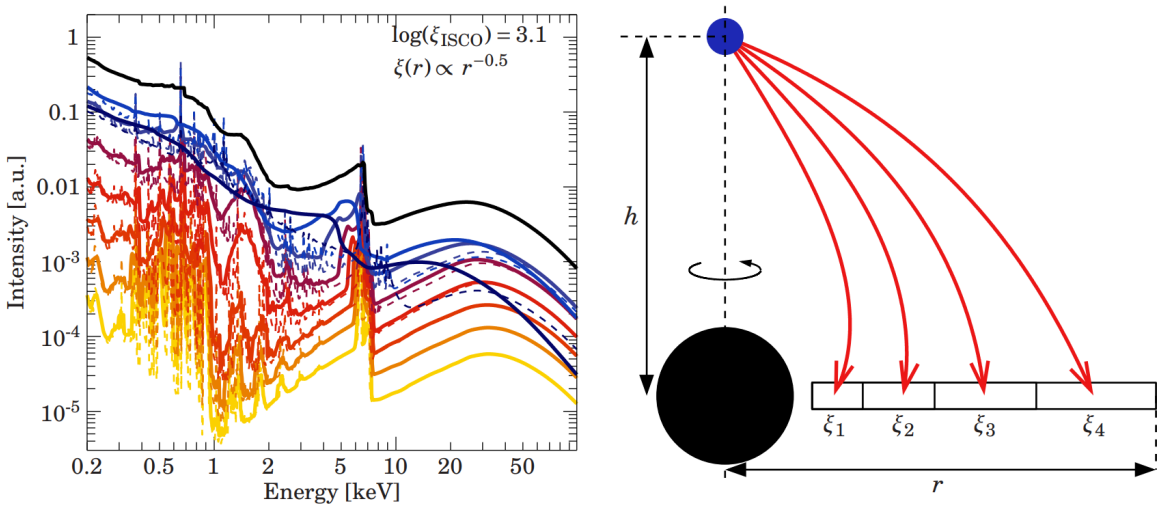

Figure 5.3: Ionization gradient (right) and spectra for different ionization regimes (left) (taken from Dauser, 2014).

the height of the emitting source decreases, indicating that the vertical gradient also changes significantly with radius. Varying the incident angle in a range of 25–80° can, for example, be compensated by changing the ionization by more than a factor of 5 (García & Kallman, 2010). The gradients give rise to a complex ionization structure, hence it is necessary to subdivide the disk into different radial ionization regimes. This concept is illustrated in Figure 5.3. The relxill extension `RELXILLLPCP` allows for an empirical powerlaw ionization gradient with the index p as a free parameter, or implements the intrinsic gradient for the α-disk density model (Shakura & Sunyaev, 1973). While the latter is more physical for specific sources and overall more consistent, the former is more widely applicable and allows for fitting ionization gradients to sources for which the α-gradient may not apply.

In the currently available version of `RELXILL`, the absolute (maximal) value of the ionisation ξ is a free parameter as well. However, as the primary flux can be inferred from the reflection fraction in the lamppost geometry, and as the mass of the black hole, as well as the distance of the source from the observer, are known for many sources, the ionization state, too, can be intrinsically calculated for each region in the gradient, as the following section will demonstrate. The new version of `RELXILL`, which implements a self-consistently calculated ionisation, will be referred to as `RELXILLLPALPHA` (or more simply, the *Alpha model*; I will use these terms interchangeably).

5.4.1 Estimating the ionization at the inner edge

Following Dauser et al. (2013), the gravitational energy shift a photon undergoes when traveling from the corona to its incident location on the disk is defined as

$$g = \frac{E_\mathrm{i}}{E_\mathrm{e}}, \tag{5.4.2}$$

where E_e is the photon energy at the point of emission, and E_i is the photon energy at the incident point. The incident photon flux can then be calculated as

$$N_\mathrm{i} = N_\mathrm{e} \cdot g^\Gamma. \tag{5.4.3}$$

Here, N_e is the emitted photon flux as seen from the restframe of the accretion disk, and is assumed to follow a powerlaw distribution, $N_\mathrm{e} = E_i^{-\Gamma}$. In both cases, Γ is the photon index

of the emitted spectrum. If one now postulates that the number of photons is conserved for a change of restframe,

$$N_\mathrm{e}\Delta t_\mathrm{e}\Delta E_\mathrm{e} = N_\mathrm{i}\Delta t_\mathrm{i}\Delta E_\mathrm{i} = \mathrm{const}, \tag{5.4.4}$$

then the emitted energy flux F_e as seen from an observer on the disk can be expressed as

$$F_\mathrm{e} = N_\mathrm{e}\cdot E_\mathrm{e} = (N_\mathrm{i}\cdot g^{-\Gamma})(E_\mathrm{i}\cdot g^{-1}) = F_\mathrm{i}\cdot g^{-(\Gamma+1)}. \tag{5.4.5}$$

with F_i denoting the incidence flux. Furthermore, the energy shift for every disk radius r can be expressed as a function of system parameters by calculating the photon energy as a product of the respective four-momentum and four-velocity of a stationary source (u_h) and a rotating disk (u_d) (Dauser et al., 2013):

$$g(r) = \frac{E_\mathrm{i}}{E_\mathrm{e}} = \frac{p_\mu u^\mu_\mathrm{d}}{p_\nu u^\nu_\mathrm{h}} = \frac{(r\sqrt{r}+a)\sqrt{h^2-2h+a^2}}{\sqrt{r}\sqrt{r^2-3r+2a\sqrt{r}}\sqrt{h^2+a^2}} \tag{5.4.6}$$

From this equation we can see that the incident photon flux depends on the radius at which the photon hits the disk, and the black hole spin. In order to calculate the energy shift from the source to an observer at spacial infinity, g_o, one can take the limit $r\to\infty$ and write

$$g_\mathrm{o} = \lim_{r\to\infty} g(r) = \frac{\sqrt{h^2-2h+a^2}}{\sqrt{h^2+a^2}}. \tag{5.4.7}$$

By setting the reflection fraction parameter to zero in a fit, the energy flux of the primary continuum can be measured by integrating the detected flux over a preferably large energy range, e.g., from 0.1 to 1000 keV. The new `RELXILL` model, however, directly fits the primary flux as a normalization parameter, hence it can simply be taken from the corresponding fit parameters. If additionally the mass of the acceting black hole is known, the length scales of the system expressed as a function of gravitational radius can be converted into a physical distance measure. The luminosity of an isotropically emitting source, which is independent of distance, is calculated as

$$L = 4\pi D^2 F_\mathrm{e}, \tag{5.4.8}$$

with D being the distance between source and observer. $\mathrm{F_e}$ is gained from Equation 5.4.5 using the distant energy shift g_o, where F_i can be identified with the incident flux at infinity, i.e. the observed flux that was extracted from the fit. The flux impinging on the inner edge of the disk can then be estimated as

$$F_\mathrm{in} = \frac{L}{4\pi R_\mathrm{d}}\cdot g_\mathrm{ISCO}^{\Gamma+1}, \tag{5.4.9}$$

where $R_\mathrm{d} = \sqrt{h^2+r^2_\mathrm{ISCO}}$ is the Cartesian distance between the source and the inner disk edge, and g_ISCO is the energy shift from Equation 5.4.6 with $r_\mathrm{i} = r_\mathrm{ISCO}$. The ISCO is set by the black hole spin since it is given in units of gravitational radii. Finally, the ionization at the inner edge is acquired by

$$\xi = \frac{4\pi F_\mathrm{in}}{n}. \tag{5.4.10}$$

with n being the electron density in the disk. In conclusion, the ionization can be estimated from the fit parameters primary flux, spin, source height, photon index and disk density, and the black hole mass and source distance. Note, however, that the other relativistic effects, like lightbending and length contraction, are not included in this estimate. Also, the distance R_d should be calculated in Boyer-Lindquist coordinates for a proper treatment of Kerr space-time

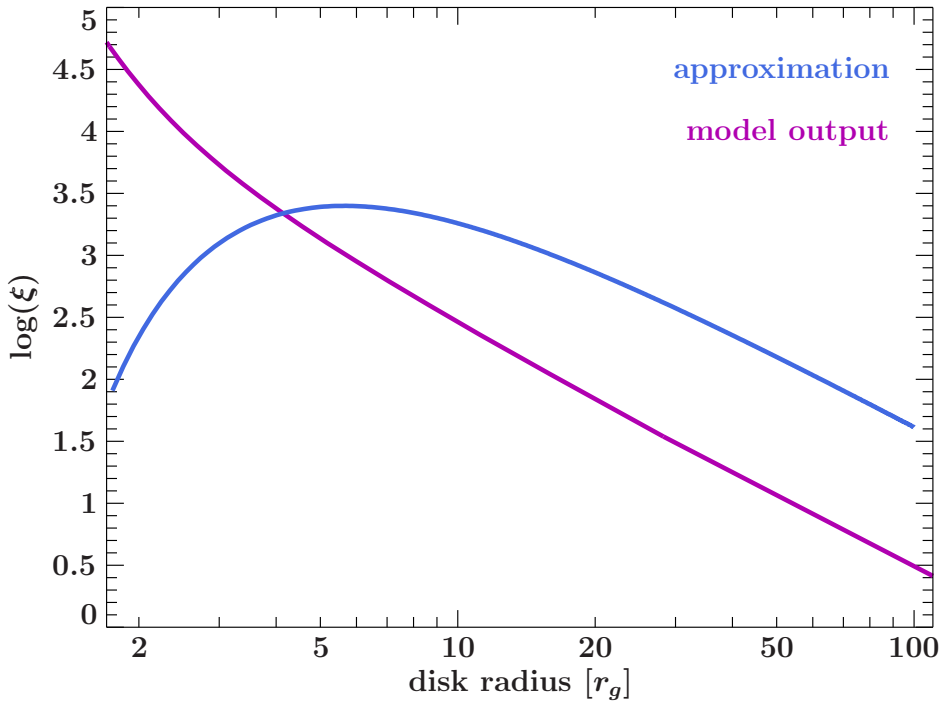

Figure 5.4: Logarithmic disk ionisation $\log(\xi)$ as a function of radius, as predicted by the Alpha model without density gradient (magenta) and approximated (blue).

(see chapter 2). The estimated ionization will therefore necessarily deviate from the value derived by the new relxill model.

The estimated ionisation per radius for an AGN that will be analyzed in my thesis[1] via Equation 5.4.10 is compared to the new model output, assuming a constant density, with the same parameter combination in Figure 5.4. It is evident that, while mostly deviating from the proper ionisation curve by a factor of less than 2, my equations will underestimate the ionisation for small radii ($r < 5\,r_\mathrm{g}$) and overestimate it for larger radii ($r > 5\,r_\mathrm{g}$). In order to get a valid estimate for the ionisation at the inner edge ($\sim 1.25\,r_\mathrm{g}$ for a maximally spinning black hole), one has to multiply the value by a factor of around 2.25. I therefore caution that this is only meant as an order of magnitude estimate.

5.4.2 Parameters of the improved model

In Figure 5.5, the output spectra of the Alpha model for different parameter combinations are plotted in order to showcase the impact of the parameters on the spectral shape. The parameter names, a short description, and the range usually found in AGN are furthermore given in Table 5.1. As the new model internally calculates the primary flux in cgs-units, the normalization can be given in physical units as the integrated energy flux of the primary source.

The **upper left panel** of Figure 5.5 shows spectra for different inclination values, ranging from almost head-on ($i = 20°$) to almost edge-on ($i = 70°$). Generally for higher inclinations, the amount of absorption decreases while the spectrum approaches the original cutoff-powerlaw shape, because, as was already argued in the previous sections, high energy photons get scattered more often than low energy photons, so their fraction in the total flux is higher for

[1] parameters: mass $\log(M_\mathrm{BH}/M_\odot) = 7.3$, distance $D = 80.50\,\mathrm{Mpc}$, spin $a = 0.998$, photon index $\Gamma = 1.62$, source height $h = 1.5\,r_+$, density $\log(N) = 15$ and flux $F = 4.5 \times 10^{-12}\,\mathrm{keV\,cm^{-2}\,s^{-1}}$

Table 5.1: Parameters of relxilllpAlpha.

Param	Unit	Description	Range
norm	$\frac{\text{erg}}{\text{cm}^2\,\text{s}}$	flux in the 0.1 to 1000 keV range of the primary source	$10^{-18} - 10^{-5}$
a	-	spin of the black hole	$0 - 0.998^*$
i	deg	inclination of the disk w.r.t. viewer's plane	$5 - 80$
R_{in}	r_{ISCO}	inner disk edge	$1 - 100$
R_{out}	r_{g}	outer disk edge	$r_{\text{in}} - 1000$
h	r_+	on-axis height of the primary source	$1.5 - 100$
β	c	upwards velocity of the primary source	$0 - 0.9$
Γ	-	photon index of the primary continuum	$1.2 - 3.4$
$\log(N)$	$\log(\text{cm}^{-3})$	logarithmic electron density of the disk	$15 - 20$
A_{Fe}	solar	iron abundance in the disk	$0.5 - 10$
kT_e	keV	electron temperature of the corona	$1 - 400$
R_{frac}	-	fraction of reflected radiation	$0 - 10$
switch_relfrac_boost	-	treat R_{frac} as boost parameter	0/1

high inclinations. Changes in the line profiles are also seen: as the inclination and therefore the projected optical depth increases, different elements in the disk become visible which each emit different low energy lines. It is also notable that the whole spectrum shifts towards higher energies: since for higher inclinations the projected component of the angular disk velocity is more affected by Doppler boosting, the spectrum is blueshifted, smoothed, and the blue wing of the iron line extends.

Spectra for different X-ray source heights are shown in the **second upper left panel**, ranging from 8 to 1.1 event horizons above the disk plane. The closer the corona approaches the black hole, the smaller the features and peaks in the spectrum become, the less continuum absorption can be seen, and the more the spectrum approaches a cutoff-powerlaw. Since for a low height, the irradiation is focused strongly onto the very inner part of the disk, which in turn is also highly ionized, electron scattering almost completely dominates for this case and produces a mirror-like image of the primary continuum as reflection. Also, the cutoff energy shifts downwards for lower heights since the photons travelling from the source to the disk experience a smaller gravitational energy shift. Therefore the disk receives a lower cutoff energy.

In the **second lower left panel**, spectra for different values of the boost parameter can be seen. A boost of 0.5 means half of the predicted amount of reflection is used, and a boost of 5 means five times as much reflection is used than predicted. For a higher boost, the spectrum generally tends to have larger and more defined line features, because those only arise when photons are absorbed and reemitted in the disk.

Spectra for different values of the photon index are depicted in the **lower left panel** panel. They range from soft ($\Gamma = 2.0$) to hard ($\Gamma = 1.5$). Generally, the photon index determines the steepness of the primary spectrum and therefore also the steepness of the reflected spectrum, given that the reflection processes do not alter the spectral shape too much. A very hard spectrum will exhibit a pronounced Compton hump and minor absorption and line features, since electron scattering is the dominant radiative interaction process for high energies. The Compton hump becomes smaller, and the lines become more pronounced for a softer primary spectrum. At some point, enough low energy photons are present so that absorption becomes dominant again, and the flux in the iron line region no longer increases.

The **upper right panel** shows spectra for different iron abundances in the disk, ranging from twice to ten times the solar value. For higher iron abundances, more and more of the flux gets redistributed into the iron line, which in turn becomes very prominent compared to the other features.

Different values of the logarithmic electron density, from 15 to 20, are shown in the **second upper right panel**. As the density, and therefore the number of electrons available for absorption, increases, more and more of the flux from the 1–10 keV regime is absorbed and reemitted as low energy lines. For higher densities, the flux in the high energy band (>10 keV) increases again as the disk becomes too dense for the high energy photons to enter into deeper layers. Therefore they undergo more scattering in the hot and highly ionized surface layer, which boosts the Compton hump and weakens the iron line in the spectral shape.

The **second lower right panel** shows reflection spectra for different coronal velocities, from a stationary corona ($\beta = 0\,\mathrm{c}$) to a corona moving away from the disk at almost light speed ($\beta = 0.8\,\mathrm{c}$). As the source becomes faster, the radiation is Doppler-boosted away from the disk and the flux decreases. Because of relativistic beaming, the emission of the corona viewed from the restframe of the disk is focused in the direction of movement, but lightbending still focuses the radiation onto the inner disk part. As a result, the outer regions are irradiated less. For velocities close to lightspeed, the distant observer only sees the continuum flux, since all radiation is boosted away from the disc.

In the **lower right panel**, spectra for spin values ranging from non-rotating ($a = 0$) to maximally rotating ($a = 0.998$) are shown. As the spin mainly controls the location of the inner edge (see Equation 4.1.3), the strength of relativistic broadening is influenced by this parameter. For low spin, the disk appears truncated, and the reflected photons do not come close enough to the black hole in order to be strongly influenced by lightbending; therefore the iron line is sharp. Furthermore, since the disk does not extend into the region onto which a large part of the flux is focused for low and intermediate source heights, the surface is only weakly ionized, and much of the flux below 10 keV is absorbed. For high spin, the disk extends far into the highly relativistic regime close to the black hole, and the iron line appears broadened with a red wing extending to low energies.

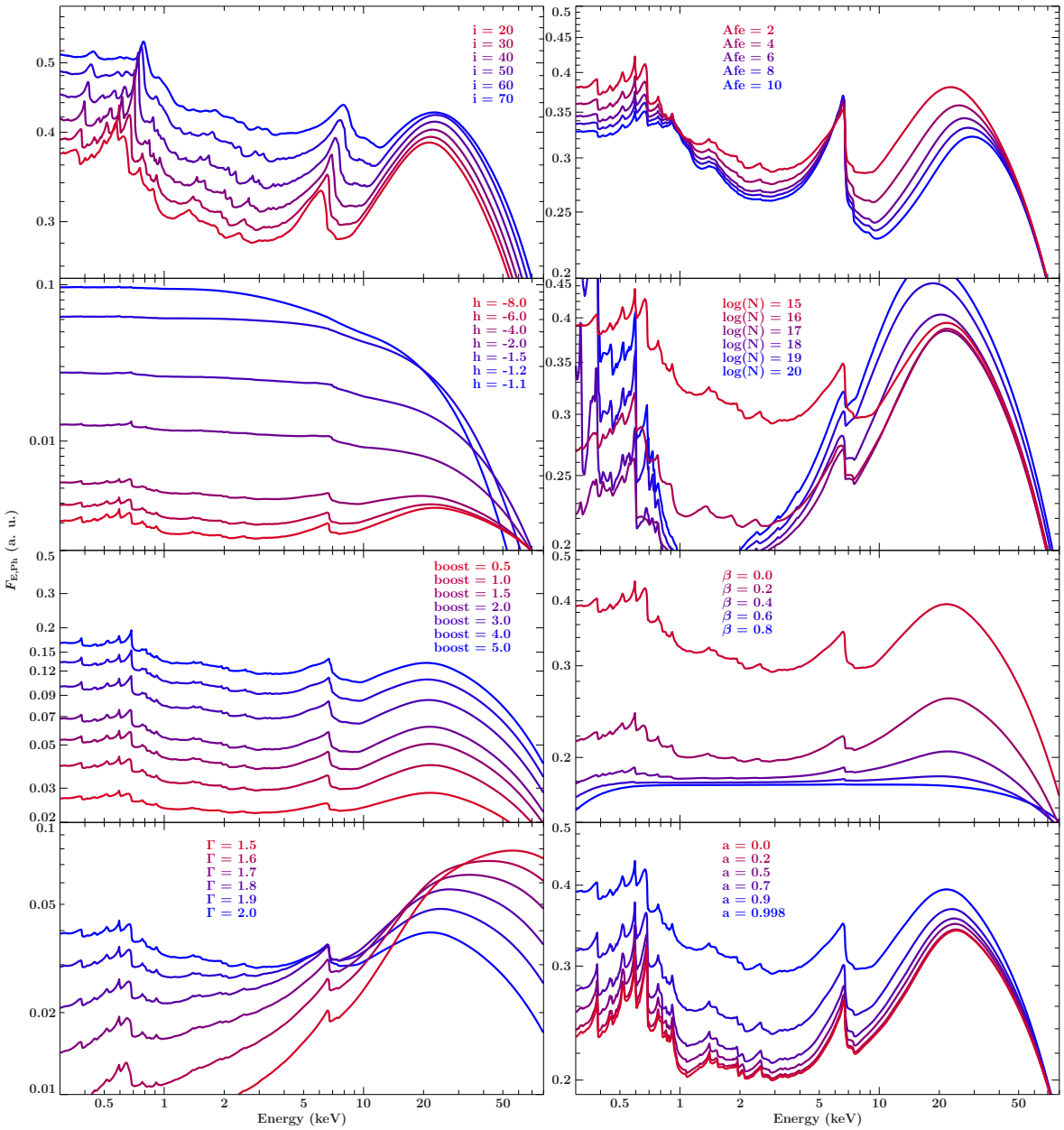

Figure 5.5: Reflection spectra calculated by the relxilllpAlpha model for different parameter combinations. Other than the parameters specified in the panels, a standard model with $i = 30°$, $h = 6\,r_+$, *boost* $= 1$, $A_{\mathrm{Fe}} = 1$, $\log(N) = 15$, $\beta = 0$, $a = 0.998$, $\Gamma = 2$ and $kT_{\mathrm{e}} = 60\,\mathrm{keV}$ is used.

6 Instruments

In order to magnify the region of the sky that one wants to observe, the light is focused in a telescope by specially shaped mirrors. In X-ray astronomy, however, this is not so straightforward, since only X-rays at near-grazing angles achieve significant reflection on a mirror (Wolter, 1952). Otherwise, the photons get absorbed. For successful X-ray reflection, the German physicist Hans Wolter developed a grazing incidence telescope which was originally intended for usage in microscopes, but is today widely used for extraterrestrial X-ray detection. The Wolter-I prototype consists of two separate mirror modules, one parabolic, the other hyperbolic, on which the incident X-rays get reflected twice. A qualitative illustration of this principle can be found in Figure 6.1. To maximise the light collection area, a number of consecutive mirror shells are nested together to fill out the interior of the telescope.

Ground telescopes cannot be used for detecting X-rays, since those wavelengths are blocked by the earth's atmosphere. Instead, satellites that carry the X-ray optics with them are launched into space. For example, the spacecraft of the XMM-Newton mission carries energy detectors with a spectral range of 0.5 to 15 keV. In modern optical instruments, the energy of photons is usually detected by Charge-Coupled Devices (CCDs) which are based on the inner photoelectric effect.

As was shown in chapter 4, hot electron plasma can upscatter radiation to many tens of keV. In order to cover the full X-ray range that is relevant for AGN spectra, data from multiple instruments with differing energy ranges is needed. In my thesis, I do not only use data from the aforementioned XMM-Newton, but also from NuSTAR.

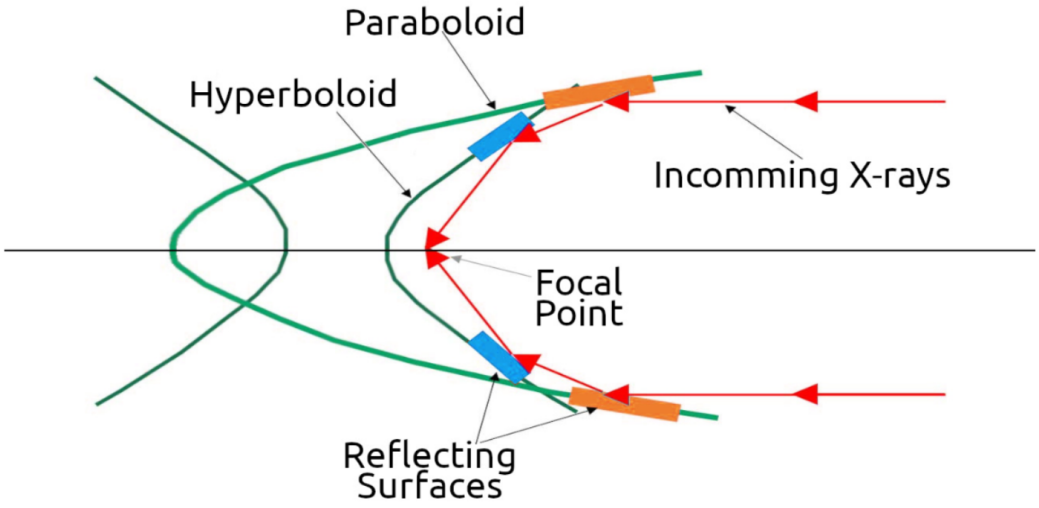

Figure 6.1: Illustration of a cross section through the Wolter-I telescope prototype. The incoming x-rays first get reflected on the parabolic mirror shells, and then again on the hyperbolic mirror shells, before they reach the focal point (taken from Abbasian Motlagh & Rastegarzadeh, 2020).

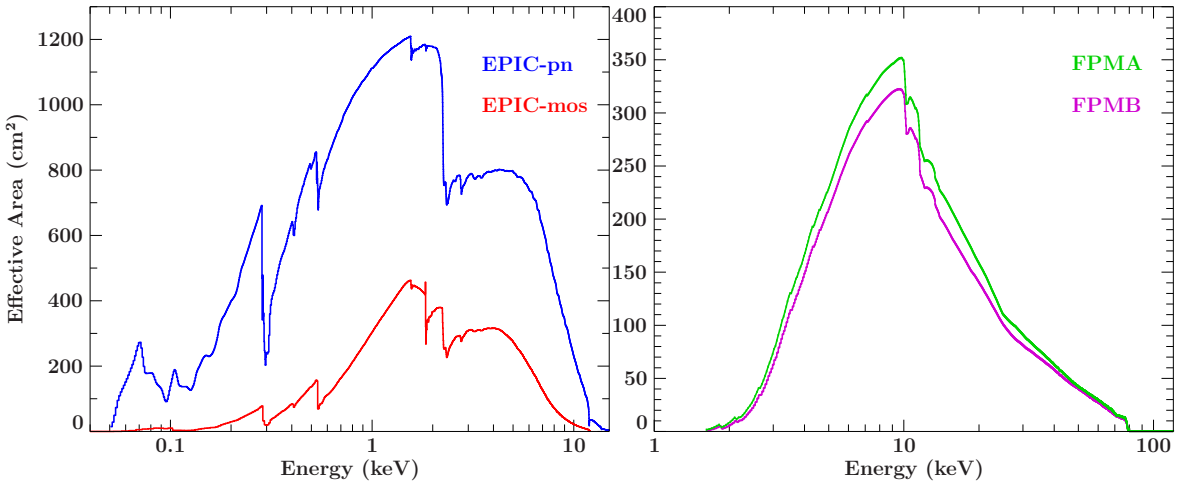

Figure 6.2: *Left:* Effective area of the EPIC-pn and EPIC-mos detectors of XMM-Newton as a function of photon energy. *Right:* Effective area of the FPMA and FPMB module detectors of nuSTAR as a function of photon energy.

6.1 XMM-Newton

The XMM-Newton spacecraft (Jansen et al., 2001), in which XMM stands for X-ray Multi Mirror, weighing 4 tons and measuring 10 meters in length, is the largest scientific satellite that was ever launched by the European Space Agency (ESA). An illustration of the spacecraft can be found in Figure 6.3. The mission, which started on December 10th in 1999, brought three high throughput telescopes into space. The modular configuration of the spacecraft consists of four elements: the Focal Plane Assembly (FPA) carries the Reflection Grating Spectrometer (RGS, den Herder et al., 2001) unit and the European Photon Imaging Cameras (EPICs, Strüder et al., 2001); the Mirror Support Platform (MSP) carries the three mirror assemblies and the optical monitor (Mason et al., 2001); the Service Module (SVM) contains technical subsystems, two solar-array wings, the sun-shield and the antennas for communication. In the focal plane, the optics are split into two units. One consists of two EPIC-MOS (Metal Oxide Semi-Conductor) CCD arrays, for which the gratings of the RGS divert half of the incoming flux towards the RGS detectors; the other half reaches the MOS cameras. The other optical unit consists of one EPIC-pn CCD camera array. Here, the telescope does not obstruct the infalling X-ray beam. This whole setup achieves sensitive X-ray imaging in an energy range from 0.5 to 15 keV with a moderate spectral resolution of $E/\Delta E \sim 20$–50. The effective area of both detectors is plotted in the left panel of Figure 6.2. From this, it is evident that the highest detection efficiency is achieved in the 1–2 keV range.

6.2 NuSTAR

The satellite of the NuSTAR mission (Harrison et al., 2013), short for Nuclear Spectroscopic Telescope Array, brought forth by the National Aeronautics and Space Administration (NASA) launched on June 13th in 2012. An illustration can be found in Figure 6.4. On the 350 kg spacecraft, two co-aligned grazing incidence telescopes of the Wolter-I-type are installed. Because the shallow reflection angles require a long focal length, the focusing module and the detection module are connected by a 10 m long mast which extended to its full length only after the final position in orbit was reached. At the focal point of each optical unit, a Focal Plane Module (FPM) detection unit is installed, hereafter referred to as FPMA and

FPMB. One detector unit consists of 4 Cadmium-Zinc-Telluride (CZT) detectors. Other than XMM-Newton, the NuSTAR mission focuses on detecting the harder X-rays. It operates in the range of 3 to 79 keV with a spectral resolution of a FWHM response of 400 eV at 10 keV and 900 eV at 68 keV. Since the usual high-density mirror coatings, e.g. iridium or gold, only enhance the reflexivity in the low energy X-ray regime, NuSTAR employs depth graded multilayer coatings (Christensen et al., 2011) with typically 200 alternating layers and high density contrast between the layers in order to achieve high reflexivity for high energy X-rays. With this, the detection efficiency peaks at 10 keV, as is shown in the right panel of Figure 6.2.

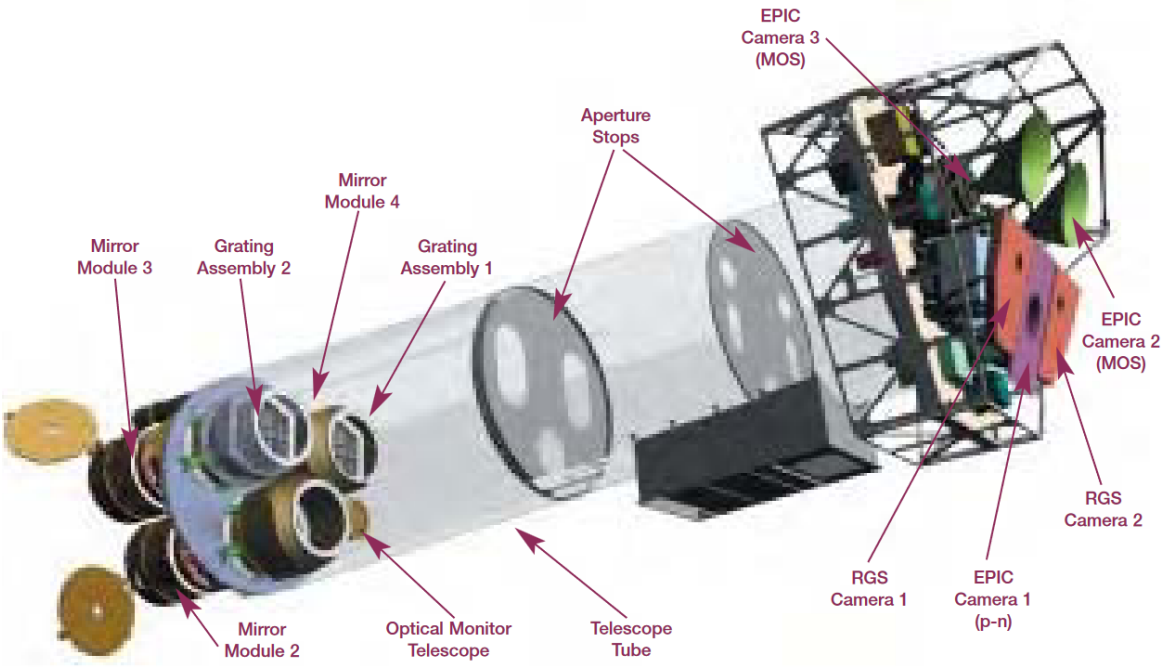

Figure 6.3: Diagram of the XMM-Newton Satellite, showing the principal elements (taken from Wilson, 2005).

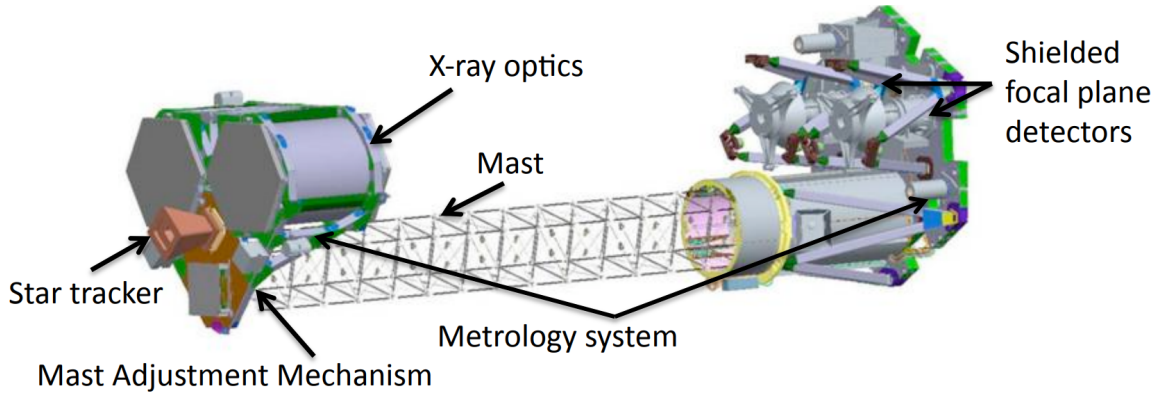

Figure 6.4: Diagram of the NuSTAR satellite, showing the principal elements (taken from Harrison et al., 2010).

7 Data Analysis Tools

The sources that are studied in X-ray astronomy are often located thousands of parsec away from earth. It is therefore necessary to understand all processes which may influence the X-ray radiation along their way. In the previous chapter, intricate physical models for the AGN source spectrum and galactic absorption were introduced. In order to approximate this original spectrum from the observed spectrum, also models for the detector response are needed. Furthermore, the final results can only be significant if the technical process of data analysis is thoroughly understood. This chapter sets out to cover these topics.

7.1 Instrument response

After travelling from its physical source to our location of observation, the X-ray photons enter the telescope, are focused by an array of mirrors and are measured by a detection unit. Since the mirrors do not reflect all incident energies equally well, an energy dependent effective area $A(E)$ can be defined, by which the observed counts are scaled. Furthermore, the energy detection is only possible within an energy grid that is defined by the discretization of electronic detector signal into digital units by the Analog-to-Digital Converter (ADC); inside a bin, the energy is assumed to be constant. Photons may trigger signals in channels with the wrong energy due to e.g. impurities in the detector material. The probability of the incident energy E creating an event with energy E' is given by the response function $R(E, E')$. The photon spectrum of the source as a function of continuous energy $f(E)$, given in units of e.g. photons $\mathrm{m}^{-2}\,\mathrm{s}^{-1}\,\mathrm{keV}^{-1}$ is then converted into the observed count spectrum $S(E')$ by convolving the photon spectrum with the effective area and detector response:

$$S(E') = \int_0^\infty R(E, E')\, A(E)\, f(E)\, dE \tag{7.1.1}$$

Due to the complexity of the spectrum and the response, it is in most cases impossible to carry out the integration analytically. Instead, it has to be evaluated for a limited number of energies; the same that are given by the detector response. The integral thereby becomes a sum, following

$$S(E') = \sum_{i=0}^{N} R(E_i, E_i')\, A(E_i)\, f(E_i)\, \Delta E, \tag{7.1.2}$$

with N denoting the total number of bins, and ΔE the bin width. This approximation is only accurate if the energy bin width is small compared to the spectral resolution of the detector. The information about effective area and detector responses is given in discrete matrix format as the *Ancillary Response File* (ARF) and the *Redistribution Matrix File* (RMF), respectively.

Lastly, the desired X-ray flux from the source is not the only signal that is measured. A certain level of background flux $B(E')$ is added on top of the source flux due to artifacts in the CCD cameras, cosmic ray particles passing through the detector, or the X-ray emission from a large number of point sources that are not resolvable as individual sources, known as the cosmic X-ray background (Revnivtsev et al., 2006). By measuring the flux of a sourceless area in the vicinity of the source in question, the so obtained background flux can be subtracted from the total measured flux, yielding an approximation of the pure source spectrum.

7.2 Model fitting

For quantifying how well a certain model fits a data set, a statistical test is a useful tool. First, a test statistic S needs to be chosen; then, it is evaluated on the data and model, and compared to the theoretical distribution of S if the hypothesis - that the data was produced by a particular model - were true. If S exceeds a certain value, the hypothesis can be rejected with statistical significance. A significance level α is chosen accordingly, where

$$\alpha = \int f(S)\, dS, \tag{7.2.1}$$

with the probability density function $f(S)$ of S. The integral is calculated over the critical region, so that α denotes the probability of S falling in the critical region or, in other words, the probability of wrongly rejecting the hypothesis.

The error on the counts in one energy bin is Poisson distributed, i.e. the error values are calculated as $\sqrt{N}$, but the distribution can be approximated by a Gaussian whose variance equals the mean if the number of counts is large (Lampton et al., 1976). For this reason, the χ^2-statistic is the most widely used test. The next subsection will largely follow the paper of Lampton et al. (1976) for the purpose of introducing χ^2-minimization.

7.2.1 The χ^2-statistic

Originally conceptualized by Pearson (1900), the χ^2-statistic for N measurements is defined as

$$S =: \sum_{i=1}^{N} \frac{(D_\mathrm{i} - F_\mathrm{i})^2}{\sigma_\mathrm{i}^2}, \tag{7.2.2}$$

where D_i are the data points, F_i are the model predictions and σ_i are the expected variances. If the tested hypothesis is true, S is χ^2-distributed with N degrees of freedom (DOF), given that the deviations are independently Gaussian distributed. If the hypothesis is wrong instead, systematic errors will increase S significantly on average. It is straightforward to test a simple hypothesis on such a statistic; however, in practice often composite hypotheses need to be tested. For example, only one model may be tested on the data, but it is unclear which values of a number of model parameters best describe the data. In this case, the miminum S_min of the statistic is searched by varying a number p of adjustable parameters. S_min will then be χ^2 distributed with $N - p$ DOF ($S \sim \chi^2_{N-p}$). Instead of explicitly testing the significance of a fit, often the reduced statistic, defined as $\chi^2_\mathrm{red} = S_\mathrm{min}\,(N-p)^{-1}$, is consulted. The fit is deemed good if this value is close to one.

Of course, only estimating the best-fitting point in the parameter space is useless if there are no quantitative measures for the accuracy of the estimate. The earliest methods of supplying errors on the parameters required holding all parameters but one fixed, and then calculating the range of the parameter for which $\Delta S = 1$. If this procedure is done for all relevant parameters, a confidence region can be drawn in the parameter space, given a chosen confidence level C. By definition, $C = 1 - \alpha$. For example, a confidence level of 90 % means that the confidence region contains the true value of the parameter 90 % of the time if the experiment is repeated often. Like this, an infinite number of possible confidence regions could be constructed for the parameters, yielding a confidence interval $x - \sigma < X < x + \sigma$ for every parameter X. In X-ray astronomy, however, parameters are often heavily correlated, i.e. a change in one parameter is compensated by readjustments in others. For such systems, a simple error estimate would underpredict the real errors.

It can be shown that the variable $\Delta S =: S_{\text{true}} - S_{\text{min}}$ is χ^2 distributed with p DOF, which implies that ΔS is independent of the distribution of S_{min}. When constructing a region in parameter space for which $S - S_{\text{min}} < T$ (with a chosen limit T), the confidence under which the region contains the true parameter vector can simply be calculated as

$$C = \int_0^T f(\chi^2)\, d\chi^2, \tag{7.2.3}$$

for which $f(\chi^2)$ is the probability density of χ^2_p, since $\Delta S \sim \chi^2_p$. Here, the shape of the confidence region is not arbitrary, but determined by the fixed ΔS distribution. This method provides exact confidence regions even when the parameters are not independent. Further calculations show that the contour value S_C is given by

$$S_C = S_{\text{min}} + \chi^2_p(\alpha). \tag{7.2.4}$$

With e.g. $p = 3$ and $C = 90\,\%$, the contour amounts to $S_C = S_{\text{min}} + 6.25$. These estimates, however, are only significant if systematic errors play a negligible role, i.e. when the fit is good in the first place. Otherwise, the assumption that $S_{\text{min}} \sim \chi^2_{N-p}$ cannot be made.

7.2.2 Model components

The data analysis in this thesis was done with the Interactive Spectral Interpretation System (ISIS) that was developed at MIT (Houck & Denicola, 2000) specifically for the interpretation and analysis of high resolution x-ray spectra. It supports measurements and identification of spectral features and allows interaction with large atomic data bases and plasma emission models. As an operating language, it employs S-Lang, which specifically supports array based operations and is therefore ideal for numerical applications. The spectral models implemented in ISIS are derived from XSPEC, an X-ray spectral fitting package developed by the High Energy Astrophysics Science Archive Research Center (HEASARC) of NASA. The relevant models are described as follows:

- **tbabs:** a galactic absorption model which calculates the cross section for X-ray absorption by the ISM as the sum of the cross sections for X-ray absorption due to the gas-phase ISM, the grain-phase ISM, and the molecules in the ISM. Developed by Wilms et al. (2000).
- **tbnew$_{\text{feo}}$:** a simplified galactic absorption model with only the absorption column and the columns for O and Fe, and the redshift as free parameters. Developed by Wilms et al. (2000) as a flavor of tbnew, an improved version of tbabs.
- **mekal:** an emission spectrum from hot diffuse gas based on the model calculations of Kaastra & Mewe (1993) with Fe L-shell calculations by Liedahl et al. (1995), including line emission from several elements.
- **apec:** an emission spectrum from collisionally ionized diffuse gas, calculated from the AtomDB atomic database (`http://atomdb.org`).
- **nthComp:** an empirical thermal comptonized continuum model that outputs a powerlaw-like spectrum with high energy cutoff. The cutoff is sharper than a pure exponential cutoff, but describes actual Comptonized spectra better. Developed by Zdziarski et al. (1996), extended by Życki et al. (1999).
- **partcov:** a convolutional model that converts an absorption model M into partially covering absorption with covering fraction C_{f}, following $M(E) \to (1 - C_{\text{f}}) + C_{\text{f}} \cdot M(E)$.

- **xillver:** a table model that provides a complete library of spectra for modeling emission that is reflected from illuminated accretion disks. It especially provides an accurate description of the Fe K emission line, but only works well if the thermal disk flux is faint compared to the incident powerlaw flux. It was developed by García et al. (2013).
- **xstar:** a grid of models precalculated by the program XSTAR for calculating the physical conditions and emission spectra of photoionized gases (Bautista & Kallman, 2001).
- **relxilllp:** a relativistic reflection model that intrinsically connects reflected emission and relativistic blurring in the Kerr metric, as described in the previous chapter, and employs a lamppost corona geometry. The primary emission is modeled by nthComp. Developed by Dauser et al. (2013), García et al. (2014).

7.3 Optimal data binning

For spectral analysis, the raw data is often rebinned to achieve a certain signal-to-noise ratio (SNR). In doing so, one needs to consider that a too large bin size may result in information loss, whereas for a too small bin size, statistical tests like χ^2 minimization may become insufficiently sensitive to structures in the data, or large computational costs can occur when evaluating models.

In order to find the optimal bin size, the theorem of Shannon (1949) can be used, as was done by Kaastra & Bleeker (2016). The fourier transform of a spectral function $f(x)$ is defined as

$$g(\omega) = \int_{-\infty}^{\infty} f(x)\, \exp(i\omega x)\, dx. \tag{7.3.1}$$

If now $g(\omega) = 0$ for all $|\omega| > W$ with a limit frequency W, i.e. $f(x)$ is band-limited, then $f(x)$ can be expressed as

$$f(x) = f_{\mathrm{s}}(x) = \sum_{n=-\infty}^{\infty} f(n\Delta) \frac{\sin \pi(x/\Delta - n)}{\pi(x/\Delta - n)}, \tag{7.3.2}$$

where $\Delta = 1/2W$ denotes the bin size. This means that a band limited signal is completely determined by a grid with constant spacing Δ, which gives the optimal bin size. Moreover, the cumulative density function

$$F(x) = \int_{-\infty}^{x} f(y)\, dy \tag{7.3.3}$$

can be shown to be determined completely by discrete x-values $m\Delta$ for integer numbers of m as well, if $f(x)$ is band-limited. For a real X-ray spectrum that may not be band-limited, $F_{\mathrm{s}}(x)$ can be used to approximate the true cumulative distribution at the energy grid, and the error can be estimated by comparing F_{s} and the true function F. The optimal bin size is calculated so as to keep the error sufficiently small.

8 Investigating the effects of a self-consistently calculated ionisation

In the lamppost geometry (see section 5.3), a point-like source located at some height above the accretion disk around a black hole irradiates and, subsequently, ionizes the inner parts of the disk. The emerging reflection spectrum is strongly influenced by the degree of ionisation (see chapter 4). In previous analyses, e.g. of the Seyfert-II galaxy ESO 033-G002 (Walton et al., 2021, hereafter W21), the ionisation of the disk was a free fitting parameter. However, with the knowledge of the black hole mass and the distance between source and observer, the luminosity of the primary irradiating source can be measured in physical units. Together with the electron density of the disk, the ionisation can subsequently be calculated self-consistently from other model parameters, as was qualitatively shown in section 5.2. With the additional modeling of a radial density gradient across the disk, the ionisation can be calculated for each radius interval, thereby adding up to a radial ionisation gradient (see section 5.4).

In this chapter, a new relativistic reflection model, which implements a self-consistently calculated ionisation, is tested on the spectral X-ray data set of ESO 033-G002. The new model applies a more strictly physical approach to reflection modeling than the previous, more empirical model. In the first place, it will be tested if the new model, which calculates the primary flux and the ionisation directly from the fitted source height, can describe the data. Secondly, as the impact of an intrinsic ionisation to the model fitting process has not been studied before, the performances and results of the new model are compared to those of currently available model versions, which include the ionisation as a free parameter.

More specifically, the impact of different models of density and ionisation profiles of the accretion disk on the best fitting parameters is examined, especially in relation to the disk ionization. A simple density gradient for a disk for which the thin disk approximation holds is the α-disk gradient (Shakura & Sunyaev, 1973), which was introduced in chapter 4. First, I want to test the free ionisation model on different assumptions for density and ionisation gradient: a radially constant density and ionisation, a constant density but an empirical powerlaw ionisation gradient, and the more physically motivated α-density and ionisation gradient. Then, the new and more self-consistent model is also tested for a radially constant density gradient, and the physically motivated gradient. Testing the model with a self-consistent ionisation stage and physically motivated α-density and ionisation gradient, which, compared to the other model versions, takes the highest number of physical assumptions into account, is the main goal of this thesis. For each stage, the results are compared and discussed, especially in the light of the role the ionisation plays internally in the models.

8.1 Seyfert-II-galaxy ESO 033-G002

The nearby ($z = 0.0181$) radio-quiet and X-ray bright type-II-Seyfert galaxy ESO 033-G002, as analysed by W21, shows signs of an extremely compact accretion geometry in which the strong lightbending suppresses the direct coronal emission and enables an unusually high reflection fraction. W21 found that the spectrum hints at reflection from both the accretion disk and more distant material: a relativistically broadened iron line and a reflection hump,

as well as a narrow iron emission line reprocessed in a distant regime which is not influenced by relativistic effects. The presence of an ionized outflow is apparent in blueshifted absorption lines from Fe XXV and Fe XXVI. Even though the soft part of the X-ray spectrum ($< 1.5\,\mathrm{keV}$) is obscured, the innermost accretion flow can still be examined in the harder X-rays. A long coordinated observation of ESO 033-G002 with *XMM-Newton* and *NuSTAR* (109/125 ks for EPIC-pn and EPIC-mos, respectively, and 172 ks for NuSTAR) was undertaken in 2020, starting on the 6th of June. This data was used by W21 for a spectral analysis. Due to the extreme reflection geometry found by W21, the equally good fit for a consistent lamppost geometry and the amount of available data, ESO 033-G002 is a great candidate for testing the new version of relxilllp with a self-consistently calculated ionisation.

In order to prove on my own that relativistic reflection is really necessary for describing the data well, I fitted a simple cutoff powerlaw to the data and compared it to the relxilllpCp fit with a constant ionisation that will be introduced later on. The model components and the residuals are shown in Figure 8.1. In the residuals for the powerlaw fit, reflection features can be clearly seen. The excess in flux at $\sim 6.5\,\mathrm{keV}$ has the shape of an iron Kα line, and the excess above $\sim 15\,\mathrm{keV}$ hints at the Compton hump. Small depletion features around 7 kev also indicate the ionized absorption lines from an outflowing component. Especially the large iron line seems to make ESO 033-G002 a good candidate for testing out the impact of a self-consistently calculated ionisation, since especially the shape of this feature strongly depends on the ionisation stage. However, I again want to stress that W21 found the iron abundance being mostly influenced by the distant reflection, while the abundance of the highly relativistic regime was not well constrained. It is therefore expected that the differences caused by the ionisation of the (inner) accretion disk result only in minor differences in the total spectrum.

8.1.1 X-ray modeling

The full spectral model that was applied by W21 and is also reused in this thesis is $\texttt{TBABS}_{\mathrm{gal}} \times (\texttt{MEKAL} + \texttt{NTHCOMP} + \texttt{XILLVER} + (\texttt{TBABS}_{\mathrm{full}} \times \texttt{TBABS}_{\mathrm{part}} \times \texttt{XSTAR} \times \texttt{RELXILL}))$. The individual models were introduced in chapter 7. In order to account for calibration differences in the instruments and the different observation durations, cross calibration constants are added to each data set, employing the EPIC-pn data as reference. Furthermore, W21 cut the data sets to the energy range of 0.3–10 keV for XMM-Newton, and to 4–78 keV for nuSTAR, since above and belong these ranges, the effective area of the detectors is too small or exhibits large jumps (see Figure 6.2). I used the same energy ranges for my data analysis.

Following W21, the highly relativistic, ionized reflection from the inner accretion disk, as well as the part of the primary continuum which reaches the observer directly, is modeled by `RELXILL`, using a lamppost geometry. The reflection off of distant and neutral material, which is unaffected by the effects of Kerr space-time metric around the black hole, is modeled by `XILLVER`. `MEKAL` and `NTHCOMP` allow for soft X-ray emission (scattered nuclear flux, diffuse plasma emission) disconnected from the central system. Additionally, `TBABS` allows the inner reflection to be absorbed by partially or fully covering cold and neutral material; `XSTAR`, which consists of a grid of precalculated models, provides absorption by an outflowing and ionized component. For this, an ionizing continuum with a photon index of $\Gamma = 2$ and a velocity line broadening of $3000\,\mathrm{km\,s^{-1}}$ was assumed, because those values are typical for AGN systems (Ricci et al., 2017; Risaliti et al., 2005). The whole resulting spectrum is also subject to absorption from the galactic column by `TBABS` with a density of $N_{\mathrm{H}} = 8.95 \times 10^{20}\,\mathrm{cm^{-2}}$ (HI4PI Collaboration, 2016).

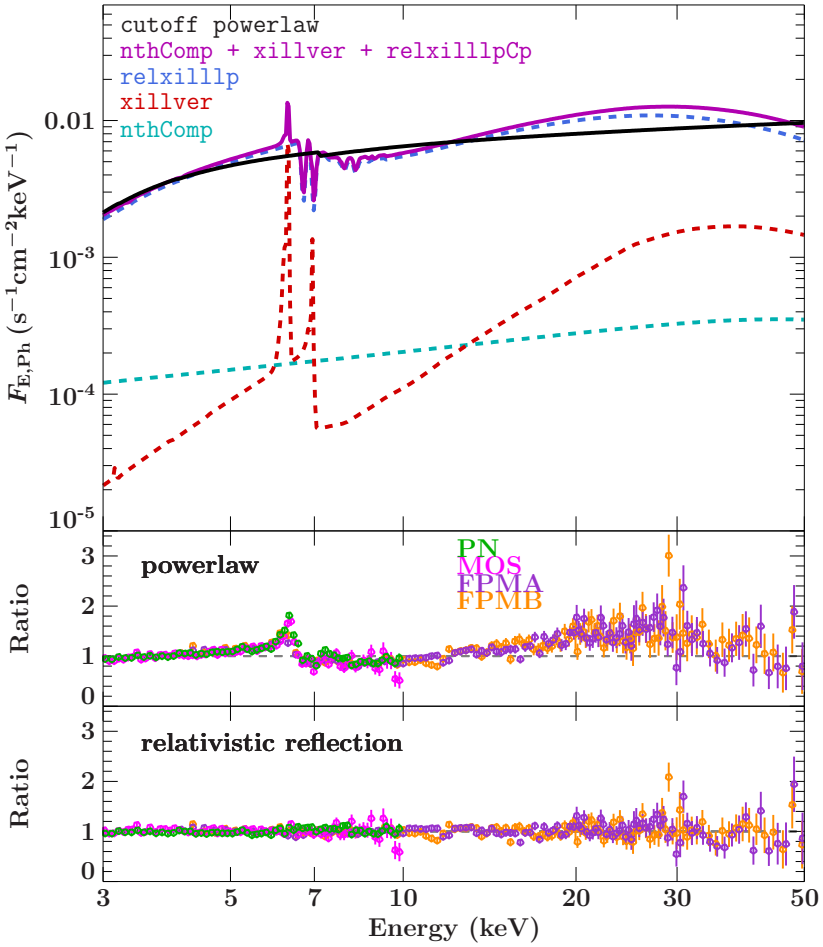

Figure 8.1: Best fit model components and residuals for a simple spectral cutoff powerlaw fit (black), and a complex relativistic reflection fit with absorption and distant neutral emission features (magenta).

General results

W21 found the best-fitting reflection fraction to be in the range of $\mathrm{R_{frac}} = 3$–7. By also fitting a broken powerlaw emissivity instead of a formal lamppost profile, W21 found an inner emissivity index of $q_{\mathrm{in}} > 5.3$ and a break radius of $R_{\mathrm{br}} = 2.5$–$3.6\,r_{\mathrm{g}}$, which implies a steep emissivity profile with the inner part of the disk being strongly irradiated, while the outer disk parts are illuminated weakly. This is well predicted by a compact lamppost geometry. Also, it is exactly the reason why the choice of model for the distant reflection does not matter in the fit (`BORUS` was tested instead of `XILLVER`, but the change in χ^2 was negligible): since the distant emission makes up only a small faction of the total flux, a different choice of model will have an equally small impact in the fit statistic.

Furthermore, W21 fitted a version of `RELXILL` where the reflection fraction is calculated self-consistently from a and h. They found that, while the predicted fraction of $\mathrm{R_{frac}} \approx 5.4$ matched their previous results, some fit parameter constraints tightened. The spin tended to the maximal value in all cases and was constrained rather tightly from below with $a > 0.96$. W21 also found that the iron abundance did not depend on the disk density, since it is likely mostly influenced by the distant reflector. Allowing a free iron abundance for `XILLVER` showed that a solar abundance for the distant material is strongly disfavoured, and the abundance of the accretion disk is badly constrained. This indicates that ESO 033-G002 really has a

supersolar iron abundance.

W21 suggest that that the partially covering absorber might be transient, similar to observations of e.g. NGC 5548 (Kaastra et al., 2014), and could consist of a far extending stream of material that originally launched from the accretion disk. The ionized absorption is clearly blueshifted w.r.t. the cosmological redshift of ES0 033-G002, resulting in a high outflow velocity of $\sim 5400\mathrm{km\,s^{-1}}$. From escape velocity arguments, W21 argued that it could be an accretion driven outflow originating in the BLR.

Geometry & properties of the X-ray source

At higher accretion rates, a thicker disk geometry is expected (see subsection 4.1.2). To account for this effect, e.g. Taylor & Reynolds (2018) allow for a varying scale height for the disk. In such a scenario, the inner region could form a funnel-like geometry and thereby enhance the observed reflection fraction. However, as the Eddington ratio computed by W21 for ESO 033-G002 is $\epsilon_{\mathrm{Edd}} \sim 0.02$, the system is still in a state in which a geometrically thin accretion disk is expected. The authors conclude that the high measured R_{frac} really must indicate a geometrically compact corona located close to the black hole.

W21 also estimated the size of the X-ray source via equation Equation 4.2.3, under the assumption that it is spherical, and that it needs to intercept a certain fraction of disk photons in order to produce the observed X-ray luminosity. The type-II Seyfert classification of ESO 033-G002 indicates that the low energy flux is absorbed by dust, i.e. the disk luminosity is not measurable; instead, the bolometric correction $\kappa_{2\text{–}10} = L_{\mathrm{bol}}/L_{2\text{–}10} \sim 10$ computed by W21 for the measured flux in the 2–10 keV regime serves as a proxy for the ratio between disk and source flux. With this W21 find the coronal radius to be $dh \sim 0.2\,r_{\mathrm{g}}$, which easily satisfies the condition $dh < h < 2\,r_{\mathrm{g}}$ so that the corona can fit above the event horizon.

W21 could constrain the electron temperature of the corona to the range $kT_{\mathrm{e}} = 40\text{–}70\,\mathrm{keV}$. Following Fabian et al. (2015), the temperature and the compactness parameter l_{c} (defined in Equation 4.2.2) together form a plane which acts as a thermostat for the corona. Above this limit, electron-positron pair production from photon-photon collisions inside the corona becomes a runaway process and effectively limits the rise of kT_{e}. For a radially compact corona, this happens at $kT_{\mathrm{e}} \sim 100\,\mathrm{keV}$. Comparing the compactness $l \sim 230$ of ESO 033-G002 with the constraints on the temperature, W21 find the source to be located close to the pair production limit which, despite its compact geometry, is in line with many other AGN.

8.1.2 Changes in binning and model choice

W21 rebinned the raw data to achieve a SNR of 5 for all instruments. I instead used the optimal binning routine (Kaastra & Bleeker, 2016) to determine the optimal bin size so that the SNR is as high as possible without losing information. The data sets for the two different binning choices are shown in Figure 8.2. It is evident that the binning of W21 was still too small for the amount of information that is actually contained in the data. Above 20 keV, however, optimal binning leads to much larger errorbars, since both the detection efficiency and the radiation yield in this regime are bad. For presentation purposes, I therefore rebinned the data above 20 keV to a minimum number of 80 counts per bin.

Furthermore, some models have been improved since the time of the analysis of W21. I therefore use `APEC` and `TBNEW` instead of `MEKAL` and `TBABS` for modeling diffuse emission and neutral absorption, respectively. No substantial changes in the fit results are expected because of this.

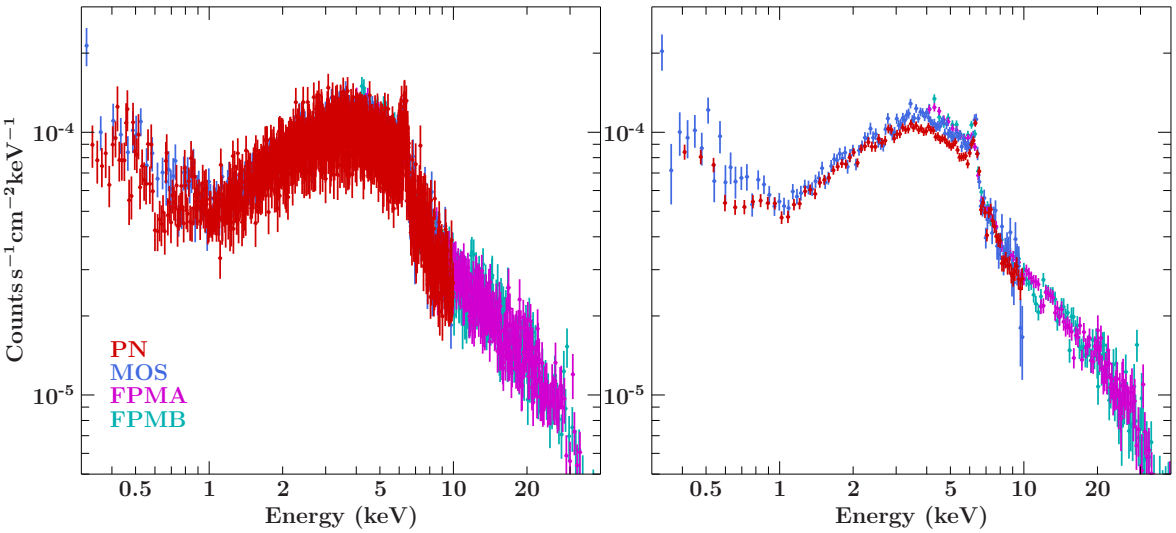

Figure 8.2: *Left:* The data unfolded with the detector response, binned to SNR=5. *Right:* The data unfolded with the detector response, using the optimal binning routine (Kaastra & Bleeker, 2016) to determine the bin sizes.

8.2 Differences between the model versions

For the currently published version of relxilllp (Dauser et al., 2013; García et al., 2014, version 2.2), denoted by relxilllpCp, three distinct radial ionisation gradients can be chosen for fitting. The powerlaw gradient follows

$$\xi(r) = r^{-p}, \tag{8.2.1}$$

with p describing the powerlaw index, i.e. the radial steepness of the ionisation profile. This kind of gradient was established to empirically account for the steepening of the irradiation profile for small radii in the lamppost geometry, which naturally results in a steepening of the ionisation profile as well, since the ionisation is directly proportional to the flux (see Equation 4.2.4). It therefore serves a similar purpose than the approach of modeling the irradiation profile as a broken powerlaw when no assumptions about the source geometry can be made. In the lamppost geometry, however, the exact shape of the irradiation profile is known (compare section 5.2). Secondly, from Equation 4.2.4 it is known that the ionisation depends on the electron density in the disk. The intrinsic density gradient of a disk, for which the thin disk approximation holds, is the α-disk density gradient, as was argued in chapter 4. With the information of both the irradiation profile and the radial density gradient, an α-disk like ionisation gradient can be established. Compared to the powerlaw gradient, the α-gradient is more strict and physical in its assumptions, and no longer needs an extra parameter modeling the steepness of the ionisation profile. The third option for relxilllpCp is to set the powerlaw gradient index to zero, thereby assuming a constant ionisation across the disk.

However, all these possible models still require the absolute value of the disk ionisation as a free parameter, i.e. they ignore the observed flux and may be incompatible with it. For the powerlaw gradient, the ionisation parameter gives the absolute value of the ionisation at the inner edge r_{in}; therefore it determines the maximal ionisation in the gradient. For the α-disk gradient, it gives the absolute ionisation at $r = (11/9)^2\, r_{\mathrm{in}}$, because the ionisation is maximal at this radius and decreases again for smaller radii. Since the α-disk density gradient predicts an increase of density for the innermost and the outer radii, a density minimum (and

therefore an ionisation maximum) can be found in between.

In order to take all assumptions plus the observed flux properly into account, an improved model should no longer contain the ionisation as a free parameter. The new relxilllp model, denoted by *relxilllpAlpha* (version 2.3.5), calculates the ionisation at the inner edge self-consistently and either implements an α-disk density gradient or a radially constant density. Other than relxilllpCp without an ionisation gradient, relxilllpAlpha always calculates an ionisation gradient from the incident irradiation profile, even for a constant density. From density information and ionisation at the inner edge, the ionisation gradient and its absolute values are completely determined by the data. As was explained in the previous chapter, the ionisation can be calculated by the black hole mass, the distance between source and observer, and the unobscured flux of the primary source.

The mass of the central black hole was estimated by W21 using the correlation between photon index and Eddington limit, which yielded $\log[M_{\mathrm{BH}}/M_{\odot}] \sim 7.3$ with uncertainties of almost one order of magnitude. This number can, however, still be regarded as significant, since measurements of the BAT AGN spectroscopic survey team (BASS, Koss et al., 2017) give similar results with much smaller errors ($\log[M_{\mathrm{BH}}/M_{\odot}] \sim 7.5 \pm 0.4$). As a black hole mass, I therefore chose $\log[M_{\mathrm{BH}}/M_{\odot}] = 7.3$. The Hubble distance of ESO 033-G002 to earth is $D = 80.58\,\mathrm{Mpc}$ (calculated form the given redshift). The primary flux takes the role of flux normalization in the Alpha model; this means it is a free parameter and can be fitted.

8.3 Results

In the following, the performance of the self-consistent relxilllpAlpha model will be compared to that of the relxilllpCp model, using the versions introduced in section 8.2. The physical reasons behind emerging differences will be discussed.

8.3.1 Analysis

Reproducing the previous results

By the time W21 carried out their analysis of ESO 033-G002, relxilllpCp was still only available in an older version (1.11.3). It did not allow for a variable density and powerlaw ionisation gradient at the same time. Therefore W21 fitted each model flavor separately, once for a variable density and once for a variable ionisation gradient index. In doing so, they found that both density and ionisation index tended back to their lower limit of 15 and 0 in the fit, noting that this may be because of the heavy absorption below 1.5 keV. Also, the smaller effective area at low X-ray energies for the XMM-Newton detectors could play a role here (see Figure 6.2). Moreover, the α-disk density gradient was still not implemented in relxilllpCp. In order to have consistency between my own fits of relxilllpCp, and in order to be able to fit the model with an α-gradient for comparing it to relxilllpAlpha, I start by showing that relxilllp version 1.11.3 and relxilllp version 2.2 produce similar results. Also, differences (although not statistically significant ones) to the results from W21 are expected, since I did not bin the data to achieve a SNR of 5, but rather used the optimal binning routine (see section 7.3).

Since the development of relxill version 2.2, it is possible to include returning radiation in the model, i.e. allow for the irradiating flux to be reflected on the disk more than once (see section 5.2). Remember that the effects of returning radiation are strongest for a compact disk-corona geometry and high black hole spin. Since W21 found evidence for both, a rapidly spinning black hole and a very low source height for ESO 033-G002, including returning radiation seems necessary for a more physical treatment of the reflection. I therefore included

Table 8.1: Best fit parameters and 90 % error intervals of the fits produced by W21 (OG) for relxilllp v. 1.11.3, and my fits for relxilllp v. 2.2 (Cp). The columns labeled with $boost = 1$ contain the fits where $R_{\rm frac}$ is calculated internally for a perfect lamppost geometry.

component	param	OG	OG (boost=1)	Cp	Cp (boost=1)
$\mathrm{tbabs_{full}}$	$N_{\rm H}$ $[\times 10^{22}\,\mathrm{cm^{-2}}]$	1.2 ± 0.1	1.3 ± 0.1	$1.3^{+0.1}_{-0.2}$	1.4 ± 0.1
$\mathrm{tbabs_{part}}$	$N_{\rm H}$ $[\times 10^{22}\,\mathrm{cm^{-2}}]$	5.4 ± 0.7	$5.8\pm^{+0.3}_{-0.5}$	$5.9^{+0.7}_{-1.1}$	$6.4^{+0.6}_{-0.7}$
	$C_{\rm f}$ [%]	79 ± 2	80^{+1}_{-2}	80^{+2}_{-3}	80 ± 2
xstar	$\log(\xi)$	$3.46^{+0.04}_{-0.05}$	$3.46^{+0.05}_{-0.04}$	3.45 ± 0.05	3.45 ± 0.05
	$N_{\rm H}$ $[\times 10^{22}\,\mathrm{cm^{-2}}]$	$5.3^{+2.0}_{-1.4}$	$6.0^{+1.2}_{-1.0}$	$6.9^{+2.1}_{-2.7}$	$6.9^{+2.7}_{-1.9}$
	$v_{\rm out}$ $[\mathrm{km\,s^{-1}}]$	5400^{+600}_{-700}	5400^{+600}_{-700}	420^{+690}_{-760}	360^{+780}_{-800}
mekal/apec	norm $[\times 10^{-6}]$	7.8 ± 1.8	8.1 ± 1.7	$6.0^{+1.5}_{-1.6}$	$5.8^{+1.7}_{-1.6}$
	kT [keV]	$0.70^{+0.09}_{-0.06}$	$0.70^{+0.09}_{-0.06}$	$0.87^{+0.08}_{-0.07}$	$0.88^{+0.09}_{-0.08}$
nthComp	norm $[\times 10^{-5}]$	$2.9^{+0.3}_{-0.4}$	$2.8^{+0.4}_{-0.3}$	3.2 ± 0.4	$3.3^{+0.4}_{-0.5}$
xillver	norm $[\times 10^{-6}]$	$7.9^{+2.3}_{-1.2}$	$9.3^{+2.1}_{-1.7}$	$10.0^{+3.0}_{-3.1}$	$11.7^{+3.0}_{-2.5}$
relxill	norm $[\times 10^{-4}]$	$7.2^{+3.6}_{-3.9}$	$5.8^{+4.6}_{-1.0}$	$8.0^{+6.0}_{-4.0}$	$3.9^{+0.9}_{-0.7}$
	i [deg]	$50.0^{+3.0}_{-2.0}$	49.0 ± 2.0	$46.3^{+3.3}_{-2.8}$	$44.3^{+2.8}_{-3.3}$
	a	> 0.960	> 0.960	> 0.958	> 0.945
	h $[\mathrm{r_+}]$	< 2.10	< 2.00	< 1.68	< 1.86
	Γ	$1.71^{+0.06}_{-0.07}$	$1.71^{+0.05}_{-0.07}$	$1.71^{+0.07}_{-0.11}$	$1.67^{+0.07}_{-0.05}$
	$\log(\xi)$	$3.1^{+0.3}_{-0.2}$	3.2 ± 0.2	$3.2^{+0.3}_{-0.2}$	$3.4^{+0.2}_{-0.3}$
	$\log(N)$	< 17.7	< 17.9	< 15.3	< 17.5
	$A_{\rm Fe}$ [solar]	$4.8^{+1.7}_{-0.9}$	$4.1^{+0.4}_{-0.5}$	$3.9^{+2.3}_{-0.7}$	$3.5^{+1.0}_{-0.8}$
	$kT_{\rm e}$ [keV]	46^{+14}_{-8}	46^{+18}_{-12}	46^{+23}_{-9}	46^{+18}_{-11}
	$boost\,(R_{\rm frac})$	$(4.1^{+2.8}_{-1.0})$	1 (5.3)	0.5 ± 0.2 (2.4)	1 (4.5)
fit stat.	χ^2	2509	2510	527.7	531.3
	$\chi^2_{\rm red}$	0.99	0.99	1.15	1.15
	# params [free]	60 [20]	60 [19]	61 [20]	61 [19]

it in my reflection model. Shortly, I will argue that the changes in the best fit parameters due to returning radiation are not statistically significant.

For comparing my own results to those results of W21 which neglected the ionisation gradient, I set the ionisation gradient index to $p = 0$ in relxilllp version 2.2. Table 8.1 shows the best fit parameters and the corresponding fit statistics for the original fit by W21 and my own fit. The fits that assume a perfect lamppost geometry, i.e. where the reflection fraction is calculated self-consistently (denoted by boost=1), are included in Table 8.1 for each model as well. In these fits, the amount of reflected flux in the total flux, as opposed to the amount of unreflected primary flux, is calculated internally from the height of the source and the black hole spin (see subsection 5.4.1). This poses strict constraints on the geometry of the source, i.e. a perfect, stationary point source lamppost is assumed. When the reflection fraction deviates from this intrinsic value, the data might show evidence for a different geometry. The boost parameter thereby denotes the value by which the intrinsic reflection fraction has to be multiplied in order to receive the fitted value.

Despite the different binning and the inclusion of returning radiation, the version 2.2 of relxilllp produces solutions that are consistent with the solutions found by W21. Overall, the fits indicate a rapidly spinning black hole ($a < 0.95$), a very compact source geometry ($h < 2\,r_+ = 2.6\,r_\mathrm{g}$) and a supersolar iron abundance in the disk ($A_\mathrm{Fe} > 3.5$). The ionisation stage is high, but not extreme ($\log(\xi) < 3.4$), and the disk density tends back to the lower limit of $\log(N) = 15$ in all cases. The outflow velocity of the ionized absorber, modeled by the redshift of the xstar component, is much lower than what was found by W21 ($400\,\mathrm{km\,s^{-1}}$ compared to $4500\,\mathrm{km\,s^{-1}}$), and the errors allow for a negative velocity. This is probably caused by the larger binning I used, compared to the binning of W21. With a sparse enough energy coverage, the absorption line positions can easily differ, which results in a large difference in velocity.

Only the new solution for a fixed boost shows small differences in the parameters of relxilllpAlpha that are, however, still largely consistent within the 90 % error intervals. Most notable is a smaller predicted inclination of $i = 41 - 47°$, compared to $i = 47 - 51°$. Also, the fixed boost solution produces a slightly worse fit than the solution for a free boost parameter ($\Delta\chi^2 = 3.6$), though when the number of free parameters is considered, the reduced χ^2 is very similar ($\chi^2_\mathrm{red} = 1.15$). Apart from that, the newer version predicts a lower reflection fraction when the boost is left free ($R = 2.4$, while the lower limit for the older version is $R = 3.1$). For a fixed boost, the reflection fraction is rather similar for both versions ($R = 5.3$ and $R = 4.5$, respectively). It can be said that for the new model, too, the lamppost geometry fits the data well. In the following, I will therefore concentrate on the solutions with a boost parameter fixed to 1.

In order to check which changes in the parameters can be attributed to the inclusion of returning radiation, I fitted relxilllp version 2.2 again with a free boost parameter, but switched off returning radiation this time. The results can be seen in the far left column of Table 8.2. Clearly, the solution without returning radiation is consistent with both the original solution and the solution with returning radiation within the 90 % error intervals, but is now much closer to the former: inclination ($i \approx 52°$), photon index ($\Gamma \approx 1.7$) and iron abundance ($A_\mathrm{Fe} \approx 5$) are almost identical with the original solution. On the one hand, this means that the influence of the change in bin size on the fit is negligible. On the other hand, it indicates that for this particular data set, not including returning radiation in the reflection model results in a slight overestimate of the inclination angle, the photon index, and the iron abundance. The exact physical implications behind these differences are very complicated and shall not be discussed further in this thesis. Nevertheless, I regard my own fits with relxilllpCp with constant ionisation as a successful recreation of the original fits.

In Figure 8.3, the residuals for the version 2.2 of relxilllp with a constant ionisation and a fixed boost are shown in the uppermost panel, followed by all other fixed boost solutions that will be presented in the course of this section, as marked individually for each panel. First, it is evident that all residuals exhibit no major unresolved features. Second, no large-scale differences can be seen when comparing them. Together with the similar χ^2 values, this means that all model versions fit the data equally well.

Solutions for a powerlaw ionisation gradient

Because of the changes in the fit parameters due to the presence of returning radiation, it would also be interesting to see if the model still predicts a flat ionisation gradient. Therefore, I allowed for a powerlaw ionisation gradient in the next three fits. Furthermore, I allowed for a coronal velocity, since it might also impact the other parameters in a nontrivial way, even though W21 neglected this possibility (see subsection 5.4.2 for how the velocity impacts the spectral shape). The results for a free and fixed boost parameter are depicted in the two

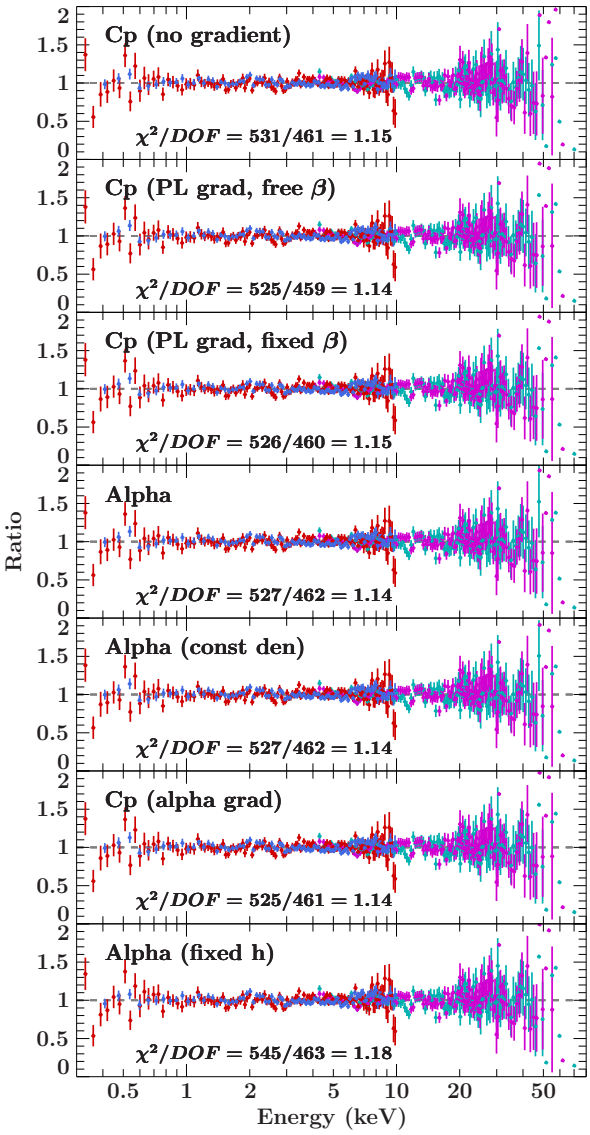

Figure 8.3: Residual plots for all fits with *boost* = 1. The colors indicate the datasets of PN (blue), MOS (red), FPMA (magenta) and FPMB (cyan).

middle columns in Table 8.2.

Despite the fact that W21 found a constant ionisation, I found evidence for a nonzero gradient in relxilllpCp for both free and fixed boost, although the errors are large and include the upper limit $p < 0.31$ from the original fit in the case of a fixed boost, but not for a free boost (giving the limit $p < 0.46$, see the results of W21). The boost as well as the reflection fraction in the free boost solution are much higher than for relxilllpCp without a gradient, although entirely unconstrained within the limits of 0 to 10. Also, a significantly higher ionisation is predicted, with a lower error of at least $\log(\xi) = 4.1$, and an upper error including the upper limit of $\log(\xi) = 4.7$.

The upwards velocity of the corona also catches the eye here. When the boost is fixed, the velocity rises dramatically from zero to over 0.5 c, though the lower limit still includes zero. I concluded that having both parameters free allows for too many degrees of freedom and fixed β at zero again in the following fits. The solution for fixed boost and fixed β is shown in the far right column of Table 8.2. Interestingly, even though fixing more parameters should result in tighter constrained errors, the uncertainties on spin and height increase, allowing for a spin as low as ~ 0.3 in the case of fixed boost and β. The best fit height also is larger than $2.6\,r_g$ in this case, predicting $h = 3.2\,r_g$ with an upper confidence of $h = 5.0\,r_g$.

Table 8.2: Best fit parameters and 90 % error intervals of the fits for relxilllp v. 2.2 without returning radiation (Cp RR0), with free coronal velocity (Cp2) or fixed coronal veloctiy (Cp β0). The columns labeled with *boost* = 1 contain the fits where $R_{\rm frac}$ is calculated internally for a perfect lamppost geometry. * Parameters that were fixed during fitting.

component	param	Cp (RR0)	Cp2	Cp2 (boost=1)	Cp2 (b1β0)
$\text{tbabs}_{\text{full}}$	$N_{\rm H}$ [$\times 10^{22}\,\text{cm}^{-2}$]	1.3 ± 0.2	1.2 ± 0.2	$1.2^{+0.2}_{-0.3}$	$1.2^{+0.2}_{-0.3}$
$\text{tbabs}_{\text{part}}$	$N_{\rm H}$ [$\times 10^{22}\,\text{cm}^{-2}$]	$5.3^{+0.8}_{-1.0}$	$5.4^{+0.8}_{-1.1}$	$5.7^{+0.8}_{-1.2}$	$5.4^{+0.9}_{-1.2}$
	$C_{\rm f}$ [%]	78 ± 2	78 ± 2	79 ± 2	79 ± 2
xstar	$\log(\xi)$	$3.44^{+0.05}_{-0.06}$	3.44 ± 0.05	$3.44^{+0.05}_{-0.06}$	$3.43^{+0.05}_{-0.07}$
	$N_{\rm H}$ [$\times 10^{22}\,\text{cm}^{-2}$]	$4.8^{+1.8}_{-1.7}$	$5.0^{+2.0}_{-1.8}$	$5.2^{+2.9}_{-2.2}$	$4.8^{+2.5}_{-2.1}$
	$v_{\rm out}$ [$\text{km}\,\text{s}^{-1}$]	390^{+780}_{-780}	370^{+720}_{-800}	360^{+720}_{-780}	360^{+780}_{-780}
apec	norm [$\times 10^{-6}$]	$5.8^{+1.7}_{-1.6}$	$5.4^{+1.7}_{-1.5}$	$5.2^{+1.7}_{-1.6}$	5.3 ± 1.7
	kT [keV]	0.88 ± 0.08	0.90 ± 0.09	0.90 ± 0.09	$0.90^{+0.10}_{-0.09}$
nthComp	norm [$\times 10^{-5}$]	3.3 ± 0.4	3.4 ± 0.4	$3.6^{+0.3}_{-0.4}$	$3.5^{+0.4}_{-0.5}$
xillver	norm [$\times 10^{-6}$]	$8.8^{+2.7}_{-1.9}$	$8.6^{+2.7}_{-1.9}$	$8.0^{+2.7}_{-2.0}$	$7.0^{+2.6}_{-2.0}$
relxill	norm	$1.0^{+1.0}_{-0.6} \times 10^{-3}$	$> 1.2 \times 10^{-5}$	$> 4.9 \times 10^{-5}$	$> 4.5 \times 10^{-5}$
	i [deg]	$51.9^{+4.0}_{-3.4}$	$47.4^{+1.8}_{-1.8}$	$47.6^{+2.8}_{-2.5}$	$47.7^{+2.4}_{-3.1}$
	a	> 0.975	> 0.465	> 0.50	> 0.285
	h [r_+]	< 1.69	< 2.35	< 2.58	< 3.78
	Γ	$1.69^{+0.08}_{-0.07}$	$1.61^{+0.07}_{-0.06}$	$1.63^{+0.05}_{-0.07}$	$1.63^{+0.09}_{-0.05}$
	β [c]	0.0*	< 0.52	< 0.74	0.0*
	$\log(\xi)$	$3.11^{+0.22}_{-0.33}$	> 4.30	> 4.1	> 3.90
	$\log(N)$	< 18.0	< 18.6	< 18.7	< 19.1
	$A_{\rm Fe}$ [solar]	$5.0^{+2.5}_{-1.3}$	$5.0^{+2.4}_{-1.0}$	$5.2^{+3.8}_{-1.6}$	$5.9^{+3.4}_{-1.9}$
	$kT_{\rm e}$ [keV]	38^{+16}_{-7}	33^{+9}_{-6}	30^{+11}_{-8}	23^{+8}_{-6}
	p	0.0*	$1.4^{+0.4}_{-0.6}$	$0.9^{+1.0}_{-0.7}$	$1.1^{+1.4}_{-0.7}$
	boost ($R_{\rm frac}$)	$0.5^{+0.4}_{-0.1}$ (3.0)	$5.3^{+4.7}_{-5.3}$ (>10)	1 (3.2)	1 (3.1)
fit stat.	χ^2	523.3	524.5	525.4	525.4
	$\chi^2_{\rm red}$	1.14	1.15	1.14	1.15
	# params [free]	61 [20]	61 [22]	61 [21]	61 [20]

Before, it always tended against the limit of $2.0\,r_{\rm g}$ with an upper confidence of $h = 3.3\,r_{\rm g}$. Otherwise, still a significantly higher ionisation with $\log(\xi) > 3.9$ is predicted. But in the end, it should be noted that all solutions for relxilllpCp with a powerlaw ionisation gradient, too, are largely consistent with the original fits within the error intervals, with an exception of a higher ionisation and a slight evidence for an ionisation gradient.

The powerlaw ionisation gradient, however, is still only an empirical tool for roughly describing a physical ionization gradient produced by a varying irradiation and density across the radial extend of the disk. In order to isolate the ionisation parameter completely from the influence of the gradient, I fitted the relxilllpCp model with an α-disk density gradient to the data, both for a free and fixed boost parameter, as presented in the two left columns of Table 8.3. Now that the ionisation gradient is derived from the density gradient and the irradiation profile, only the absolute value of the ionisation remains for the model in order to

Table 8.3: Best fit parameters and 90 % error intervals of the fits for relxilllp v. 2.2 assuming an α-disk density gradient, and the fits for relxilllpAlpha (Alpha). The columns labeled with *boost* = 1 contain the fits where $R_{\rm frac}$ is calculated internally for a perfect lamppost geometry. * Parameters that were fixed during fitting. † relxilllpAlpha gives the normalization in physical flux units of erg cm^{-2} s^{-1}.

component	param	Cp-α	Cp-α (boost=1)	Alpha	Alpha (boost=1)
tbabs$_{\rm full}$	$N_{\rm H}$ [$\times10^{22}$ cm^{-2}]	$1.2^{+0.2}_{-0.3}$	$1.2^{+0.2}_{-0.3}$	$1.2^{+0.1}_{-0.2}$	1.3 ± 0.1
tbabs$_{\rm part}$	$N_{\rm H}$ [$\times10^{22}$ cm^{-2}]	$5.6^{1.0}_{-1.3}$	$5.5^{+0.9}_{-1.2}$	$5.1^{+1.0}_{-0.7}$	6.3 ± 0.4
	$C_{\rm f}$ [%]	78 ± 2	79 ± 2	80 ± 2	82^{+1}_{-2}
xstar	log(ξ)	3.44 ± 0.06	$3.43^{+0.06}_{-0.07}$	3.45 ± 0.05	$3.46^{+0.05}_{-0.06}$
	$N_{\rm H}$ [$\times10^{22}$ cm^{-2}]	$4.8^{+2.1}_{-1.8}$	$4.7^{+2.7}_{-2.2}$	$5.5^{+2.1}_{-1.8}$	$8.9^{+1.2}_{-1.3}$
	$v_{\rm out}$ [km s^{-1}]	320^{+750}_{-780}	320^{+750}_{-870}	510 ± 720	690^{+670}_{-690}
apec	norm [$\times10^{-6}$]	$4.9^{+1.8}_{1.5}$	5.5 ± 1.7	$6.1^{+1.6}_{-1.5}$	$7.0^{+1.7}_{-1.5}$
	kT [keV]	$0.90^{+0.10}_{-0.09}$	$0.89^{+0.09}_{-0.08}$	$0.87^{+0.08}_{-0.07}$	0.85 ± 0.07
nthComp	norm [$\times10^{-5}$]	$3.67^{+0.28}_{-0.04}$	3.4 ± 0.4	3.4 ± 0.4	$2.77^{+0.26}_{-0.38}$
xillver	norm [$\times10^{-6}$]	$7.7^{+2.5}_{-2.1}$	$6.9^{+2.6}_{-2.0}$	$7.7^{+2.4}_{-1.3}$	$9.6^{+1.8}_{-1.6}$
relxill	norm	$> 8.0 \times 10^{-6}$	$> 4.1 \times 10^{-5}$	$1.72^{+0.22}_{-0.74} \times 10^{-12}$†	$1.26^{+0.13}_{-0.05} \times 10^{-11}$†
	i [deg]	$47.7^{+2.1}_{-2.6}$	$47.4^{+3.2}_{-2.7}$	$54.1^{+2.5}_{-1.1}$	$51.7^{+1.0}_{-1.1}$
	a	> 0.930	> 0.918	> 0.979	> 0.995
	h [r$_+$]	$2.2^{+1.3}_{-0.6}$	$2.8^{+2.2}_{-0.9}$	2.2*	2.8*
	Γ	$1.60^{+0.08}_{-0.06}$	$1.65^{+0.08}_{-0.09}$	$1.73^{+0.06}_{-0.05}$	$1.80^{+0.03}_{-0.02}$
	log(ξ)	$3.19^{+0.23}_{-0.37}$	$2.70^{+0.62}_{-0.40}$	[3.45]	[3.69]
	log(N)	< 19.0	< 18.9	< 15.3	< 15.1
	$A_{\rm Fe}$ [solar]	$5.7^{+3.5}_{-1.8}$	$5.6^{+3.4}_{-1.8}$	$5.0^{+2.0}_{-1.2}$	3.5 ± 0.3
	$kT_{\rm e}$ [keV]	27^{+12}_{-4}	21^{+7}_{-4}	25^{+8}_{-4}	28^{+10}_{-4}
	boost ($R_{\rm frac}$)	$9.9^{+0.1}_{-9.9}$ (>10)	1 (2.6)	$0.47^{+0.21}_{-0.12}$ (1.7)	1 (3.3)
fit stat.	χ^2	524.0	525.0	532.4	545.1
	$\chi^2_{\rm red}$	1.14	1.14	1.15	1.18
	# params [free]	61[20]	61 [19]	60 [18]	60 [17]

adapt the ionisation structure of the disk to the data. Compared to all the previous relxilllpCp fits, the primary source height is now larger with a more tightly constrained lower error ($h = 2.1$–$4.6\,r_{\rm g}$), and the ionisation is slightly lower, especially for the fixed boost solution (log(ξ) = 2.3–3.3). The boost parameter, again, increases almost to the upper limit of 10, and again includes the lower limits of 0 within its confidence intervals. But also here, most parameters are consistent with the original fit within the 90 % errors. So apparently, there is a strong correlation between the ionisation gradient model and the other parameters.

Solutions for a self-consistent ionisation

After I reproduced the fits of W21 with the version 2.2 of relxilllp, I exchanged the model by the Alpha version. Now, the distance between source and observer, and the black hole mass need to be given to the model. The normalization of the relxill component can therefore be given in physical flux units, i.e. erg cm^{-2} s^{-1}. Intrinsically, again an α-disk density gradient is assumed. With this, the absolute value of the ionisation is calculated for each unit radius.

In Table 8.4, the best fits for relxilllpAlpha are shown in the two left columns. The main

Table 8.4: Best fit parameters and 90 % error intervals of the fits for relxilllpAlpha assuming an α-disk density gradient (Alpha) or a constant density (AlphaCD). The columns labeled with $boost = 1$ contain the fits where $R_{\rm frac}$ is calculated internally for a perfect lamppost geometry. † relxilllpAlpha gives the normalization in physical flux units of $\mathrm{erg\,cm^{-2}\,s^{-1}}$.

component	param	Alpha	Alpha (b=1)	AlphaCD	AlphaCD (b=1)
$\mathrm{tbabs_{full}}$	$N_{\rm H}$ $[\times 10^{22}\,\mathrm{cm^{-2}}]$	1.3 ± 0.1	1.3 ± 0.1	1.3 ± 0.1	1.2 ± 0.1
$\mathrm{tbabs_{part}}$	$N_{\rm H}$ $[\times 10^{22}\,\mathrm{cm^{-2}}]$	$6.2^{+0.6}_{-0.5}$	$5.9^{+0.6}_{-0.8}$	$5.8^{+0.8}_{-0.6}$	$5.7^{+0.7}_{-1.1}$
	$C_{\rm f}$ [%]	80 ± 2	79 ± 2	78 ± 2	79 ± 2
xstar	$\log(\xi)$	3.45 ± 0.05	$3.44^{+0.05}_{-0.06}$	3.45 ± 0.05	$3.44^{+0.05}_{-0.07}$
	$N_{\rm H}$ $[\times 10^{22}\,\mathrm{cm^{-2}}]$	$5.9^{+1.4}_{-1.0}$	$4.9^{+1.7}_{-1.4}$	$5.8^{-1.8}_{-1.2}$	$5.3^{+1.8}_{-2.0}$
	$v_{\rm out}$ $[\mathrm{km\,s^{-1}}]$	480 ± 720	420^{+720}_{-750}	450^{+690}_{-720}	420^{+720}_{-780}
apec	norm $[\times 10^{-6}]$	5.8 ± 1.5	$5.3^{+1.6}_{-1.5}$	$4.8^{+1.6}_{-1.5}$	5.1 ± 1.6
	kT [keV]	$0.90^{+0.09}_{-0.08}$	0.90 ± 0.09	$0.90^{+0.10}_{-0.09}$	$0.90^{+0.10}_{-0.01}$
nthComp	norm $[\times 10^{-5}]$	$3.4^{+0.2}_{-0.3}$	3.6 ± 0.3	$3.7^{+0.2}_{0.4}$	3.6 ± 0.4
xillver	norm $[\times 10^{-6}]$	$9.9^{+2.3}_{-1.8}$	$9.0^{+2.0}_{-1.8}$	$8.9^{+2.7}_{-1.5}$	$8.7^{+2.2}_{-2.0}$
relxill	norm $[\times 10^{-12}]^{\dagger}$	$0.7^{+0.3}_{-0.1}$	$4.0^{+1.8}_{-0.2}$	$4.8^{+17.5}_{-0.3}$	$4.5^{+2.4}_{-0.6}$
	i [deg]	$49.8^{+1.6}_{1.5}$	$51.0^{+1.6}_{-1.8}$	$48.3^{+1.6}_{-1.5}$	$50.1^{+2.4}_{-2.0}$
	a	> 0.972	> 0.994	> 0.988	> 0.976
	h $[\mathrm{r_+}]$	< 1.66	< 1.75	< 1.74	< 1.88
	Γ	$1.64^{+0.05}_{-0.04}$	$1.63^{+0.05}_{-0.04}$	$1.60^{+0.07}_{-0.03}$	$1.62^{+0.07}_{-0.04}$
	$\log(\xi)$	[4.47]	[4.42]	[5.73]	[5.17]
	$\log(N)$	< 15.2	< 17.6	< 15.2	< 15.3
	$A_{\rm Fe}$ [solar]	4.6 ± 0.7	$5.3^{+1.6}_{-1.0}$	$4.9^{+1.0}_{-1.1}$	$5.3^{+2.6}_{-1.1}$
	$kT_{\rm e}$ [keV]	48^{+14}_{-9}	46^{+4}_{-11}	45^{+13}_{-8}	44^{+13}_{-11}
	$boost$ $(R_{\rm frac})$	$6.5^{+3.5}_{-6.5}$ (>10)	1 (9.5)	$9.9^{+0.1}_{-9.9}$ (>10)	1 (9.2)
fit stat.	χ^2	527.7	527.9	525.6	527.4
	$\chi^2_{\rm red}$	1.15	1.14	1.14	1.14
	# params [free]	62 [20]	62 [19]	60 [19]	60 [18]

result is that the solutions for both free and fixed boost are consistent with the original solutions. It is remarkable that the fit is just as good as for a fitted ionisation with red. $\chi^2 = 1.15$. Only now that the ionisation is calculated self-consistently, the model predicts a higher value of $log(\xi) = 4.4$, close to the maximally allowed ionisation of $log(\xi) = 4.7$, while relxilllpCp predicts a lower value of $log(\xi) = 3.0$–3.6. Also, the Alpha model predicts a much higher reflection fraction of $R = 9.5$ in the case of a fixed boost parameter, as opposed to relxilllpCp, which predicts a reflection fraction of $R = 2.4$ for a constant ionisation, and $R = 3.1$ for an ionisation gradient. Only the latter is consistent with the range of possible reflection fractions found in the original fit. By fitting the boost parameter, it increases to 6.5 and, again, has its confidence intervals within the upper and lower limits of 0 and 10.

The comparison of relxilllpAlpha to relxilllpCp with an α-disk gradient is especially interesting here, since the two models only differ in the way the disk ionisation is treated. Compared to the Alpha solution with a fixed boost parameter, especially the electron temperature is significantly lower for relxilllpCp ($kT_e = 17$–$28\,keV$, as opposed to $kT_e = 35$–$50\,keV$ for the Alpha model). Other than for relxilllpCp, no evidence for an increase in height can be found

for the Alpha model; the value tends back to the limit of $1.5\,r_+ = 1.9\,r_\mathrm{g}$ with an upper confidence of at most $2.2\,r_\mathrm{g}$ in the case of a fixed boost. Otherwise, most parameters are surprisingly similar.

As an additional feature of the Alpha model, the density gradient can be set to a constant density across the disk. This way, the ionisation gradient is only influenced by the irradiation profile. Since only the α-disk density gradient predicts an increase of density for the innermost radii, and therefore a decrease of ionisation, it is expected for the Alpha model with constant density to predict a higher ionisation for the inner radius. The results are shown in the two right columns of Table 8.4. Indeed, the calculated ionisation is $\log(\xi) = 5.2$ for a fixed boost parameter, and $\log(\xi) = 5.7$ for a free boost. All other parameters are consistent with the Alpha solution for a density gradient.

Lastly, I fitted the Alpha model with the source height fixed to the values predicted by relxilllpCp with an α-gradient ($h = 2.2\,r_+ = 2.6\,r_\mathrm{g}$ for the free boost solution, $h = 2.8\,r_+ = 3.2\,r_\mathrm{g}$ for a fixed boost), so that the irradiation profiles are as similar as possible. Like this, the differences in the other parameters can be exemplified better. The best fits are presented in the two right columns of Table 8.3. It is clearly visible that especially the fixed boost solutions are quite different. The iron abundance is lower for the Alpha model (at most $A_{Fe} = 3.8$, which barely coincides with the lower uncertainty of the same value for relxilllpCp) and the photon index is also significantly higher (at least $\Gamma = 1.78$, while the upper uncertainty for relxilllpCp is $\Gamma = 1.73$). Most importantly, the ionisation, while it is consistent for the free boost solutions, is lower for relxilllpCp with an α-gradient and a fixed boost; the Alpha model solution shows that at a source height of $h = 2.8\,\mathrm{r_+}$, the ionisation is actually close to $\log(\xi) = 3.7$, while relxilllpCp predicts an ionisation of at most $\log(\xi) = 3.3$. Looking at the last panel of Figure 8.3, which shows the residuals for the fixed boost fit for the Alpha model at $h = 2.8\,r_+$, one can see that those are the only residuals exhibiting small but visible differences below 1 keV, compared to the residuals of relxilllpCp with an α-gradient in the panel above. This is likely the cause of the large increase of $\Delta\chi^2 = 20$ in fit statistic between the two models.

8.3.2 Discussion

In analysing the results for the different model versions, my main goal is to test the lamppost geometry by including the observed primary flux, and therefore a self-consistent ionisation. So far, I found that all fits are largely consistent among each other and show no large differences in the residuals over the observed energy range. Specifically, the fits with a boost parameter fixed to 1, i.e. those which assume a perfect lamppost geometry, are consistent among each other, and with the fits for which the boost parameter was fitted. For the latter, I mostly found that the boost parameter tended to values much larger than one, and that the 90 % confidence intervals included the limits of 0 and 10.

Regarding my own fits with the relxilllpCp model which, other than the relxilllpCp model from W21, included returning radiation and allowed for a powerlaw ionisation gradient, I found evidence for a nonzero ionisation gradient (even though the gradient index had large error intervals) and a higher fitted ionisation at the inner edge of the disk. When implementing a more physical α-disk density gradient in the relxilllpCp model, it predicted a lower ionisation than the model from W21. Both ionisation gradient models, however, predicted a larger source height and a smaller coronal electron temperature than the constant ionisation model from W21.

The new Alpha model, which not only implements an α-disk density gradient, but calculates the absolute ionisation for each unit radius from the primary flux of the source at a height h, produced surprisingly similar results to the original fits from W21, and had equally good fit

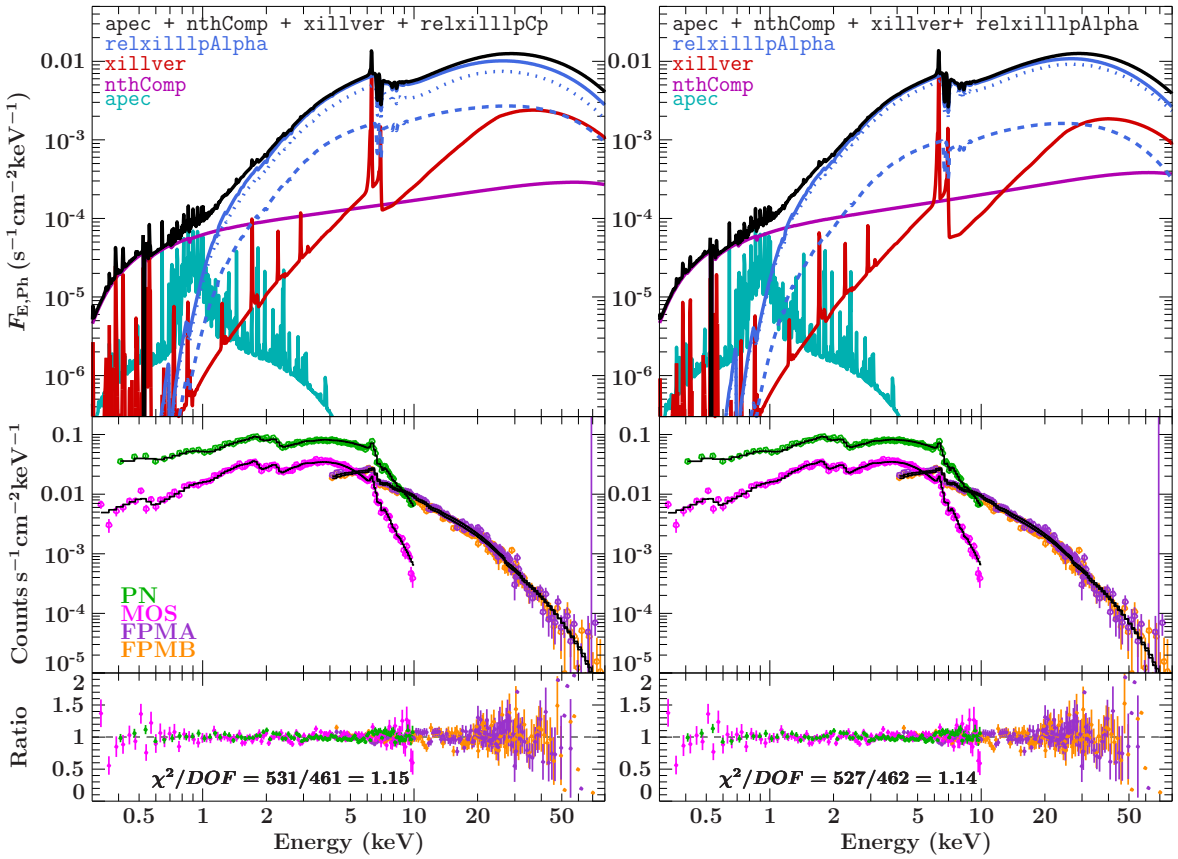

Figure 8.4: *Left:* plots for the relxilllpCp solution without ionisation gradient. *Right:* plots for the relxilllpAlpha solution. The upper panels show the individual model components alongside the total model spectrum; the middle panels show the original count spectrum together with the model histogram; the lower panels show the residuals.

statistics. Only the ionisation was generally predicted higher, even more so for the version of the Alpha model with a constant density. When fixing the source height at the value predicted by relxilllpCp with an α-gradient, the Alpha model showed that the low ionisation would be predicted higher when it is calculated self-consistently.

Similarity between fits

The different models I tested on the same data set produce very similar fits, regardless of how the ionisation and density gradient is treated. This may indicate that twenty or more free parameters, which are present in most of the fits, are not necessary to describe the data at this particular SNR sufficiently (the optimal binning routine I used to rebin the data chooses the bin size such that the SNR is as high as possible, but not so high that information is lost). It may also indicate that strong correlations exist between the parameters.

Nevertheless, the high SNR achived by optimal binning makes the fitting process susceptible for internal incongruities in the models. The fact that the new way of intrinsically calculating the ionisation archives a fit that is just as good as the fit for a fitted ionisation proves that indeed, the model with the more physical ionisation describes the data well, and that the lamppost geometry is a good fit for the data of ESO 033-G002, as was already concluded by W21. Furthermore, the fact that the model with a self-consistent ionisation produces fits with

parameters that are largely consistent within their 90 % error intervals with the ones from the fits of the model with a fitted ionisation, proves that the differences between the fitted spectra are, at best, minor, and will therefore only be visible in smaller energy bands.

The lamppost assumption, again, is also supported by other fit paramters: the overall low height, high spin, high reflection fraction and high ionisation level in all fits indicates a compact disk-corona geometry, where most of the primary flux is focused onto the innermost, highly relativistic disk region by the strong lightbending in the vicinity of the black hole, and subsequently ionizes this region almost completely. This particular setup is typical for a lamppost source, since its geometrically compact emission of X-rays is easily focused for a low source height. Finally, it can be said that the stricter conditions of taking the primary flux into account for the lamppost geometry still describe the spectrum of a real AGN well. This adds a piece of evidence to the validity of the lamppost approach.

To understand this further, we can take a look at the spectral components of the fits in Figure 8.4. The left plot shows the spectral components featuring the least physical model, i.e. where a constant density and ionisation across the disk is assumed, and where the ionisation itself was fitted; below, the count spectrum for each detector together with the best fit spectrum, and the residuals can be seen. On the right, the same is shown for the most physical model, i.e. where the ionisation is calculated across the disk from the primary flux profile and the α-disk density gradient. In both cases, the components reveal a strongly reflection dominated spectrum, which can be explained by the strong enhancement of the reflection fraction in a compact lamppost geometry due to lightbending, and a smooth reflection component with almost no features, except for a small Compton hump around 30 keV and a broad iron absorption edge around 7 keV. The latter reflects the high ionisation stage of the irradiated disk parts. The fact that both models support this particular solution shows, on the one hand, that the data itself contains strong evidence for highly ionized, highly relativistic reflection and a compact geometry. On the other hand, it shows that the predictions of the new model, which calculates the ionisation self-consistently, are in line with the predictions of current modeling practices of X-ray spectra.

Role of the boost parameter

When fitting the boost parameter, which gives a measure of how much the data requires deviation of the exact point source lamppost geometry, I found values much larger than one, and very large confidence intervals for this parameter in almost all model versions. The only exception is the model which assumes no density or ionisation gradient and neglects the primary flux. It predicted a reflection fraction around 0.5 with tighter constraints.

A boost parameter smaller than one could indicate an outwards moving corona (Dauser et al., 2013). The coronal velocity and the boost parameter control the strength of reflection features in the spectrum in a similar way: while a smaller boost parameter is an empirical way of reducing the reflected flux in relation to the primary flux, a corona moving upwards at relativistic speeds produces a similar effect by boosting the emission in the direction of its movement, thereby reducing the flux reflecting on the disk. However, as the dramatic increase of the velocity to half the speed of light showed when fitting the ionisation parameter with an empirical powerlaw gradient and fixing the boost parameter to one, the possibility of a moving corona simply exceeds the information that can be drawn out of the data set.

A boost parameter larger than one is not so easily interpreted. The lamppost geometry already should give the most extreme levels of reflection in the total spectrum. Even more focusing of the primary flux onto the disk than for a point source emitter is hardly possible. However, when the total spectrum, like in the case of a self-consistently calculated ionisation (as shown on the right in Figure 8.4) is already highly reflection dominated, the exact value of

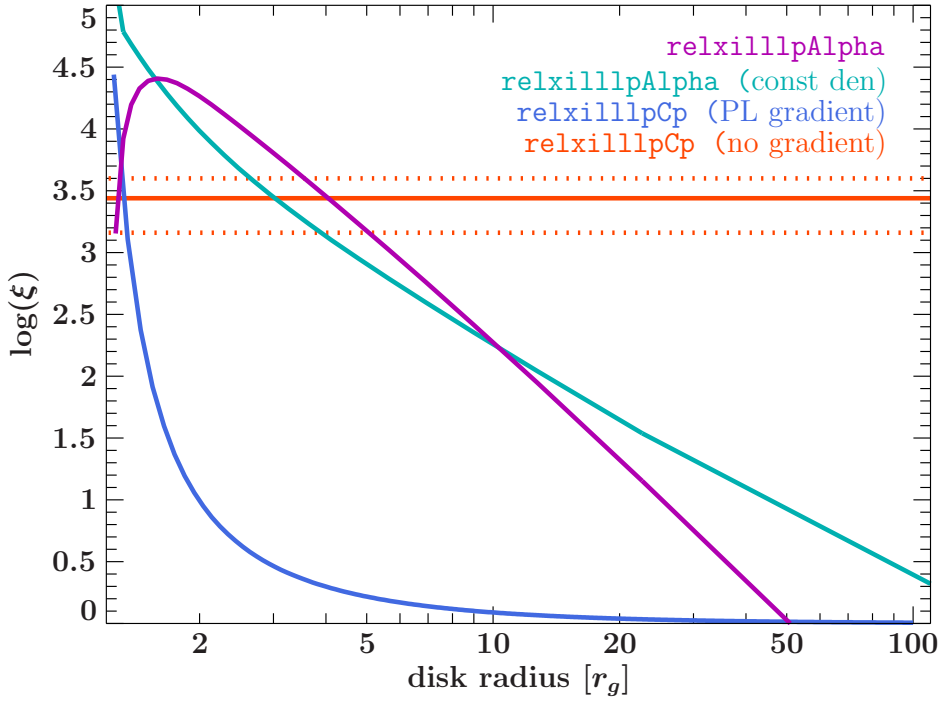

Figure 8.5: Ionisation gradients as functions of disk radius for the solutions Alpha (magenta), AlphaCD (cyan), Cp (orange) and Cp2 (blue) with the boost parameter fixed to one. The dashed lines indicate the 90 % error intervals.

the boost parameter does not make a large difference anymore, since the primary continuum is very weak. This likely causes the large confidence intervals. It also means that the high value of the boost parameter is not meaningful for interpretation.

Also, the source height can play a similar role as the boost parameter, since for an increased height, less flux is bent towards the disk, and more flux escapes without reflecting. When both, boost and velocity, were fixed in my solutions with a fitted ionisation with empirical and physical gradients, the height was left to control the strength of reflection line features, hence this parameter became less constrained towards higher values, or even predicted higher values directly. This also explains the low electron temperature compared to the solution without ionisation gradient: the larger source height results in the disk seeing a higher cutoff energy, therefore the fit compensates by lowering the actual cutoff.

Overall, two kinds of solutions seem to be present in the fits, represented by the two fits in Figure 8.4. One requires a smaller reflection fraction than predicted by the lamppost geometry and is not dominated by either reflection or primary emission, but contains those two components in an equal amount. The other is highly reflection dominated and allows for no constraints of the boost parameter within the limits of 0 and 10. These shall be investigated further in the following sections. But first, it is necessary to entangle the impact of the ionisation gradient on the parameters.

Connection between ionisation and ionisation gradient

While the model assuming a constant ionisation and density across the disk predicted an intermediate to high ionisation at the inner edge (which is located at around $1.25\,r_g$ for a maximally spinning black hole), the model assuming an empirical powerlaw ionisation gradient predicted an extremely high ionisation. At the same time, the fit statistic favoured

the presence of a steep gradient falling approximately like 1/r, though the error intervals on the gradient index were large. With a self-consistent ionisation and a more physical α-disk density gradient, the maximal predicted ionisation was almost as extreme as for the powerlaw gradient. It should be remembered, however, that the α-gradient model predicts a decrease of ionisation at the innermost radii due to an increase of density.

To showcase this, all ionisation gradients are depicted in Figure 8.5. The constant ionisation model, which is undoubtedly the least physical, predicts an ionisation level of around $\log(\xi) = 3.5$ for all radii. Neither irradiation profile nor varying density are taken into account. The powerlaw gradient model, which also does not take irradiation profile or density into account properly, but imitates the steep irradiation at the inner radii empirically, predicts a very high ionisation at the inner edge around $\log(\xi) = 4.5$, which falls off rapidly outwards, so that at $2\,r_{\mathrm{g}}$, the ionisation level is already lower than $\log(\xi) = 1$. When the ionisation level is calculated self-consistently, but still a constant density across the disk is assumed, the predicted ionisation at the inner edge is even higher ($\log(\xi) = 5.2$) and falls off more slowly that the powerlaw gradient, so that at $2\,r_{\mathrm{g}}$, the ionisation level is still at $\log(\xi) \sim 4$. This gradient reflects the actual irradiation profile from the lamppost source. Lastly, the model which calculates the ionisation for each radius from the impinging flux and the α-disk density profile, predicts a maximal ionisation of $\log(\xi) \sim 4.5$ at around $2\,r_{\mathrm{g}}$. For smaller radii, the ionisation decreases rapidly, until it reaches $\log(\xi) \sim 3$ at the inner edge. For larger radii, the decrease is almost linear; steeper than the irradiation-induced gradient, but more shallow that the powerlaw gradient.

The models which calculate the ionisation self-consistently take the physical assumptions of the thin accretion disk and the lamppost geometry properly into account. The models which fit the ionisation at the inner edge ignore those assumptions. In order to estimate the expected ionisation for the constant ionisation model, if it were calculated self-consistently from the other fit parameters, I can use the equations that were introduced in subsection 5.4.1, again assuming the same black hole mass and source distance as before. I measured the primary flux of the X-ray source by setting $R = 0$ in the model and summing the flux over the energy grid from 0.1 keV to 1.0 MeV, which gives the integrated flux $f_{\mathrm{E}} = 0.0049\,\mathrm{erg\,cm^{-2}\,s^{-1}}$. Since the ionisation estimate by hand only accounts for the gravitational energy shift and neglects all other relativistic effects, the actual ionisation at the inner edge is underestimated by a factor of around 2.25, which was also shown in subsection 5.4.1. When this correction factor is accounted for, I receive an ionisation of $\log(\xi) \sim 5.9$. The model which calculates the ionisation self-consistently without a density gradient predicts a similar value at the inner edge ($log(\xi) = 5.2$).

On the one hand, this implies that relxilllpCp significantly underestimates the ionisation at the inner edge, if the irradation profile were considered properly. On the other hand, the relxilllpCp solution that assumes a powerlaw ionisation gradient (but no density gradient), only gives a lower limit of $log(\xi) > 3.9$, which includes the more physical prediction. Allowing for an empirical ionisation gradient therefore seems to yield a solution closer to the predictions of the Alpha model.

This is easily understood when looking at what changes those parameters cause in the spectrum predicted by the fitted ionisation model. Spectra for different ionisation and gradient index values are plotted in figure Figure 8.6. When the ionisation is low ($\log(\xi) < 2$), also the reflection fraction is lower and therefore only weak reflection features are seen. A slight increase in ionisation leads to stronger low energy lines since more low energy photons than high energy photons exist for a powerlaw incident flux. The same is true for a steep ionisation gradient ($p > 1$), since only a small amount of reflected flux will then come from the outer disk parts. An intermediate ionisation ($\log(\xi) \sim 3$), on the other hand, equates to more reflected

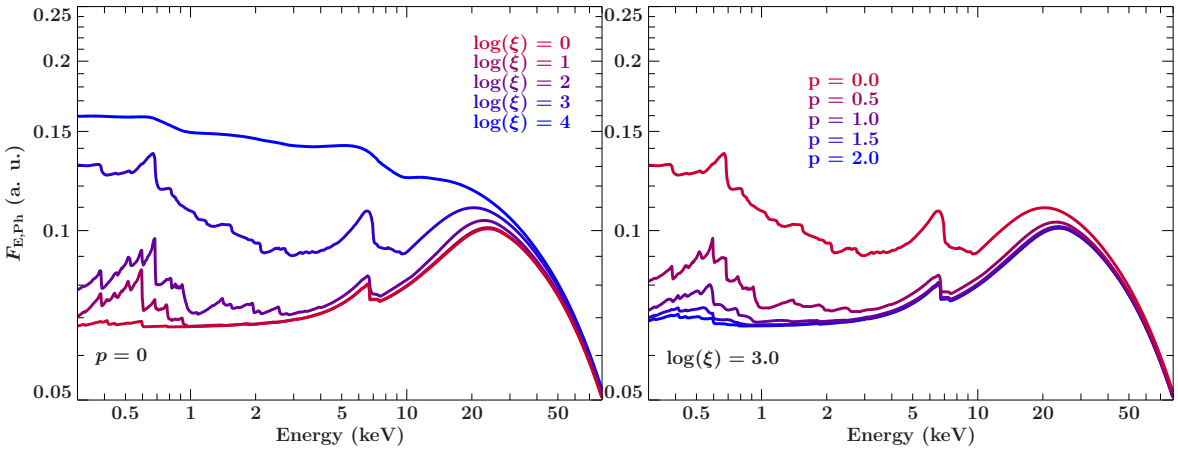

Figure 8.6: *Left:* output spectra of relxilllpCp for different values of the ionisation parameter, which denotes the ionisation at the inner edge. No ionisation gradient was applied. *Right:* output spectra of relxilllpCp for different values of the ionisation gradient index for the powerlaw ionisation gradient. For both, standard parameters with $\Gamma = 2$, $A_{\mathrm{Fe}} = 1$, $\log(N) = 15$ and $kT_{\mathrm{e}} = 60\,\mathrm{keV}$ have been assumed.

flux, which produces strong reflection features. A radially constant ionisation ($p = 0$) has the same effect, because the disk reflects evenly across its radial extend.

Comparing the spectra for different ionisation and gradient indices, it becomes clear that changing those two parameters has a very similar effect on the spectra. Note, however, that an ionisation gradient that is not connected to the irradiation profile is just as unphysical as an ionisation parameter unconnected to both irradiating flux and density. The Alpha model should therefore give more physical solutions than relxilllpCp with or without an ionisation gradient. The fact that the relxilllpCp solution with a powerlaw gradient is very similar to the Alpha solution might be owed to the strong absorption at low energies, as was argued by W21 and can be confirmed by Figure 8.6, since the changes in the spectrum are most extreme below $\sim 3\,\mathrm{keV}$. Nevertheless, the iron line region is also, if less strongly, influenced by both parameters. It is therefore a possibility that $\log(\xi)$ and p are correlated in the relxilllpCp solutions and could cause the model to balance a constant gradient by artificially decreasing the ionisation at the inner disk edge.

Iron line shape for a self-consistent ionisation

Now I want to take a closer look at the shape of the iron line in the 5–10 keV region. The left panel of Figure 8.7 shows the 5–10 keV energy band of residuals and the absorption corrected relxill components, together with the ratio between those components. Below, also the relxill spectra with absorption from an ionised disk wind (xstar) and the distant reflection spectra (xillver) are shown. The relxill model components reveal almost entirely smooth reflection spectra with a minuscule iron line feature, although the Alpha model predicts a slightly larger one at 7 keV with a smaller blue wing. This is also visible in the two bumps in the ratio plot at around 7.5 keV.

Despite these small differences, the residuals in the 5–10 kev range are almost indistinguishable. This is owed to the smaller normalization of the xillver component in the Alpha model fit ($\sim 9.0 \times 10^{-6}$, compared to $\sim 11.7 \times 10^{-6}$ for relxilllpCp), which counteracts the slight excess in flux from the relativistic reflection and might also cause the slightly higher iron abundance ($A_{Fe} = 2.7$–4.5 for relxilllpCp and $A_{Fe} = 4.3$–6.9 for relxilllpAlpha), since the iron

Kα-line from the distant reflection needs to stay constant in flux.

The slightly smaller column density of the absorption component, which denotes the N_{H} of the ionized outflow, might also play a role in the self-consistent ionisation solution, since the two prominent blueshifted absorption lines are located directly at the iron hump at 7 keV. Indeed, the N_{H} of xstar is smaller for relxilllpAlpha ($4.9 \times 10^{22}\, cm^{-2}$) than for relxilllpCp ($6.9 \times 10^{22}\, cm^{-2}$); the error intervals again overlap slightly though. Looking at the absorbed relxill components in Figure 8.7, the larger absorption lines in the case of a self-consistent ionisation manage to align the flux with the spectrum of the constant ionisation model.

The very flat iron line of relxilllpCp could be attributed to the radially constant ionization. Figure 8.5 shows that it differs drastically from all the other gradients. Especially for small radii, which is the region in a compact lamppost geometry where most of the reflection comes from, it underpredicts the ionisation parameter. Comparing the iron lines of the self-consistent model and the model with a powerlaw gradient shows that by allowing for an ionisation gradient, the empirical model also predicts a slightly larger hump comparable to that of relxilllpAlpha (see Figure 8.7, right panel). In this case, no large differences in the distant reflection and absorption components are necessary anymore. The only remaining differences, as seen in the ratio between the relxill components, are slightly different shapes of the blue wing. These probably cause minimal differences in the residuals and lead to a slight improvement of χ^2 for the empirical model ($\Delta\chi^2 = 2$).

Comparing the iron lines of the empirical powerlaw model (Figure 8.7, right panel), and the more physical model implementing an α-disk density gradient (Figure 8.8, left panel), virtually no differences in line shape are visible. This is all the more surprising since the former predicts a much higher ionisation than the latter ($\log(\xi) > 3.9$ and $\log(\xi) = 2.3$–3.3). When comparing the gradients in Figure 8.5, it is clear that the powerlaw gradient falls off much steeper than the α-gradient (so that the ionisation is very weak for larger radii) but predicts a much higher ionisation at the inner edge. The high amounts of absorption at larger radii for the powerlaw gradient due to the low ionisation levels (compare Figure 4.4) might therefore be counteracted by an extremely high ionisation at the innermost radii, where most of the reflection takes place. It also should be remembered that it were exactly those models, which implemented an ionisation gradient and fitted the ionisation level, that required a larger source height. Since this parameter controls the irradiation profile, it has a complex impact on the spectrum. In these cases, it seems to counteract changes in the ionisation parameter. It can therefore be concluded that both, empirical and more physical ionisation and density gradient models, predict a larger source height when the ionisation is a free parameter.

The left panel of Figure 8.8 shows the relxill components for a self-consistent ionisation, assuming a constant density and an α-disk density gradient, respectively. It is apparent that the constant density model exhibits a lack in reflected flux of around 10 % w.r.t the flux of the density gradient model over the depicted energy range. Also, it predicts a slightly sharper absorption edge at 7 keV. Again looking back at Figure 8.5, this might be caused by the smaller ionisation in the intermediate radial range between 2 and 10 r_{g} for the purely irradiation-induced ionisation profile assuming a constant density. For smaller ionization, a larger part of the flux is absorbed and does not reach the observer. To keep the flux of the total spectrum constant, the offset of the relxill component for a constant density is probably counterbalanced by a slightly higher normalization of the scattered flux component nthComp (see the bottom left panel of Figure 8.8).

Previously, I postulated the existence of two kinds of solutions: one is neither reflection nor continuum dominated, the other is heavily reflection dominated. From Figure 8.7 and Figure 8.8, it is evident that the former corresponds to the solutions for a free ionisation, and the latter corresponds to the solutions for a self-consistent ionisation, i.e. the solutions of the

new Alpha model. The overall slightly better fit statistics for the free ionisation solutions indicate that this particular iron line shape plus a larger amount of primary continuum emission, which essentially flattens the iron line, fit the data better than the line shape predicted by self-consistently calculating the ionisation across the disk. The iron line shape resulting from self-consistent ionisation, however, still seems to fit the data well, and requires much less influence of the primary continuum. Therefore one could say that the relxilllp model predicts a smaller reflection fraction, regardless of ionisation or density gradient, when the ionisation stage of the inner disk is allowed to be a free parameter.

Impact of a self-consistent ionisation on other parameters

It remains to compare the solution for a free ionisation, assuming a physical α-disk density gradient, and the solution for a self-consistently calculated ionisation, also assuming an α-gradient, but having the height fixed to the value that was predicted by the other model. Both models take the lamppost irradiation profile and the thin disk density profile into account for properly calculating the ionisation gradient across the disk. Only the latter, however, additionally takes the luminosity of the primary source into account in order to calculate the ionisation level itself. The model which fits the ionisation level neglects the actual luminosity impinging on the disk. By fixing the source heights to the same value, I made sure that the irradiation profiles (and therefore the ionisation profiles) are as similar as possible for both models. They only differ in the absolute value of the ionisation. Like this, I can examine the impact of a self-consistently calculated ionisation on the other parameters.

In the left panel of Figure 8.9, the 5-10 keV energy band for the relxilllp components is plotted, again together with the ratio between the components, the individual residuals, the wind absorbed relativistic reflection components and the distant reflection components. From the ratio, it is evident that the reflection components deviate more than 20 % above 7 keV. The iron line has a much sharper and larger absorption edge for a self-consistent ionisation than for a fitted ionisation. Again, this lack in flux above 7 keV is partly balanced by a larger distant reflection component (the normalization of xillver being $\sim 9.6 \times 10^{-6}$ for relxilllpAlpha and $\sim 6.9 \times 10^{-6}$ for relxilllpCp). Still, the deviations in iron line shape lead to a significantly worse fit ($\Delta\chi^2 = 20$).

Previously, I observed that the predicted ionisation for a lamppost source at this height ($h = 2.8\,r_+$) is larger when calculated self-consistently ($\log(\xi) \sim 3.7$) than when fitted ($\log(\xi) \sim 2.7$), and that the photon index of the primary spectrum is also higher in the latter case ($\Gamma \sim 1.80$, compared to $\Gamma \sim 1.65$). The reason for this is the shape of the Compton hump, which is depicted for both models in the right panel of Figure 8.9. A larger ionisation in the self-consistent case implies a more pronounced Compton hump, since in the high ionisation regime, electron scattering of high energy photons dominates the radiative interaction processes. Since the source height is fixed, the only way left to compensate for this is to increase the photon index, i.e. make the primary spectrum softer, which flattens the Compton hump due to a lack of high energy photons, but leads to a sharper iron absorption edge. The fact that the reflected component is larger in the self-consistent case, while the continuum component is smaller, reinforces my line of reasoning.

In turn, the mechanism forces the scattered emission of the nthComp component, shown in the second panel from below, which also has a slight impact on the shape of the Compton hump, to decrease in flux (the normalisation being $\sim 2.8 \times 10^{-5}$, compared to $\sim 3.4 \times 10^{-5}$). This, however, also influences the spectrum below 1 keV and leads to visibly different residuals, as can be seen in Figure 8.3. It can be concluded that in this case, fitting the ionisation not only underestimates the photon index w.r.t. calculating the ionisation self-consistently, but overestimates the amount of scattered emission, too.

8.3.3 Summary

The main point that can be drawn from my analysis is that, by taking the primary flux into account and calculating the ionisation with it, the validity of the lamppost geometry is confirmed. The similarity between the fits of the older relxilllpCp model and the newer relxilllpAlpha model proves that the lamppost approach works well even with stricter physical assumptions.

At least for a source for which the lamppost geometry, neglecting the primary flux, was already a good fit (like the AGN ESO 033-G002), a self-constently calculated ionisation with an α-disk density gradient prevents correlations between the ionisation gradient index (if a powerlaw ionisation gradient is used) and the ionisation at the inner edge, so that the ionisation is generally found higher. Furthermore, even if an α-disk density gradient is used, a self-consistent ionisation prevents correlations between the ionisation and the primary source height, so that the source height is generally found lower. Regardless of density or ionisation gradient, a self-consistent ionisation generally predicts a higher reflection fraction, probably due to the lower source height and the higher ionisation at the innermost radii. Furthermore, when the source height (and therefore the irradiation profile) is fixed, a self-consistent ionisation predicts a higher photon index, and prevents the photon index and the ionisation to be correlated due to the similar impact on the shape of the Compton hump. Lastly, a self-consistent ionisation prevents correlations between the ionisation and the flux of the distant reflection, since both parameters can be used to control the strength of the iron absorption edge. Also, it prevents correlations between the ionisation and the column density of an absorbing ionised outflow, given that the resulting absorption lines impact the iron line shape.

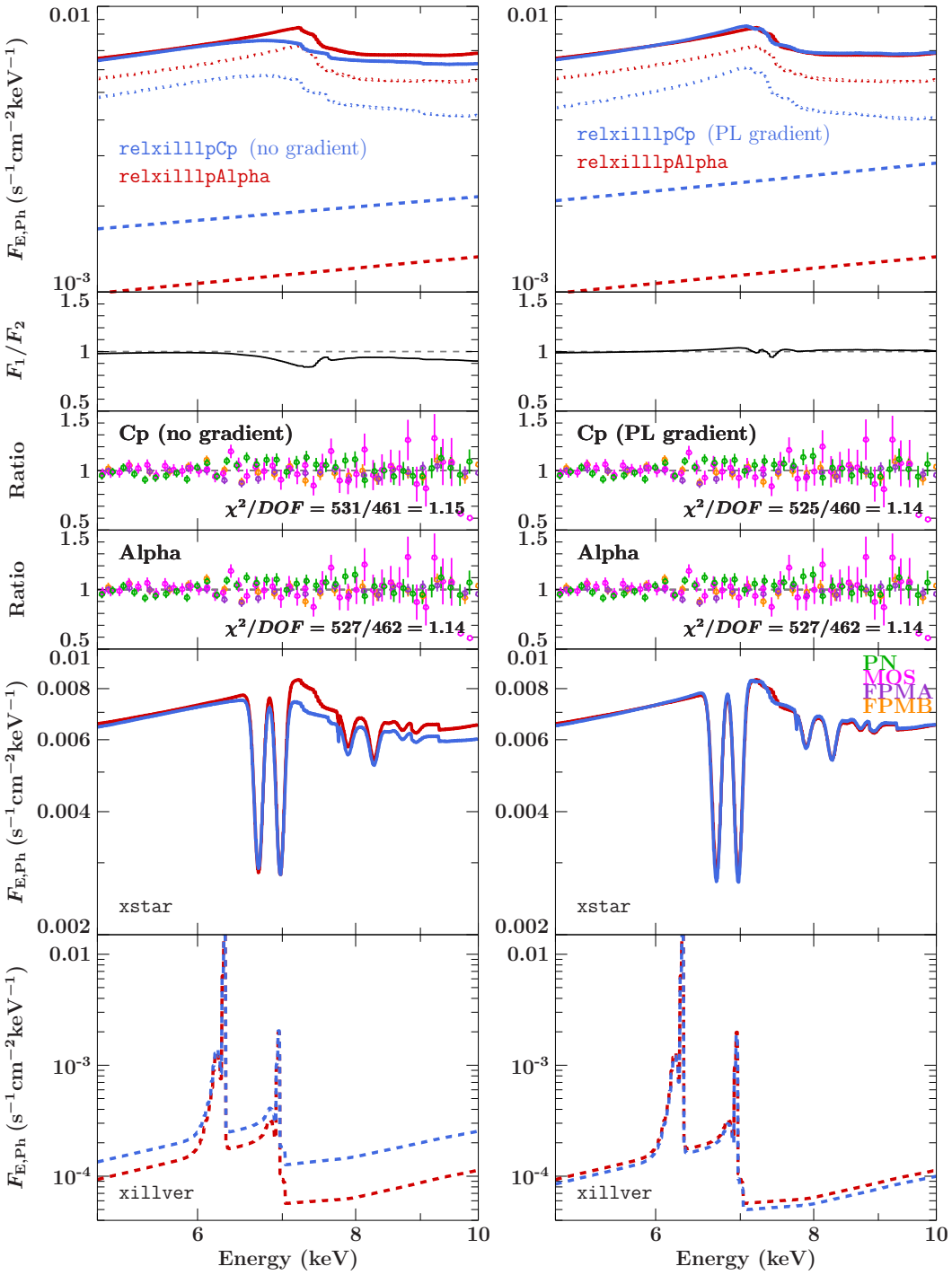

Figure 8.7: *Left:* comparison of the relxilllpCp spectrum for a constant ionisation, and the relxilllpAlpha spectrum in the 5-10 keV range. *Right:* comparison of the relxilllpCp spectrum with a powerlaw ionisation gradient, and the relxilllpAlpha spectrum in the 5-10 keV range. The upper panels show the model output spectra (where the dashed lines indicate the continuum components and the dotted lines the reflected components); the panels below show the ratio between the two total spectra (denoted as M1 and M2, respectively) and the residuals; the two lower panels show the relxilllp spectra absorbed by the xstar components, and the distant reflection components of xillver, respectively.

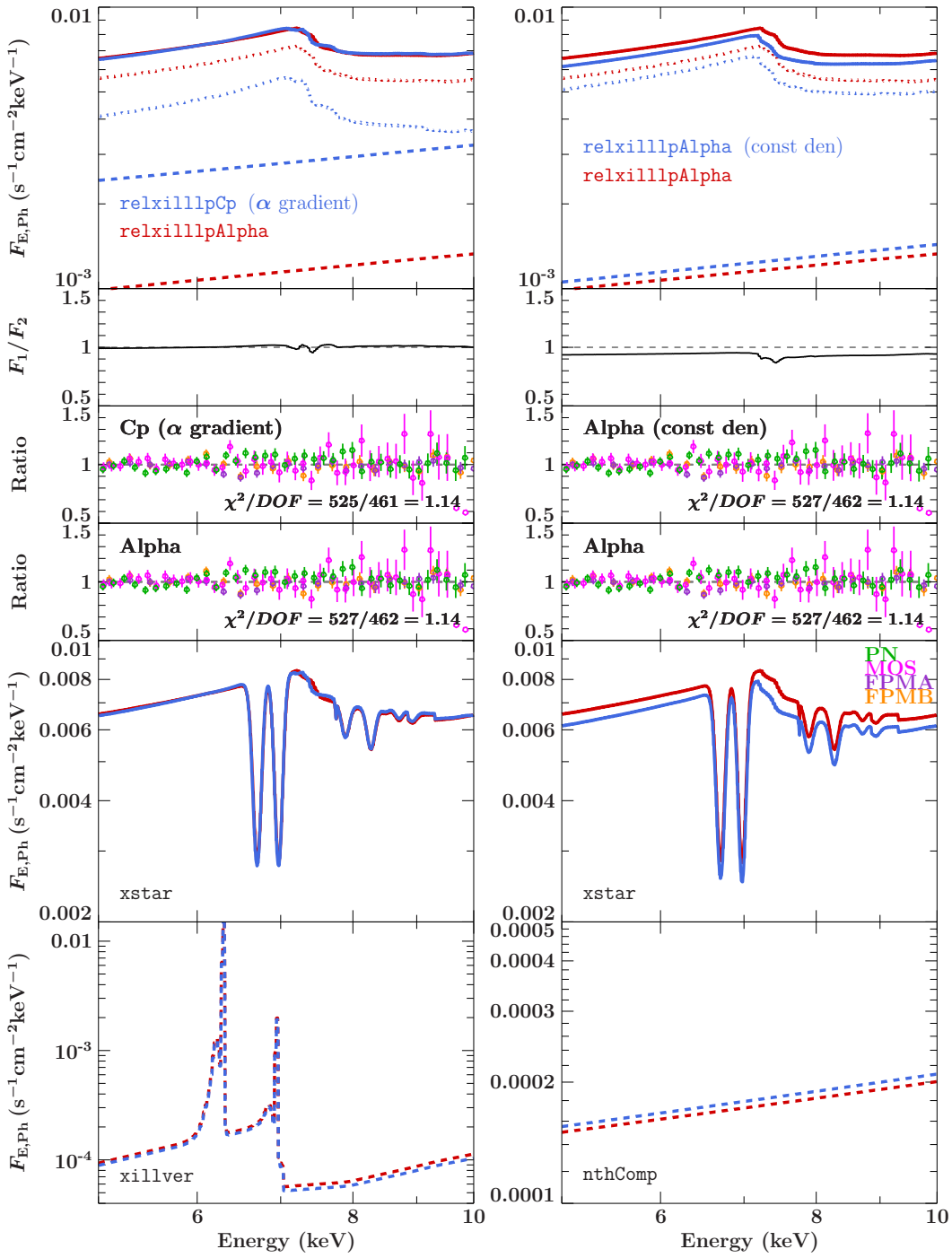

Figure 8.8: *Left:* comparison of the relxilllpCp spectrum assuming an α-disk gradient, and the relxilllpAlpha spectrum in the 5-10 keV range. *Right:* comparison of the relxilllpAlpha spectrum with a constant density, and the relxilllpAlpha spectrum with an α-disk gradient in the 5-10 keV range. The upper panels show the model output spectra (where the dashed lines indicate the continuum components and the dotted lines the reflected components); the panels below show the ratio between the two total spectra (denoted as M1 and M2, respectively) and the residuals; the two lower panels show the relxilllp spectra absorbed by the xstar components, and the distant reflection components of xillver plus the scattered emission of nthComp, respectively.

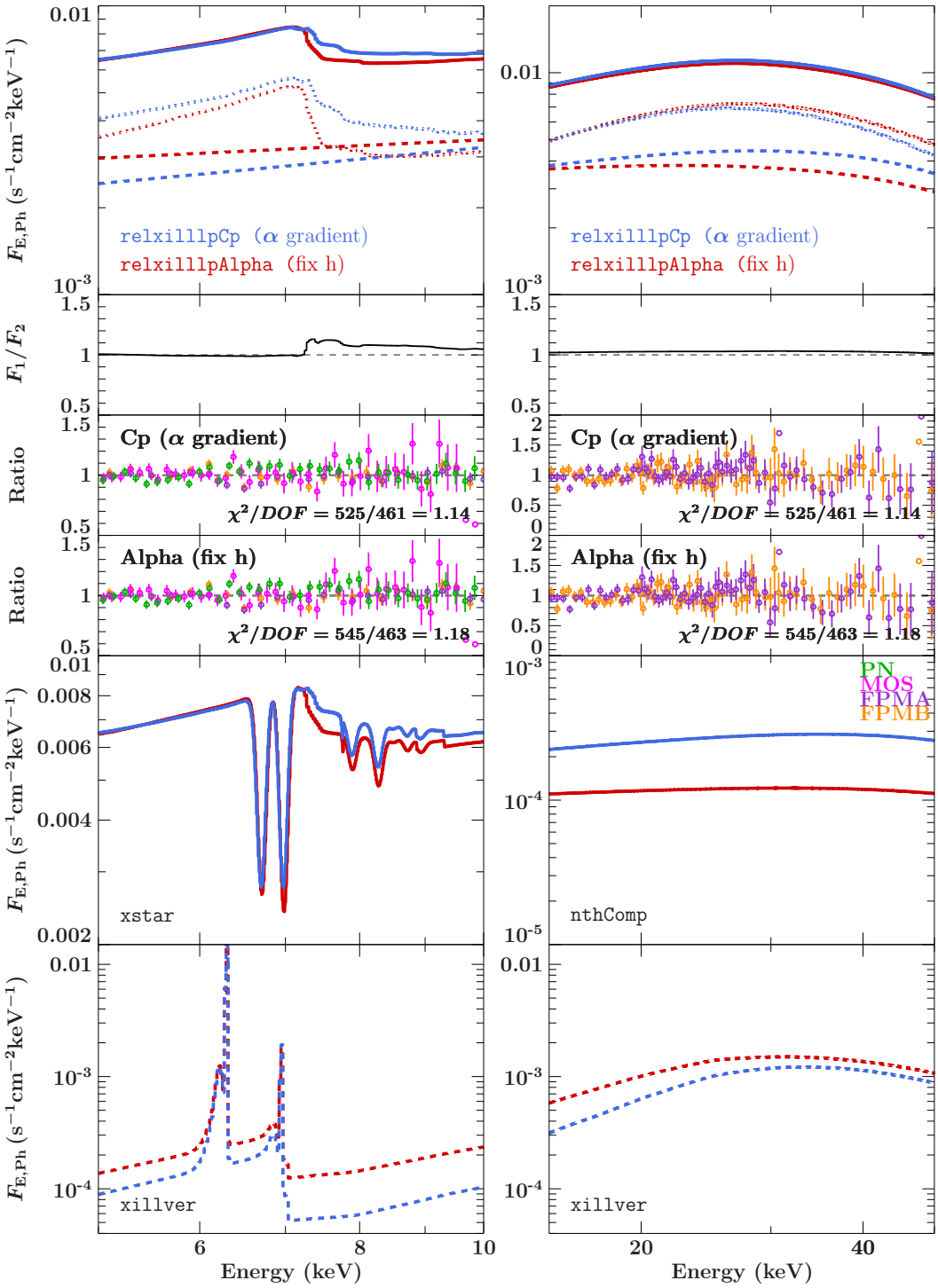

Figure 8.9: *Left:* comparison of the relxilllpCp spectrum assuming an α-disk gradient, and the relxilllpAlpha spectrum in the 5-10 keV range, with the source height fixed to $h = 2.8\,r_+$ in both cases. *Right:* the same spectra in the 10-50 keV range. The upper panels show the model output spectra (where the dashed lines indicate the continuum components and the dotted lines the reflected components); the panels below show the ratio between the two total spectra (denoted as M1 and M2, respectively) and the residuals; the second panels from below show the relxilllp spectra absorbed by the xstar components on the left, and the scattered emission components of nthComp on the right; the bottom panels show the distant reflection components of xillver.

9 Exploring the parameter space with MCMC

In the previous chapter, I showed that the solutions for practically all tested model versions are very similar, in terms of both the best fit parameter ranges and the residual shapes. Furthermore, the parameter space is expected to be complex due to the high complexity of the models that are required by the data. Because the free parameters of relxilllpAlpha impact the spectral shape in a nontrivial way, correlations are inevitable. In order to find those, and to investigate possible secondary solutions in the parameter space, the previously used χ^2-minimization is not particularly useful. In this chapter, I instead introduce a Bayesian data analysis tool based on Monte Carlo sampling, which is able to explore the parameter space more freely.

9.1 Theory

Monte Carlo Methods, according to MacKay (2003), use random numbers to generate samples $\{x^{(r)}\}_{r=1}^{R}$ from a probability distribution $P(x)$, called the *target density*, which is often complex. The difficulty lies in sampling those regions where $P(x)$ is large, without needing to evaluate it everywhere. Additionally, $P(x)$ can often only be assessed within a normalizing constant Z, so that

$$P^*(x) = P(x)/Z. \tag{9.1.1}$$

Z is simply the N-dimensional integration over the whole parameter space of $P^*(x)$,

$$Z = \int \mathrm{d}^N x \, P^*(x). \tag{9.1.2}$$

Since a high-dimensional distribution is also often concentrated in a small region in the state space (the so-called *typical set*), the number of samples needed to hit the typical set at least once is usually very large if a uniform sampling is applied. Another sampling method is e.g. rejection sampling, where a simpler *proposal density* $Q^*(x)$ is defined so that Q is always larger than P when multiplied by some constant c ($\mathrm{c}\, Q^*(x) > P^*(x)\, \forall x$). Subsequently, uniform samples (u) from the interval $[0, \mathrm{c}\, Q^*(x)]$ are generated. A sample is rejected if $u > P^*(x)$ and accepted if $u \leq P^*(x)$. The probability density of all accepted points is then proportional to $P^*(x)$ and poses independent samples of $P(x)$. As a disadvantage, $P^*(x)$ must already be well approximated by $Q^*(x)$, or otherwise too many samples will be rejected.

Markov Chain Monte Carlo (MCMC) processes provide a more elaborate way of sampling a complicated distribution, for which the *Metropolis-Hastings* method is the most commonly used algorithm. It defines a proposal density Q that is not fixed, but depends on the current state x^t, e.g. a Gaussian $Q(x, x^t)$ centered around x^t. The variable $t = 1, ..., \mathrm{T}$ denotes the sequence of dependent samples in the Markov Chain. It is not necessary for Q to be similar to P as it is used to "scan" over P. This method is therefore suitable for high-dimensional problems where finding a similar proposal density is hard. A sample x is accepted if the condition

$$a = \frac{P^*(x)}{P^*(x^t)} \frac{Q(x^t, x)}{Q(x, x^t)} \geq 1 \tag{9.1.3}$$

is fulfilled. Otherwise, the sample is accepted with probability a, so that a trade-off between optimized sampling and random exploration of the state space is achieved. When a gets accepted, it is moved to the next position $x^{(t+1)}$ in the chain; otherwise, the position x^t is kept. Due to the fact that the sampling positions thereby "walk" over the parameter space, they are also called *walkers*. The chosen step size should, on the one hand, be small compared to the length scale of the typical set, since too large steps would likely end up in states with a low probability; on the other hand, too small steps would take an inappropriate amount of computation time. The whole process is similar to rejection sampling, aside from the fact that each sample x^t depends on the previous sample $x^{(t-1)}$. But since an ideal approximation of the target density only contains independent samples, the chain needs to be run until the samples become independent or, in other words, *convergence* has occurred.

Judging whether a chain has converged is mostly not trivial. Tools based on firm theoretical foundation exist as well as empirical diagnostic tools, even though the latter cannot determine convergence with certainty. Several articles, which give an overview for MCMC convergence diagnostics, can be found in the literature (e.g. Roy, 2020).

9.2 Implementation

In this thesis, an MCMC method is used to sample the complicated parameter space of the spectral models which are fitted to the X-ray data of ESO 033-G002. For a possible parameter combination θ of a model H, and a set of data points D, the posterior probability of the paramters, given the data and model, is

$$P(\theta|D,H) = \frac{P(D|\theta,H)\,P(\theta|H)}{P(D|H)} \tag{9.2.1}$$

according to Baye's theorem, where the χ^2 of a fit poses the likelihood $P(D|\theta,H)$ of this particular parameter combination producing the observed data points (given error bars). The prior $P(\theta|H)$ dictates the available parameter space. The evidence $P(D|H)$ is irrelevant for this level of inference, i.e. when only one model is used for fitting. The MCMC process can be used to sample the posterior distribution $P(\theta|D,H)$ as a target function, but is no minimization algorithm. As a result, the solutions of MCMC runs will never indicate the "best fit" of the model for a particular data set, as this is only given by $P(\theta|H)$. Instead, the "most probable fit" is calculated as the maxima of the sampled parameter distributions in the posterior space and at best comes close to the true best fit.

9.2.1 Stretch move algorithm

The MCMC method that was implemented in ISIS by M. A. Nowak is based on an algorithm from Foreman-Mackey et al. (2013, hereafter FM13), which in turn is based on the method of Goodman & Weare (2010, hereafter GW10). I also use this implementation in my thesis. GW10 proposed an algorithm called *stretch-move*, which, instead of updating the walkers one after another, simultaneously evolves an ensemble of K walkers $S = \{X_k\}$. The distribution for one walker k is based on the current position of the complementary ensemble $S_{[k]} = \{X_j, \forall j \neq k\}$. A position thereby refers to a vector in the N-dimensional parameter space. For an update of the walker position X_k, a walker X_j is randomly drawn from $S_{[k]}$, and $X_k(t)$ is updated according to

$$X_k(t) \rightarrow X_k(t+1) = X_j + Z[X_k(t) - X_j]. \tag{9.2.2}$$

The random variable Z is drawn from the distribution $g(z)$, for which GW10 propose

$$g(z) \propto \begin{cases} z^{-1/2} & \text{if } z \in [1/a,\, a] \\ 0 & \text{otherwise} \end{cases} \tag{9.2.3}$$

The parameter a denotes the stretch factor and essentially controls the step size of the stretch move.

FM13 suggested an improved algorithm which allows a part of the stretch move algorithm to be executed in parallel. Therefore, the full ensemble K is split into two subsets $S^{(0)} = \{X_k, \forall k = 1, ..., K/2\}$ and $S^{(1)} = \{X_k, \forall k = K/2+1, ..., K\}$. All updates of walkers in $S^{(0)}$ are based on the positions of the walkers in $S^{(1)}$, and vice versa, and are updated simultaneously. The possibility of parallelizing the stretch move this way makes the algorithm computationally very powerful.

9.2.2 Measure of convergence: autocorrelation time

As a measure of convergence, FM13 introduce the *autocorrelation time* τ. It is based on the autocovariance function of a time series $X(t)$,

$$C_{\mathrm{f}}(T) = \lim_{t\to\infty} \mathrm{cov}[f(X(t+T)), f(X(t))] \tag{9.2.4}$$

which measures the covariance between sample distributions separated by a time lag T. Independence between samples is reached when $C_{\mathrm{f}}(T) \to 0$, i.e. there is no more joint variability between the first state and last state of a chain, or, in other words, the starting conditions no longer influence the later samples. The integrated autocorrelation time

$$\tau_{\mathrm{f}} = \sum_{T=-\infty}^{\infty} \frac{C_{\mathrm{f}}(T)}{C_{\mathrm{f}}(0)} \tag{9.2.5}$$

poses a measure of the number of samples that must be taken in order to ensure convergence. Judged by the length of the autocorrelation time, the stretch move algorithm outperforms standard Metropolis-Hastings-methods by far, exhibiting a much shorter autocorrelation time and therefore being able to save valuable computing power.

9.2.3 Practical handling

Apart from the theory-based measure of autocorrelation time, convergence can also roughly be checked by inspecting the acceptance fraction C_{acc}, which denotes the fraction of walker positions that get accepted as samples for each iteration. The acceptance fraction should not be near the extreme limits. If $C_{\mathrm{acc}} \sim 0$, nearly all steps are rejected, and the chain will fail to draw a representative set of samples from the target density. If $C_{\mathrm{acc}} \sim 1$, almost all steps are accepted, which means that the chain essentially performs a random walk over the parameter space and likewise fails to produce representative samples of the target density. Once C_{acc} no longer exhibits much variability, i.e. the samples get accepted at a steady rate over a large number of iterations, convergence has likely occured. FM13 suggest that C_{acc} ideally lie between 0.2 and 0.5 in this case. If it is too low or too high, it can be manipulated by the parameter a from Equation 9.2.3. Of course, this method cannot judge convergence with certainty and should be regarded as a rule-of-thumb.

The stretch move algorithm only requires two input paramters: the number of walkers and the stretch factor a. Regarding the number of walkers, the larger the better. With twice the number of walkers, the sampling process will yield twice as many independent samples.

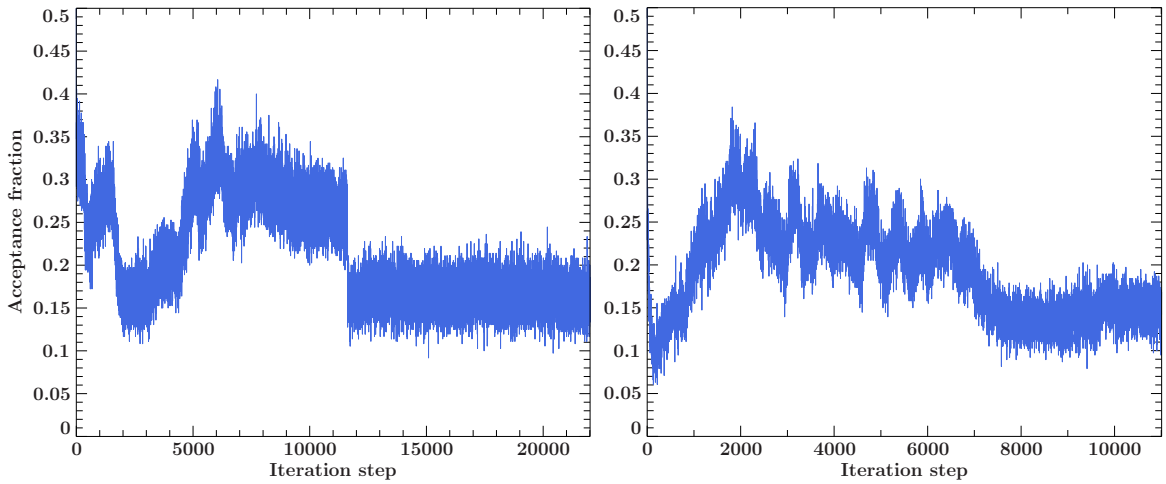

Figure 9.1: *Left:* acceptance fraction over the course of 22×10^3 iterations using relxilllpAlpha with a boost parameter fixed to 1. *Right:* acceptance fraction over the course of 11×10^3 iterations using relxilllpAlpha with a free boost parameter.

At the same time, however, each step will take up twice as much computational time. The number of walkers is therefore limited by the computer power, and too many walkers can lead to performance issues. Apart from that, it should be discussed beforehand which starting distribution the walkers should have (i.e. uniformly spread over the whole parameter space, or a multivariate Gaussian with the mean being the expected best fit). It is also common to define a burn-in time, i.e. the number of steps the walkers need to reach a fairly independent state. These will be rejected in the final chain in order to receive a mostly independent set of samples.

9.3 Results

I ran all MCMC samplings with 20 walkers per parameter and a stretch factor of $a = 1.5$, since this setting proved to be the best in terms of result quality and computational time in previous runs. The starting distribution for the walkers was set to uniform over the whole allowed parameter space, i.e. the walkers were spread evenly (for the exact limits, see the ranges in Table 5.1). This seemed like the best option, since my goal is to explore the parameter space as widely as possible. In the following, I used the same model setup as for the fits from the previous chapter, and relxilllpAlpha as a relativistic reflection component, on the X-ray datasets of ESO 033-G002. I let the MCMC process sample the parameter space of the Alpha model with a boost parameter fixed to 1, i.e. a perfect lamppost geometry, since this proved to fit the data as well as fitting the boost parameter in the previous chapter. I ran the MCMC process a second time with a free boost parameter to test if this is also the case for possible other solutions. For both runs, the coronal velocity was fixed to zero, since this also proved to be necessary in the previous chapter.

In Figure 9.1, the acceptance fraction is plotted over iteration steps, for both the run with boost=1 (left panel) and free boost (right panel). In the first case, the walkers seem to have settled on a steady acceptance rate after 12×10^3 iterations; in the second case, this happened already after 8×10^3 iterations. The first case, however, looks more stable overall. Unfortunately, the average value the acceptance rate settled lies somewhat below 0.2 in both cases. The reason for this, as FM13 suggest, might be that the posterior distribution is multi-modal with narrow modes separated by wide, low probability valleys. This seems to be

the case here and will be elaborated further on. Nevertheless, as running the MCMC for more iterations brought no improvement, decided that an acceptance rate of 0.15 is close enough to convergence. Also, for both cases, the iterations for the most stable range of acceptance rates coincided with the lowest χ^2 fits; therefore cutting the sample distributions above $\chi^2 = 600$ yielded the same result as cutting the burn-in phases of 12×10^3 and 8×10^3 iterations, respectively. In the following, the resulting sample distributions shall be analysed.

9.3.1 Analysis

When two parameters are uncorrelated, their shared 2D-distribution for a large number of fits appears as a 2D-Gaussian. This means that, on average, a change in one parameter does not cause a change in the other. For correlated parameters, this in not the case, and the 2D-distribution appears stretched or warped. If an increase in one parameter is, on average, followed by an increase in the other parameter, they are positively correlated. If instead an increase in one parameter is, on average, followed by a decrease in the other parameter, they are negatively correlated. In order to find out if this is the case for the parameters of relxilllpAlpha, the 2D-distributions for all parameter combinations will be investigated.

Fixed boost parameter

Plots of the sampled one-dimensional and two-dimensional fit parameter distributions for the Alpha model with a boost fixed to 1, so that a perfect lamppost geometry is assumed, can be found in Figure 9.2. The red lines and crosses indicate the most probable parameter combination, and the dashed lines mark the $1\,\sigma$ intervals for the 1D distributions. Only fits with $\chi^2 < 600$ are shown.

From this, it is immediately evident that the MCMC process implies a different solution than the fitting via χ^2-minimization, with a larger source height and much higher iron abundance. However, it is not as good, as the smallest statistic value reached by MCMC is $\chi^2 = 564$, while fitting by hand achieves $\chi^2 = 527$ at best. The most notable feature is the shared distribution between spin and source height: a heavy positive correlation (h is given in negative units) exists, where increasing the spin also increases the height. Another striking feature is the almost flat spin distribution with two small humps at $a \sim 0.4$ and $a = 0.86$. Also, the distribution of the density exhibits a small second peak at $\log(N) \sim 17.5$, in which the solutions do not contain a different distribution of parameters than the ones in the large peak, which has a maximum at $\log(N) = 15.8$. The only parameter that shows significant degeneracy is the inclination: while the main peak is located at $i = 61°$, a smaller second peak is visible around $i \sim 55°$. The tails of the 2D-distributions for the inclination, which otherwise are rather symmetric, show noticeable correlations. Apart from that, the MCMC suggests a significantly larger source height ($h = 5.45\,r_+$) and a higher photon index ($\Gamma = 1.80$). The maximum of the electron temperature is rather low with $kT_\mathrm{e} = 18\,\mathrm{keV}$. The peak of the iron abundance distribution $A_\mathrm{Fe} = 9.3$ is close to the upper limit of $A_\mathrm{Fe} = 10$ solar abundances.

To investigate the second solution for a smaller inclination, the sample distributions for $i < 57°$ are plotted in Figure 9.3. The most drastic change in distribution occurs for the iron abundance. While before it's peak tended to the limit of $A_\mathrm{Fe} = 10$, now the distribution is symmetric around $A_\mathrm{Fe} = 7.3$. Yet, the tail for lower iron abundance still correlates with the higher spin peak $a \sim 0.9$. Significant correlation can also be seen in the 2D-distribution between iron abundance and source height, where a higher abundance corresponds to a lower height. Furthermore, the iron abundance shows some correlation to the photon index (lower A_Fe corresponds to higher Γ) and to the inclination still. This indicates a third kind of solution with $i \sim 55°$, $A_{Fe} \sim 6$ and $a \sim 0.9$.

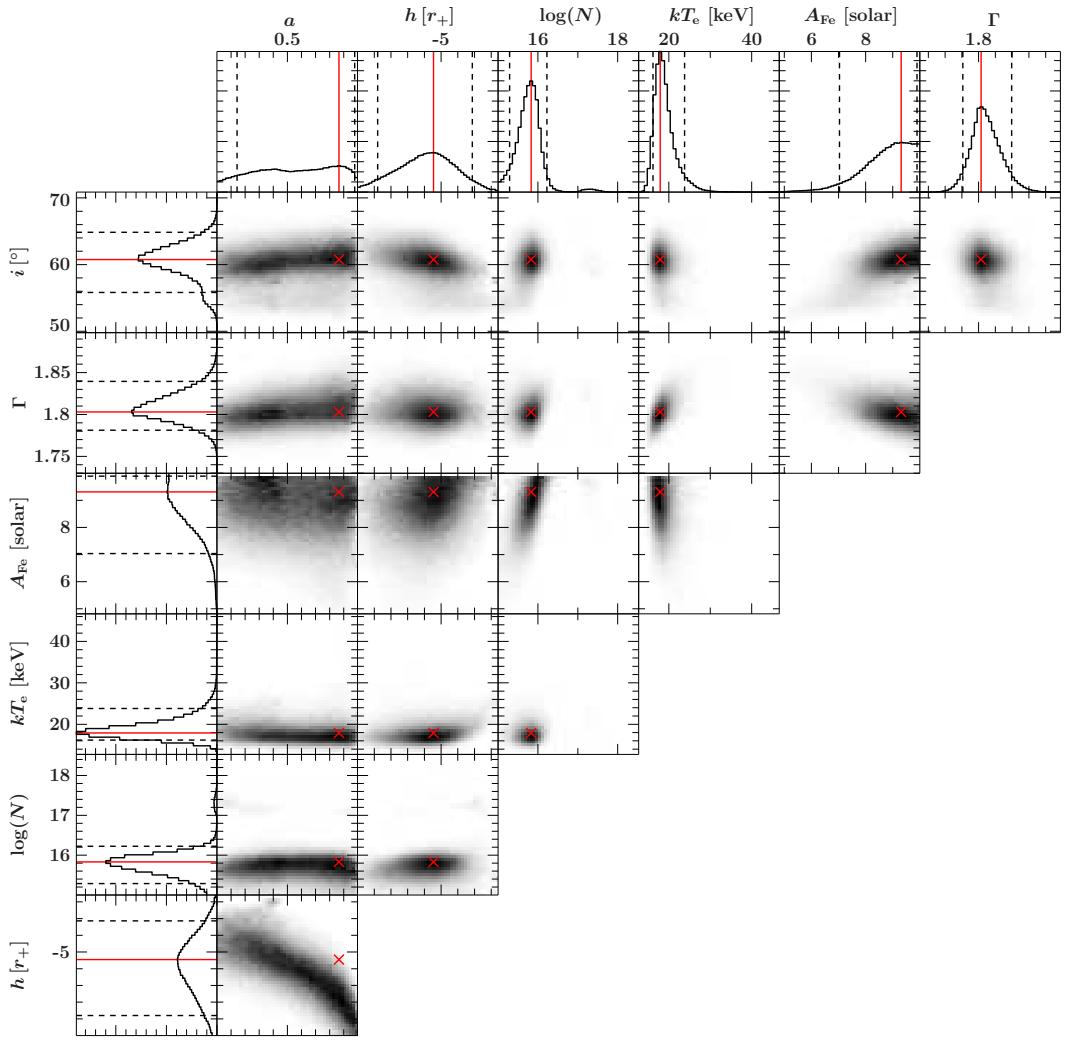

Figure 9.2: 1D and 2D parameter distributions for the Alpha model with boost fixed to 1 and β fixed to zero. Only the best fits with $\chi^2 < 600$ are shown. Red lines and dashed black lines indicate the most probable parameter value and the $1\,\sigma$ intervals for the 1D distributions. Red crosses mark the most probable combinations for the 2D distribution.

Free boost parameter

The 1D and 2D distributions for the MCMC run featuring a free boost parameter are plotted in Figure 9.4. On the first glance, they look very similar to the distributions for a fixed boost. However, the peak of the density distribution is now slightly higher with $\log(N) = 16$, and no second peak is seen. Other slight differences appear in the height distribution peaking at $h = 6.67\,\mathrm{r_+}$ rather than $h = 5.5\,\mathrm{r_+}$, and the photon distribution peaking at $\Gamma = 1.82$ rather than $\Gamma = 1.80$. The distributions of iron abundance and electron temperature are similar to the ones for a fixed boost parameter. It is also notable that the inclination distribution shows no major degeneracy anymore; the second peak in the distribution for a fixed boost is barely visible as a long tail towards lower inclinations in the distribution for a free boost. The boost parameter itself peaks at $boost = 1.2$, but converges to $boost \sim 1$ for increasing spin. Lastly, the strong correlation between spin and height is still clearly visible. The spin distribution, although still flat, shows no peaks anymore and even flattens further towards higher values,

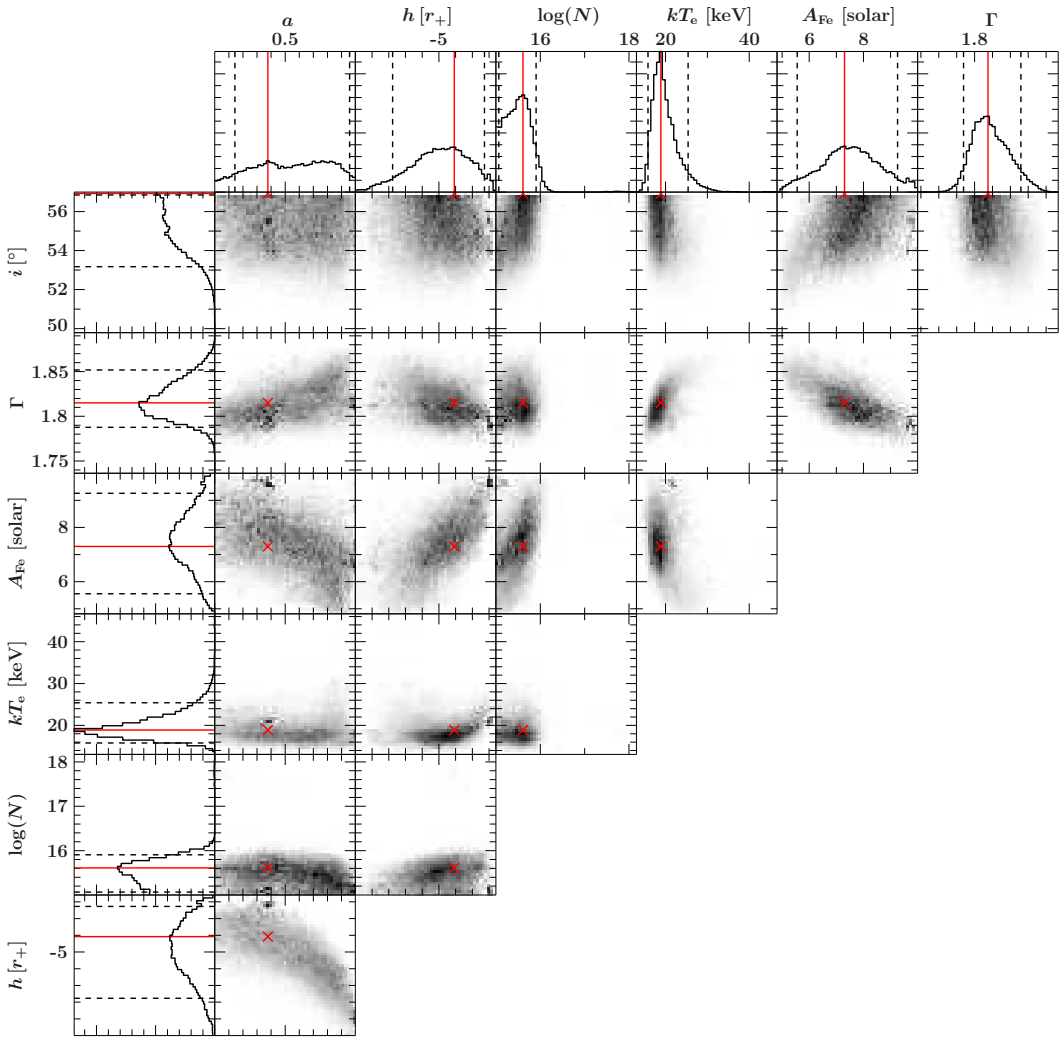

Figure 9.3: 1D and 2D parameter distributions for the Alpha model with boost fixed to 1 and β fixed to zero. Only the best fits with $\chi^2 < 600$ are shown, and the inclination distribution was cut so that $i < 57°$. Red lines and dashed black lines indicate the most probable parameter value and the $1\,\sigma$ intervals for the 1D distributions. Red crosses mark the most probable combinations for the 2D distribution.

seemingly excluding maximally spinning solutions. Other correlations are especially apparent in inclination against height (negative) and inclination against boost (positive); also the density is slightly positively correlated with all parameters except electron temperature and source height.

9.3.2 Discussion

By analysing the 2D-distributions of the sampled parameter combinations, I observed many correlations and non-Gaussian distributions. The main solution found by the MCMC run is distinctly different than the solution I found via χ^2-minimization, with a larger source height, iron abundance, photon index and inclination. For a boost parameter fixed to 1, especially the inclination revealed a secondary solution for lower inclination and lower iron abundance. The MCMC run for a free boost parameter found a very similar solution to the solution with a fixed boost, however with much less samples inside the secondary solution.

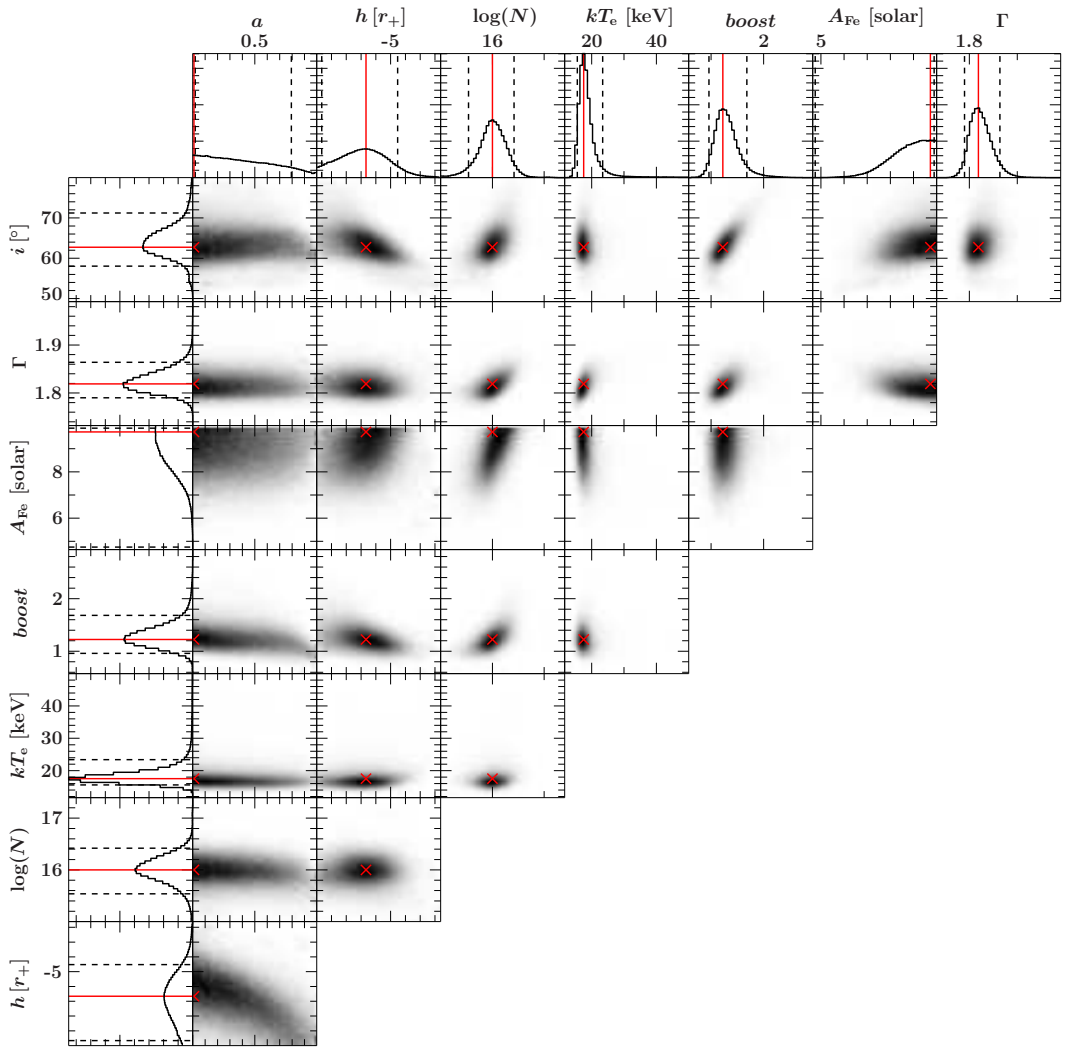

Figure 9.4: 1D and 2D parameter distributions for the Alpha model with a free boost parameter and β fixed to zero. Only the best fits with $\chi^2 < 600$ are shown. Red lines and dashed black lines indicate the most probable parameter value and the 1 σ intervals for the 1D distributions. Red crosses mark the most probable combinations for the 2D distribution.

Nevertheless, the similarity between the solutions for a fixed and free boost parameter again, like in the previous chapter, stresses the consistency of the data with the lamppost geometry, since for a fixed boost, the reflection fraction is calculated self-consistently for a lamppost point source.

Height-spin correlation

The dominating correlation in the parameter space seems to be the positive height-spin correlation. Since for a higher spin, the inner disk edge draws closer to the black hole, and the area for which strong lightbending is important becomes larger, the reflection fraction increases. To keep it constant, the source height subsequently increases, since it controls the strength of reflection by moving closer to or away from the black hole. This way, the total spectrum is always continuum dominated, since more primary flux reaches the observer for a large source height.

The benefit in χ^2 for increasing the height seems to be so large that the solutions for high spin and low height, which I found by χ^2-minimization by hand in the previous chapter, are never found. These solutions seem to exist in a narrow trench in the χ^2 landscape, as increasing the height by $0.01\,r_+$ results in a fit statistic growth of $\Delta\chi^2 = 97$, and further increasing it by the same amount two times more results in $\Delta\chi^2 = 366$ and $\Delta\chi^2 = 938$, respectively. For small changes in other parameters, the increase in χ^2 is not so extreme.

For a large source height, approximately half of the emission reaches the observer without reflecting on the disk. To counterbalance the resulting dominance of the continuum in the total spectrum and strengthen the iron line, the iron abundance runs against its upper limit of $A_{\mathrm{Fe}} = 10$.

Impact of a self-consistent ionisation

The reason why especially the inclination is so strongly degenerate might be connected to the ionisation in the Alpha model. It was established in chapter chapter 5 that varying the viewing angle lets different layers of the disk become visible due to the change in effective optical depth. Since the incidence angle of the irradiating photons changes over the radial range of the disk due to lightbending, the photons reach different depths and thereby create an ionisation structure that varies for each layer. Additionally, heavy elements, like iron, are more abundant at larger depths and therefore create stronger emission lines for steep incidence angles.

As the absolute value of the ionisation is calculated self-consistently in the Alpha model, it can no longer be adjusted so that it matches different layers when varying the viewing angle. The Alpha model, although more physical than previous models due to the α-disk density gradient and the self-consistent ionisation, is still a simplification and will never describe a real system completely. If therefore the overall ionisation level and structure implied by the models fit the data less well for a different viewing angle, other parameters will change. For $i < 60°$, this seems to be the case since especially the iron abundance, which controls the strength of the iron line, appears to be correlated with many other parameters in the secondary solution and thereby implies a tertiary solution, corresponding to a deeper layer in the disk. A lower iron abundance, which correlates with high spin, high photon index, large source height and low inclination, counterbalances the naturally stronger emission of iron in the deeper layer, for which the calculated ionisation level does not seem to account.

In the top and middle panel of Figure 9.5, I plotted the relxilllpAlpha components in the iron line region from 2-10 keV with their continuum components and reflected components, for the solutions with $i \sim 60°$ (S1) and $i \sim 55°$ (S2). Fitting these solutions again by hand yielded similar statistic values, $\chi^2 = 546$ for the former and $\chi^2 = 548$ for the latter. Still, the fits are not as good as the one found in the previous chapter, which is shown in the third main panel of Figure 9.5. For convenience, I call this solution Sα. It is obvious that the two kinds of solutions are completely different, since one is continuum dominated, while the other is reflection dominated. This strengthens the argument that the MCMC fit seems to be "stuck" in the solution with a large source height.

The parameters of the refitted solutions found by MCMC also coincide well with their sampled distributions: for S1, the relevant parameters are $i = 62°$, $h = 7.2\,r_+$, and $A_{\mathrm{Fe}} = 8.4$; for S2, it is $i = 54°$, $h = 5.0\,r_+$, and $A_{\mathrm{Fe}} = 6.0$. These solutions again indicate different layers of the accretion disk. The ionisation at $(11/9)\,r_{\mathrm{in}}$ is $\log(\xi) = 0.6$ for S1, and $\log(\xi) = 1.1$ for S2. Indeed, the two solutions predict a (if slightly) different ionisation, which is in line with the point made above.

Below the model components in Figure 9.5, the ratios of S2 divided by S1, and Sα divided by S1 are shown. In the first case, the difference between the solutions is mostly evident

in the shape of the iron edge around 7 keV. The sharper line of the secondary solution fits the data less well, as the residuals show slightly larger deviations around 7 keV than for the primary solution. However, the higher ionisation strengthens the Compton hump more, as is evident is a slight deviation from unity above 30 keV. This trade-off could be one of the reasons for the degeneracy in the viewing angle distribution. The ratio between the primary MCMC solution and the solution by hand also serves as evidence for the trade-off scenario: compared to the S2/S1 ratio, the iron line shapes are more similar, but the Compton hump is approximately 20 % larger for the MCMC solution S1. Since Sα fits the data much better than S1 ($\Delta\chi^2 = 19$), the slightly smaller Compton hump of S2 is probably the feature that sets the solution apart from S1, even though their χ^2 statistics are almost equal.

Role of the boost parameter

At first, it may be surprising that the boost parameter stays close to 1 throughout the sampling process when it is left free, while the boost in the solutions from the previous chapter was often unconstrained in the 90 % error intervals within the limits of 0 to 10. This, however, is easily explained by the large source height. Previously, the spectrum of the Alpha model was extremely reflection dominated due to the low source height, and it did not matter if the strength of the continuum was decreased even more by increasing the boost. Here, the total spectrum is even continuum dominated (see Figure 9.5), and varying the strength of the reflection component w.r.t. the continuum component greatly influences the total spectral shape. This explains the rather narrow distribution of the boost parameter. Also, the fact that the boost parameter stays close to 1 proves that for the solution found by the MCMC process, too, the reflection fraction implied by the lamppost geometry fits the data well.

Secondly, the reason why the inclination distribution for a free boost parameter shows no strong correlations anymore could be the variability of the boost parameter itself. As increasing the boost means increasing the fraction of reflection in the total spectrum and therefore strengthening the reflection features, discrepancies with the data, which are caused by the self-consistently calculated ionisation for different viewing angles, may be counterbalanced in this way. The fit is thereby prevented from slipping into a second solution with a different parameter combination in order to match the ionisation level of a deeper layer in the disk.

The correlations, which appear stronger than in the distributions for a fixed boost, indicate that the parameters overall form a tighter system in which small changes in one parameter can be counterbalanced by equally small changes in a set of others. This is especially apparent in the positive correlation between boost and inclination, which shows that a steeper viewing angle, while obscuring deeper disk layers, causes an increase in reflection strength. Due to the lower abundance of iron in the upper disk layers, the iron line is strengthened by increasing the boost. This seems to be better in terms of fit statistic than increasing the iron abundance itself, as this parameter is not correlated with the boost. The slight positive correlation between boost and source height reflects the correlation between spin and source height, since the boost parameter controls the strength of the reflected component similarly to the spin.

Supersolar iron abundance

For both, a fixed and a free boost parameter, the density is positively correlated with the iron abundance. This hints at the connection between density and iron abundance mentioned in section 5.2, and the overall problem of supersolar iron abundances. Implementing a high density model can lead to a different fit that mitigates the need for a large iron abundance by better describing the flux at soft energies (Tomsick et al., 2018). However, this cannot be the case for ESO 033-G002, since the reflected flux is completely absorbed in this regime.

While the iron abundance found by W21 of $A_{\mathrm{Fe}} = 3.5$–4.5 solar abundances, which was confirmed by the new model which takes the primary flux into account, is already supersolar, the abundance found by the MCMC process gives $A_{\mathrm{Fe}} = 6$–10 and is therefore very likely unphysical. This was also found in other sources (see subsection 5.2.6) and is an unsolved problem still. In my case, however, it can easily be attributed to the large source height, as mentioned before. This proves that the relxilllpAlpha model is capable of producing solutions with extremely high iron abundances, which could be a point for improvement in the future.

9.3.3 Summary

Sampling the parameter space with an MCMC process has not brought more insight into the solutions found by χ^2-minimization, but has revealed a second kind of solution. However, due to the extremely high iron abundance and the larger χ^2 statistics, it is very likely unphysical. The reason why the walkers seem to be trapped in this solution is, on the one hand, the strong correlation between spin and source height, which leads to a large source height estimate and a broad spin distribution. On the other hand, it could be caused by the fact that the low height solution found by χ^2 fitting is located inside a narrow trench in the parameter space, which is unlikely found by the walkers.

Nevertheless, analysing the MCMC results has brought more insight into the internal mechanisms of the relxilllpAlpha model, which calculates the ionisation of the disk self-consistently. The fact that the self-consistent ionisation, when varying the disk inclination w. r. t. the observer's plane, does not describe every layer of the disk equally well, might cause a degeneracy in the inclination distribution, thereby creating two or more separate solutions. Each of them adjusts the other parameters so that the ionisation for the individual disk layer fits the data better. This also gives rise to some correlations between the parameters. However, by allowing the boost parameter to be fitted (and thereby allowing for deviations from the lamppost geometry), this degeneracy can be mitigated.

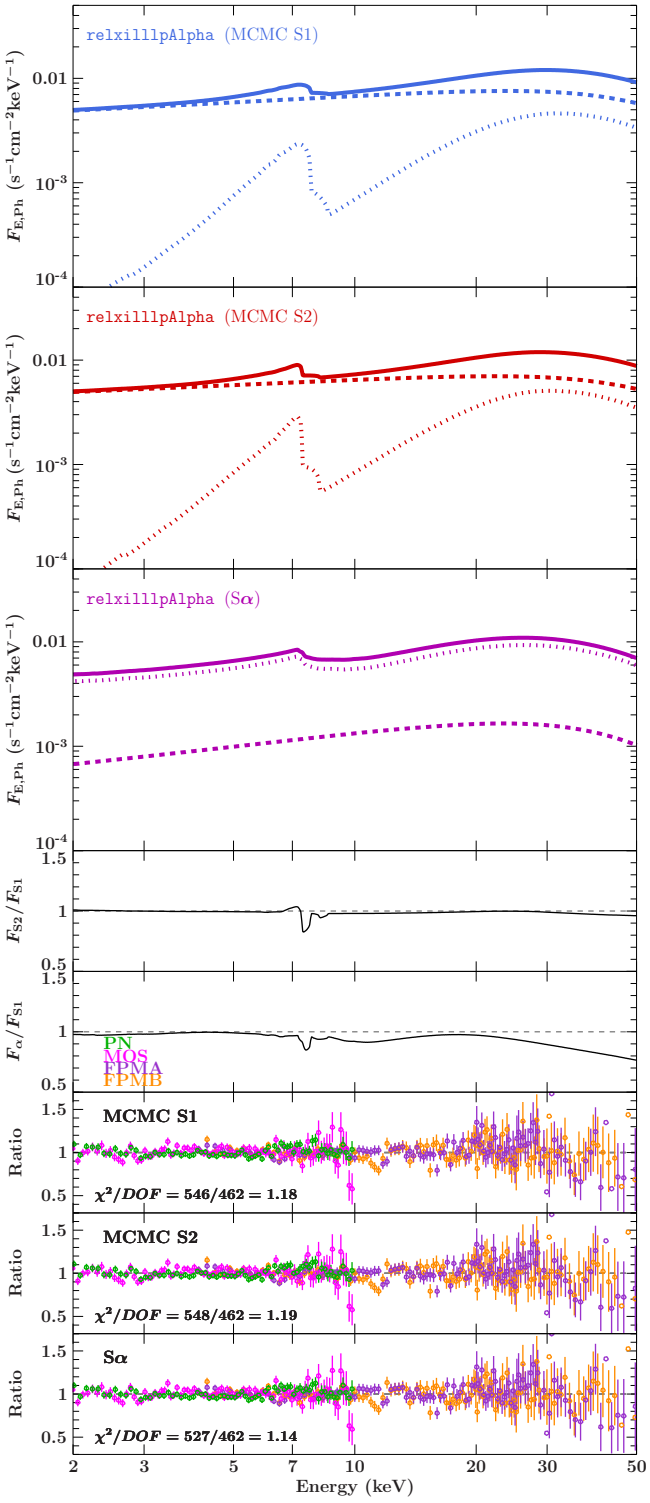

Figure 9.5: RelxilllpAlpha components for the 2–50 keV energy regime of the MCMC solutions S1 (for $i \sim 60°$, in blue) and S2 (for $i \sim 55°$, in magenta) that were favored by the MCMC sampling. In magenta, the relxilllpAlpha solution Sα found by χ^2-fitting is shown. Dashed lines indicate the continuum components, dotted lines the reflected components, and solid lines the full spectra. Below, the ratios of S2/S1 and Sα/S1 are shown, as well as the residuals of the individual fits.

10 Conclusion & Outlook

In this thesis, I first covered the basics of general relativity, radiative transfer in matter, the physics, components and evolution of accreting supermassive black holes, and the history and tools of relativistic reflection modeling. Building on the introductory chapters, I tested five different versions of the relxilllp model, including the new version which takes the primary flux of the X-ray source into account, and further explored the parameter space with an MCMC process.

In the light of the outcomes, it can be said that testing the lamppost geometry on stricter physical assumptions by taking the primary flux into account and self-consistently calculating the ionisation for each radius has been successful. By using the new relxilllpAlpha model, I was able to recreate the best fit parameters of the Seyfert-II-galaxy ESO 033-G002 found by W21, who used the relxilllpCp model which neglected the primary flux and included the ionisation as free parameter. At least for this particular source, which already produced a consistent fit for the lamppost geometry when the flux was neglected, the validity of the lamppost geometry was fortified. This means that spin estimates undertaken in the lamppost geometry win additional impact, and contribute to refining the measurement of the spin distribution of black holes across the universe, from which the research on galactic evolution can benefit.

Moreover, I could identify correlations between the free ionisation parameter and other parameters, which are prevented by calculating the ionisation self-consistently. Particularly, it prevents correlations with the ionisation gradient index when an empirical powerlaw ionisation gradient is assumed; with the source height when the ionisation gradient is calculated using an α-disk density gradient; and with the primary photon index when the source height is fixed. Overall, the new model tends to predict a higher ionisation for the inner radii, a lower source height, and a higher reflection fraction. Also, a self-consistent ionisation prevents the flux of a distant reflection component and the column density of an ionized absorber to counteract incongruities in the spectrum caused by neglecting the primary flux. However, I found an additional source of parameter correlations by exploring the parameter space with an MCMC sampler: the self-consistent ionisation led to multiple solutions for the disk inclination parameter, in which the model adapts the other parameters to match the change in ionisation when different disk layers become visible. This can be mitigated when deviations from the lamppost geometry are allowed.

I also found that the new model, which takes the primary flux into account, does not help to solve the problem of supersolar iron abundances seen in many AGN. Both, the old and the new model, find an equally high iron abundance for ESO 033-G002. The MCMC solutions have furthermore shown that the new model is capable of finding solutions with an extremely high, unphysical iron abundance. In the future, this could be a starting point for improvement.

In order to further test the solutions I found for relxilllpAlpha by χ^2-minimization, one could undertake MCMC runs which do not have the walkers being uniformly distributed over the whole parameter space in the beginning, but implement Gaussian starting distributions around the previous best fit values. Like this, the same solution might be found by the MCMC process. Also, the model should be tested on more AGN sources which show evidence for a compact, lamppost-like accretion geometry. A possible candidate is, for example, the type-I Seyfert galaxy IRAS 09149-6206 (Walton et al., 2020). According to the authors,

it shows evidence for a compact accretion geometry with a low lamppost source height ($h = 3.6^{+1.2}_{-0.5}\, r_\mathrm{g}$) and a near maximally spinning central black hole ($a = 0.94^{+0.02}_{-0.06}$). The low ionisation parameter ($\log(\xi) = 1.9 \pm 0.2$) and near constant ionisation gradient ($p = 0.10^{+0.23}_{-0.05}$) indicate that a fit, which takes the primary flux into account, might find a higher ionisation, as was demonstrated in my thesis. Another well suited candidate could be the type-I Seyfert galaxy IRAS 13224-3809 (Jiang et al., 2018) with a rapidly spinning black hole ($a > 0.94$). It is especially promising for testing the new model with an ionisation gradient, since with a constant, fitted ionisation model, two reflection components with different ionisation paramters ($\log(\xi) = 3.13^{+0.07}_{-0.04}$ for $r < 5.8\, r_\mathrm{g}$, $\log(\xi) = 1.48^{+0.14}_{-0.10}$ otherwise) were needed by the authors to describe the data sufficiently. This might imply the existence of a steep ionisation gradient.

Only taking the primary flux of a point source lamppost into account, however, still does not guarantee a sufficiently physical treatment of the underlying source geometry. A real lamppost source, e.g. the base of an aborted jet, will necessarily be extended in both the longitudinal and radial dimension. Dauser et al. (2013) already showed that a source elongated along the spin axis produces reflection features similar to a point source at an effective height, which leads to a problem for the estimate of the spin: for a sufficiently elongated source, both low and high spin parameters produce narrow reflection features. Fitting a broad line reflection model will therefore lead to low spin values, regardless of the actual spin. Another possibility would be to allow for a radial source extend (Wilkins et al., 2016), which directly influences the emissivity profile and therefore the reflection spectrum (Wilkins & Fabian, 2012). The implementation of such a geometry in `RELXILL` is currently a work in progress.

In my analysis, I found that allowing for too many fit parameters, for example a coronal velocity on top of the standard parameters, exceeded the predictive potential of the data sets measured by XMM-Newton and nuSTAR. The proposed *High Energy X-ray Probe* (HEX-P) mission (Kammoun et al., 2023) will combine high spatial resolution X-ray imaging and broad spectral coverage (0.2–80 keV) with a sensitivity superior to current facilities like nuSTAR, which served as the primary data source for determining the coronal temperature E_cut in previous years, and will provide a higher diagnostic potential. With the help of reverberation time lag measurements, the broad bandpass of HEX-P will enable reflection spectroscopy methods to probe the location, geometry and motion of X-ray emitting coronae above black holes. The new flavor of the `RELXILL` reflection model, which takes the flux of the lamppost source into account, can help to utilize the new data for shedding more light onto the coronal geometry and the process of its formation and evolution.

11 Bibliography

Abbasian Motlagh M., Rastegarzadeh G., 2020, Ir. Astron. J. 7, 77

Abramowicz M.A., Chen X., Kato S., et al., 1995, ApJL 438, L37

Antonucci R.R.J., Miller J.S., 1985, ApJ 297, 621

Bambi C., Brenneman L.W., Dauser T., et al., 2021, SSRv 217, 65

Bardeen J.M., 1970, Nature 226, 64

Bautista M.A., Kallman T.R., 2001, ApJS 134, 139

Beckmann R.S., Dubois Y., Volonteri M., et al., 2023, MNRAS 523, 5610

Blandford R.D., Payne D.G., 1982, MNRAS 199, 883

Boyer R.H., Lindquist R.W., 1967, J. Math. Phys. 8, 265

Brenneman L.W., Reynolds C.S., 2006, ApJ 652, 1028

Brenneman L.W., Reynolds C.S., Nowak M.A., et al., 2011, ApJ 736, 103

Christensen F.E., Jakobsen A.C., Brejnholt N.F., et al., 2011, In: O'Dell S.L., Pareschi G. (eds.) Proc. SPIE., Vol. 8147., San Diego, California, p. 81470U

Cunningham C., 1976, ApJ 208, 534

Cunningham C.T., 1975, ApJ 202, 788

Dauser T., 2010, Diploma thesis, Dr. Karl Remeis Sternwarte Bamberg, FAU Erlangen-Nürnberg, Bamberg, Germany

Dauser T., 2014, PhD thesis, Dr. Karl Remeis Sternwarte Bamberg, FAU Erlangen-Nürnberg, Bamberg, Germany

Dauser T., Garcia J., Wilms J., et al., 2013, MNRAS 430, 1694

Dauser T., García J.A., Joyce A., et al., 2022, MNRAS 514, 3965

Dauser T., Wilms J., Reynolds C.S., Brenneman L.W., 2010, MNRAS 409, 1534

den Herder J.W., Brinkman A.C., Kahn S.M., et al., 2001, A&A 365, L7

Dobrotka A., Ness J.U., Nucita A.A., Melicherčík M., 2023, A&A 674, A188

Dotti M., Colpi M., Pallini S., et al., 2013, ApJ 762, 68

Dovčiak M., Done C., 2016, Astron. Nachr. 337, 441

Dovčiak M., Karas V., Yaqoob T., 2004, ApJS 153, 205

Dubois Y., Volonteri M., Silk J., 2014, MNRAS 440, 1590

Einstein A., 1905, Ann. Phys. (Leipzig) 322, 891

Einstein A., 1915a, Sitzungsberichte der Königlichen Preussischen Akademie der Wissenschaften 844–847

Einstein A., 1915b, Sitzungsberichte der Königlichen Preussischen Akademie der Wissenschaften 831–839

Fabian A.C., Lohfink A., Kara E., et al., 2015, MNRAS 451, 4375

Fabian A.C., Rees M.J., Stella L., White N.E., 1989, MNRAS 238, 729

Fabian A.C., Zoghbi A., Ross R.R., et al., 2009, Nature 459, 540

Farah A.M., Edelman B., Zevin M., et al., 2023, ApJ 955, 107

Fiore F., Feruglio C., Shankar F., et al., 2017, A&A 601, A143

Foreman-Mackey D., Conley A., Meierjurgen Farr W., et al., 2013, emcee: The MCMC Hammer, Astrophysics Source Code Library, record ascl:1303.002

Fürst F., Nowak M.A., Tomsick J.A., et al., 2015, ApJ 808, 122

García J., Dauser T., Lohfink A., et al., 2014, ApJ 782, 76

García J., Dauser T., Reynolds C.S., et al., 2013, ApJ 768, 146

García J., Kallman T.R., 2010, ApJ 718, 695

García J., Kallman T.R., Mushotzky R.F., 2011, ApJ 731, 131

García J.A., Fabian A.C., Kallman T.R., et al., 2016, MNRAS 462, 751

García J.A., Kallman T.R., Bautista M., et al., 2018, In: Workshop on Astrophysical Opacities, Vol. 515. Astronomical Society of the Pacific Conference Series, p. 282

Genzel R., Eisenhauer F., Gillessen S., 2010, Rev. Mod. Phys. 82, 3121

Ghisellini G., Haardt F., Matt G., 2004, A&A 413, 535

Giacconi R., Gursky H., Paolini F.R., Rossi B.B., 1962, Phys. Rev. Lett. 9, 439

Goodman J., Weare J., 2010, Communications in Applied Mathematics and Computational Science 5, 65

Haardt F., Maraschi L., 1991, ApJL 380, L51

Harrison F.A., Boggs S., Christensen F., et al., 2010, In: Arnaud M., Murray S.S., Takahashi T. (eds.) Proc. SPIE., Vol. 7732. Space Telescopes and Instrumentation 2010: Ultraviolet to Gamma Ray, San Diego, California, p. 77320S

Harrison F.A., Craig W.W., Christensen F.E., et al., 2013, ApJ 770, 103

HI4PI Collaboration 2016, A&A 594, A116

Hofmann F., Barausse E., Rezzolla L., 2016, ApJL 825, L19

Houck J.C., Denicola L.A., 2000, In: Manset N., Veillet C., Crabtree D. (eds.) Astronomical Data Analysis Software and Systems IX, Vol. 216. Astronomical Society of the Pacific Conference Series, p. 591

Ingram A., Mastroserio G., Dauser T., et al., 2019, MNRAS 488, 324

Iwasawa K., Norman C., Gilli R., et al., 2023, A&A 674, A77

Jansen F., Lumb D., Altieri B., et al., 2001, A&A 365, L1

Jiang J., Parker M.L., Fabian A.C., et al., 2018, MNRAS 477, 3711

Kaastra J.S., Bleeker J.A.M., 2016, A&A 587, A151

Kaastra J.S., Kriss G.A., Cappi M., et al., 2014, Science 345, 64

Kaastra J.S., Mewe R., 1993, A&AS 97, 443

Kallman T., Bautista M., 2001, ApJS 133, 221

Kammoun E., Lohfink A.M., Masterson M., et al., 2023, arXiv e-prints arXiv:2311.04679

Kawanaka N., Mineshige S., 2023, arXiv e-prints arXiv:2304.07463

Koss M., Trakhtenbrot B., Ricci C., et al., 2017, ApJ 850, 74

Lampton M., Margon B., Bowyer S., 1976, ApJ 208, 177

Laor A., 1991, ApJ 376, 90

Lapointe M.R., 2020, Master thesis, Laurentian University, Sudbury, Canada

Liedahl D.A., Osterheld A.L., Goldstein W.H., 1995, ApJL 438, L115

Maccarone T.J., Gallo E., Fender R., 2003, MNRAS 345, L19

MacKay D.J.C., 2003, Cambridge University Press

Markoff S., Nowak M.A., Wilms J., 2005, ApJ 635, 1203

Mason K.O., Breeveld A., Much R., et al., 2001, A&A 365, L36

Matt G., Perola G.C., Piro L., 1991, A&A 247, 25

Mondal S., Salgundi A., Chatterjee D., et al., 2023, MNRAS 526, 4718

Netzer H., 2013, Cambridge University Press

Niedźwiecki A., Zdziarski A.A., Szanecki M., 2016, ApJL 821, L1

Niedźwiecki A., Życki P.T., 2008, MNRAS 386, 759

Novikov I.D., Thorne K.S., 1973, In: Black Holes (Les Astres Occlus)., p.343

Pearson K., 1900, The London, Edinburgh, and Dublin Philosophical Magazine and Journal of Science 50, 157

Peterson B.M., 1993, PASP 105, 247

Piotrowska J.M., García J.A., Walton D.J., et al., 2023, arXiv e-prints arXiv:2311.04752

Pringle J.E., 1976, MNRAS 177, 65

Revnivtsev M., Sazonov S., Gilfanov M., et al., 2006, A&A 452, 169

Ricci C., Trakhtenbrot B., Koss M.J., et al., 2017, ApJS 233, 17

Risaliti G., Bianchi S., Matt G., et al., 2005, ApJL 630, L129

Ross R.R., Fabian A.C., 2005, MNRAS 358, 211

Ross R.R., Fabian A.C., Ballantyne D.R., 2002, MNRAS 336, 315

Roy V., 2020, Annual Review of Statistics and Its Application 7, 387

Rybicki G.B., Lightman A.P., 2004, WILEY-VCH Verlag GmbH & Co. KG

Saglia R.P., Opitsch M., Erwin P., et al., 2016, ApJ 818, 47

Schwarzschild K., 1916, Sitz. K. Preuss. Ak. Wiss. 189–196

Shakura N.I., Sunyaev R.A., 1973, A&A 24, 337

Shannon C.E., 1949, The Bell System Technical Journal 28, 656

Steiner J.F., García J.A., Eikmann W., et al., 2017, ApJ 836, 119

Strüder L., Briel U., Dennerl K., et al., 2001, A&A 365, L18

Sunyaev R.A., Titarchuk L.G., 1980, A&A 86, 121

Svoboda J., Dovčiak M., Goosmann R., Karas V., 2009, A&A 507, 1

Taylor C., Reynolds C.S., 2018, ApJ 855, 120

Teyssier R., 2002, A&A 385, 337

Thorne K.S., 1974, ApJ 191, 507

Tomsick J.A., Parker M.L., García J.A., et al., 2018, ApJ 855, 3

Urry C.M., Padovani P., 1995, PASP 107, 803

Ursini F., Dovčiak M., Zhang W., et al., 2020, A&A 644, A132

van Holten J.W., 1997, Fortschr. Phys. 45, 439

Walton D.J., Alston W.N., Kosec P., et al., 2020, MNRAS 499, 1480

Walton D.J., Baloković M., Fabian A.C., et al., 2021, MNRAS 506, 1557

Webster B.L., Murdin P., 1972, Nature 235, 37

Wilkins D.R., Cackett E.M., Fabian A.C., Reynolds C.S., 2016, MNRAS 458, 200

Wilkins D.R., Fabian A.C., 2012, MNRAS 424, 1284

Wilkins D.R., Gallo L.C., 2015, MNRAS 449, 129

Wilms J., Allen A., McCray R., 2000, ApJ 542, 914

Wilms J., Reynolds C.S., Begelman M.C., et al., 2001, Astronomische Gesellschaft Meeting Abstracts, p. MS 01 20

Wilson A., 2005, ESA achievements: more than thirty years of pioneering space activity 250

Wolter H., 1952, Ann. Phys. (Leipzig) 445, 94

Workman R.L., et al., 2022, Prog. Theor. Phys. 2022, 083C01

Xu Y., García J.A., Walton D.J., et al., 2021, ApJ 913, 13

Zackrisson E., 2005, PhD thesis, Uppsala University, Department of Physics and Astronomy, Uppsala, Sweden

Zdziarski A.A., Johnson W.N., Magdziarz P., 1996, MNRAS 283, 193

Zhang W., Dovčiak M., Bursa M., 2019, ApJ 875, 148

Zhou M., Ayzenberg D., Bambi C., Nampalliwar S., 2020, Phys. Rev. D 101, 043010

Życki P.T., Done C., Smith D.A., 1999, MNRAS 309, 561

Acknowledgements

I give many thanks to Jörn Wilms for welcoming me into the observatory and providing me with a fascinating thesis topic; to Thomas Dauser for being endlessly patient, always having an open ear for my questions, and being a very quick and prolific reader; to the "reflection team" Ole, Amy and Alexey for giving me valuable comments on my working methods and text, and for being generally great people; to my desk neighbor Jakob for letting me interrupt his hard work on many occasions; to the rest of the observatory for fun conversations in the kitchen when I was looking for an excuse to procrastinate. Special thanks also go to my roommates Anna & Basti for nurturing me with great food for the body and the soul, whichever was needed.

Statutory Declaration

I declare that I have developed and written the enclosed thesis entirely by myself and have not used sources or means without declaration in the text. Any thoughts or quotations which were inferred from these sources are clearly marked as such. This thesis was not submitted in the same or in a substantially similar version, not even partially, to any other authority to achieve an academic grading and was not published elsewhere.

.....

Julia Häfner Erlangen, December 4, 2023